INVESTIGATION OF PHYSICAL AND ELECTRO-OPTIC DIFFRACTIVE STRUCTURES FOR ENERGY-EFFICIENT SMART WINDOW APPLICATIONS

BY

LINUS JANG

DISSERTATION

Submitted in partial fulfillment of the requirements
for the degree of Doctor of Philosophy in Materials Science and Engineering
in the Graduate College of the
University of Illinois at Urbana-Champaign, 2010

Urbana, Illinois

Doctoral Committee:

Professor John A. Rogers, Chair
Professor Kanti Jain, Director of Research
Professor Phillip H. Geil
Professor Nancy R. Sottos
Professor J. Gary Eden

ABSTRACT

The cost of energy used for lighting, heating, and cooling in commercial and residential buildings is increasing annually while wasteful losses and gains through inefficient windows can be avoidable with advanced technology. Energy-efficient smart windows in commercial and residential buildings can reduce energy consumption for temperature control and lighting, potentially saving billions of dollars in heating, cooling, and lighting costs. A smart window is so named for its ability to have control over the window's optical properties such that they adapt to changing environments. A wide variety of technologies to improve window efficiency have been researched to date, including various mechanical and optical methods, but none has shown the ability to efficiently reject or admit solar heat when desired while retaining daylight that is useful for indoor lighting.

To overcome the limitations of current window technologies in providing control over both visible and near-infrared radiation, a novel smart window technology is described that incorporates both physical and electro-optic blazed diffractive components for the control of solar heat while retaining natural light. The optical behavior of physical diffractive structures in different configurations to optimize design parameters such as spatial frequency, groove angle, and angle of incidence are investigated by both theoretical and experimental approaches. Predictive optical models that agree well with experimental results are developed to design the diffractive components for the smart window with high-efficiency. A novel fabrication technique,

which offers a low-cost approach with customizability of grating pitch and grating angle, for physical blazed gratings using angled photoablation and *in-situ* masking is also developed.

Based on the results from physical blazed gratings, the novel concept is extended to electro-optic diffractive structures that can be incorporated into energy-efficient adaptive window systems with the desired user controllability. The continuous triangular groove profile of the physical blazed grating is approximated by a 4-step binary profile which is realized by an array of blazed elements each with a 4 x 4 array of passive matrix pixels. Extensive optical modeling and simulation performed using advanced optical design software further confirmed the functionality of selective transmission of the near infrared radiation and indicated the feasibility of the electro-optic diffractive components for smart window technology. Microelectronic fabrication processes for the pixelated optoelectronic smart window based on liquid crystal polymer blazed diffraction gratings are also explored and developed.

ACKNOWLEDGMENTS

I could never thank my advisor, Professor Kanti Jain, enough for his support, encouragement, and inspiration throughout my graduate study. The research work presented in this thesis would not have been possible without his insightful guidance. I would also like to thank my Ph.D. committee members, Professor John A. Rogers, Professor Phillip H. Geil, Professor Nancy R. Sottos, and Professor J. Gary Eden for their helpful comments and useful suggestions.

I am grateful to all members of the Photonics, Microelectronics, and Microsystems Laboratory (PMML) – Dr. Junghun Chae, Dr. Yoonsoo Han, Kevin Lin, and Hyunjong Jin – for their help and support regarding the numerous theoretical modeling and experimental work in this thesis. Special thanks go to Dr. S. Kuchibhotla for his contribution with optical simulation and discussion with the experimental work on the large-area excimer laser photolithography system.

Finally, I owe my deepest gratitude to all of my family. I am heartily thankful to my lovely wife, Haejin Jang for her sacrifice, patience, encouragement, and endless love. This dissertation would never have been completed without her being beside me. The arrival of my adorable son, Justin Damin Jang, also gave me strength and perseverance to carry on whenever I felt exhausted. I am indebted to my parents and parents-in-law for their constant support, prayer, and unconditional love throughout my life.

TABLE OF CONTENTS

LIST OF FIGURES

CHAPTER 1

INTRODUCTION

1.1. Motivation for Energy-Efficient Windows

The recognition of the diminishing availability and increasing costs of current energy resources, combined with significant barriers (technological, financial, and political) in the development of new energy resources, has highlighted the enormous importance of making our society's current energy usage means more efficient. The cost of energy used for lighting, heating and cooling in commercial and residential buildings is a staggering number—estimated by the Department of Energy in 2005 to be $416 billion [1, 2], a figure that is certainly much higher now. It has been further estimated that annual costs attributed to wasteful losses and gains through inefficient windows exceed $50 billion, and those to interior lighting, $70 billion. Therefore, a smart window technology that can reduce losses, increase efficiency, and enable recycling of valuable energy sources presents a highly attractive opportunity for making a major contribution in an enormous commercial market that is of global importance.

Many types of advanced windows have been developed to date, including various mechanical and optical technologies, but all of them suffer from one or more of the following limitations: inability to efficiently reject solar heat when desired, inability to accept solar heat when desired, blocking daylight when only heat blocking is desired, high costs, difficult to implement on large windows, and nondynamic configuration.

One of the most crucial limitations is that visible light, which can be useful for indoor lighting, is sacrificed to block the heat generating near-infrared radiation.

In addition to windows, skylights, doors, and other glass exteriors in buildings, this technology will be also attractive for automobile windows and sunroofs, greenhouses, and windows for aircraft and military vehicles. This technology will be applicable globally without geographic or seasonal limitations since its benefits include reduction of heating costs during winter, reduction of cooling costs during summer, and reduction of interior lighting costs throughout the year. Further, the development of these low-cost process technologies for fabrication of efficient liquid crystal light control devices will also have benefits for other applications such as large-area beam steering systems, flexible displays, and flat-panel displays.

1.2. Smart Window Technologies

Windows in a building are important structures that require a sophisticated design to provide natural light, comfort, and a view of the outside environment. While the comfort level of the occupants is important, energy loss through windows results in increased energy cost to sustain HVAC for large buildings; thus, windows are required to be energy-efficient. A variety of technologies to improve window efficiency have evolved to address this issue; a smart window is so named for its ability to have control over the window's optical properties such that they adapt to changing environments.

The following is an overview of the currently available technologies for improving energy efficiency of windows in the industry and summarizes their limitations.

1.2.1. Current Energy-Efficient Window Technologies

Window systems can be categorized by their operational method - either as a mechanical or optical window. Optical methods can be further categorized by their control method - passive, dynamic, and active window.

1.2.1.1. Mechanical Methods

A variety of fixtures, such as awnings, louvers, blinds, etc., are used in buildings to control solar heat and light. The general goal of these structures is to physically block direct sunlight. These devices are often of fixed construction but also can be made adjustable or retractable to respond to the changing incoming solar radiation. Louvers and blinds are composed of slats of various sizes, widths, and shapes. All of these devices are mainly intended for shading but are also used to redirect daylight, reduce glare, and control solar heat gain [3-6]. Fixed systems are relatively low-cost, but controllable systems tend to be more expensive. In the context of energy efficiency, their major drawback is that when they are used to block direct solar heat, they also block direct daylight.

1.2.1.2. Optical Methods

The general concept of optical methods for solar heat control is to absorb or reflect solar radiation by changing the optical properties of the window. These methods fall in the smart window category [7] and can be classified into passive, dynamic, and

active systems, depending on how they are controlled. Since approximately 40% of the solar radiation is in the near-IR region (box in Figure 1.1), techniques that are more spectrally selective in rejecting or transmitting the incident radiation provide greater energy efficiency.

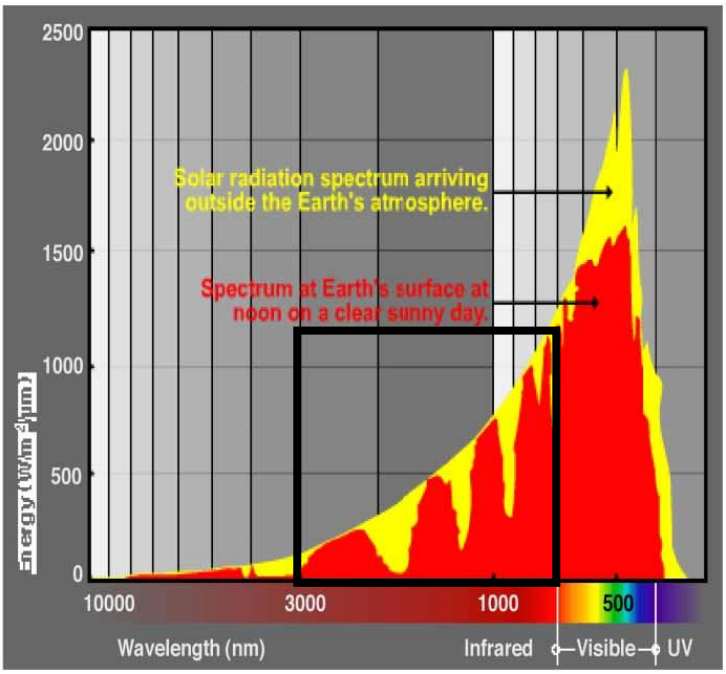

Figure 1.1: Solar spectral distribution, showing 40% of it lies in the 0.7 - 3 μm near-IR region.

1.2.1.2.1. Passive Systems

In this class of windows, a spectrally selective coating is applied to the window glass to reject specific regions of the solar spectrum, generally UV and IR, while admitting the visible portion of the solar spectrum. Such windows usually have a thin-film metal coating or a dielectric-metal multilayer coating [8-13]. By reducing solar heat gain, they benefit buildings in hot climates where the cooling load is a major energy cost. These coatings can also be applied on the interior side of the windows to reduce

heat loss in cold climates, but the coating also blocks incoming heat from direct sunlight, which is an important natural heating source. This technology is not suitable for mixed climates because the coating property is fixed once it has been applied to the window.

1.2.1.2.2. Dynamic Systems

Photochromic materials undergo a reversible photochemical reaction under exposure to solar radiation in a specific spectral region, usually UV [14]. This reaction changes their optical absorption band, resulting in a change of color. The reaction can be reversed by eliminating the light source that has activated the transformation. The largest application of this technology appears in eyeglasses that automatically darken under direct solar exposure. The switching speed of photochromic materials is much faster in solution form than in solid form [15-18]. Recently, it has been reported that the switching speed of a photochromic dye in solid form, such as an ophthalmic lens, can be improved by adding flexible polymers which have low glass-transition temperatures [19].

Thermotropic and thermochromic materials change their optical properties in response to temperature changes [20]. In general, they are transparent at lower temperatures and become translucent or opaque at higher temperatures. The basic mechanism is based on the movement of component molecules that cause a phase transition in the material, which changes the optical characteristic of the material [21, 22]. Major commercial applications of these materials include skylights and upper windows, where visual comfort can be sacrificed.

1.2.1.2.3. Active Systems

Suspended particle systems (SPS) have an active polymer layer in which light absorbing microparticles are suspended, as shown in Figure 1.2.

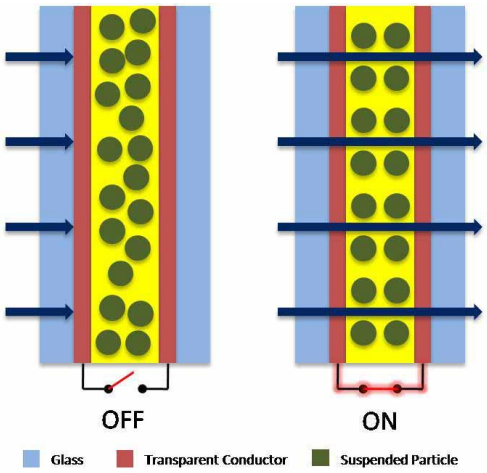

Figure 1.2: The "ON" and "OFF" states of a Suspended Particle Systems (SPS) window.

In the "off" state, the suspended particles are randomly distributed and absorb light, making the film opaque. When an electric field is applied to the active layer, the particles align to the field and the film becomes transparent. The transmission changes from 6-15 % in the off state to 60-75 % in the on state, with switching speeds of 100-200 ms, and an operating voltage of 100 V AC [23]. Another application of an SPS is electrophoretic electronic paper, also known commercially as E-ink, which utilizes migration of color-coated suspended particles under the influence of an applied electric field. With an operating voltage of 90 V DC, a 6:1 contrast ratio with memory effect has been attained [24].

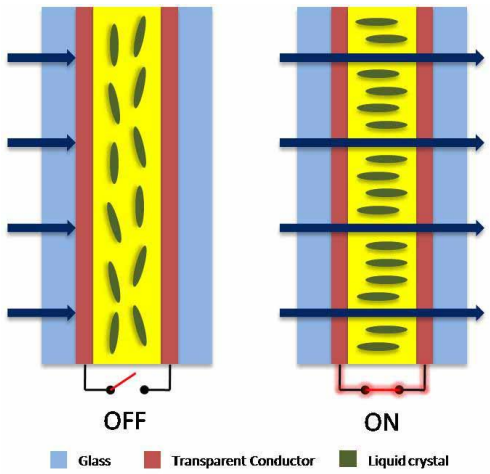

Figure 1.3: The "ON" and "OFF" states of a Polymer Dispersed Liquid Crystal (PDLC) window.

A polymer dispersed liquid crystal (PDLC) system is an emulsion of a polymer and a liquid crystal which can be formed into a film. The refractive index of the polymer matrix is matched to the dispersed liquid crystal [25]. The film is then sandwiched between two transparent sheets coated with Indium Tin Oxide (ITO), as shown in Figure 1.3. In the off state, the randomly oriented liquid crystals scatter light, making the film translucent. When an electric field is applied, the dispersed liquid crystals align parallel to the field and the film becomes transparent. Typical operating voltages of PDLC are between 24 and 100 V AC and power consumption is less than 5 W/m^2 for switching [26]. Since there is no memory effect, continuous power is required to hold its transparent state, which makes the power consumption in PDLC systems higher than that of electrochromic windows (described below), which require power only during switching.

Electrochromic windows are composed of an electrochromic layer [typically tungsten oxide (WO_3)], an electrolyte layer, and an ion storage layer which are placed between transparent conductors such as ITO, as shown in Figure 1.4. Optical properties

of the electrochromic layer change by the injection of coloration ions from the storage layer. A reverse electric field draws back the coloration ions into the storage layer, switching the electrochromic layer back to its normally clear state. Various coloration ions such as Li^+, H^+, Na^+, and Ag^+ are used. Inorganic oxides such as WO_3, NiO, V_2O_5, and MoO_3 are used for the electrochromic layer among which WO_3 has been most widely investigated [26-28]. However, the high cost of electrochromic windows ($100-200/ft^2) has been a major obstacle in their applicability in wide markets [29].

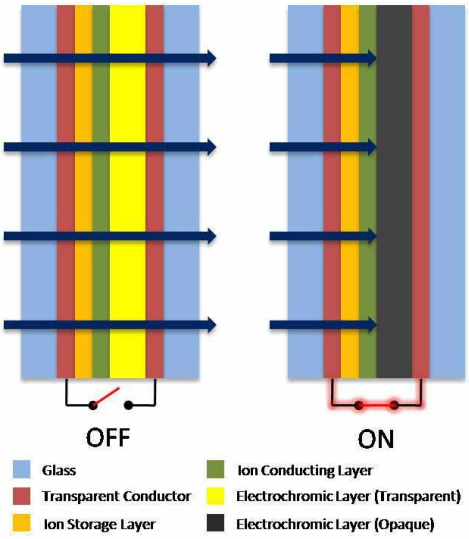

Figure 1.4: The "ON" and "OFF" states of an Electrochromic window.

Gasochromic devices employ the same principle as electrochromic windows except that gasochromic devices have coloration ions which are supplied by a gas [30]. H_2 gas is typically used and injected between two panes; one of the panes has a thin catalytic coating on top of a laver of tungsten oxide (WO_3) (a chromogenic layer). Decoloration can be achieved by feeding another purging gas. The major drawback with this technique is the need for integration of gas lines in the window, which is a substantial construction challenge.

1.2.2. Limitations of Current Technologies

The following list describes the major drawbacks of each of the above window technologies and is followed by a comparison table (Table 1.1).

(1) Mechanical methods do not provide any spectral selectivity for accepting or rejecting solar radiation.

(2) Photochromic windows are self-regulating, which make them impractical as energy-saving devices since they cannot be controlled as desired in response to a changing environment. Their optical transmission changes when exposed to UV, causing heat to be blocked even on a sunny cold winter day.

(3) Thermochromic technology has the same drawbacks as photochromic technology except that in the former, the optical transmission changes with temperature, causing daylight to be blocked on a sunny day.

(4) PDLC windows in their normal state are diffusely transmitting (translucent), which is suitable for privacy control but is ineffective in blocking the solar heat.

(5) SPS windows become opaque in their off state. Since they absorb both IR and visible light, interior lighting becomes necessary, causing the lighting component of building energy use to increase.

(6) Electrochromic windows, although efficient in switching to an opaque state, are very expensive (~ \$100-200/ft^2) and interior lighting is still required since they absorb or reflect visible light.

Method	Advantages	Disadvantages
Mechanical Methods: Awnings, louvers, blinds	• Cheap, easily available	• Fixed • Block direct light as well as heat
Passive Methods: Coatings	• Block heat • Reduce glare • Cheap	• Reduce light • Change hue • Cannot admit heat in winter
Dynamic Methods: Photochromic	• Reduce glare	• Cannot admit heat in winter • Difficult to implement on large windows
Thermochromic	• Block heat • Easy to implement on large windows	• Translucent (no view) • Inhomogeneity during switching
Active Methods: Electrochromic	• Change per needs	• Block light and heat • Expensive • Difficult to implement on large windows

Table 1.1: Comparison chart of currently available technologies for improving energy efficiency of windows in the industry with their major drawbacks highlighted.

1.3. Dissertation Overview

In this thesis, we propose a novel smart window technology which is a programmable, pixelated optoelectronic window system based on liquid crystal polymer blazed diffraction gratings constructed by microelectronic fabrication processes. This new energy-efficient window technology is configurable in such a manner that its spectral characteristics can be selected in different ways to enable dynamic control of the reflectivity and transmission for near-infrared as well as visible light as desired, leading to highly cost-effective, programmable window systems with greatly improved energy efficiency and recycling capability. We also investigate optical properties of physical diffractive structures and extend the novel concept to electro-optic diffractive structures that can be incorporated into the window system. Lastly, we develop reliable and versatile large-area fabrication processes for this new envelope technology. Figure 1.5 illustrates the conceptual framework of the smart window research program.

The thesis is arranged as follows: Chapter 2 reviews briefly current window technologies followed by their limitations. We propose a novel solution to address a major drawback in current window technologies – their inability to provide selective control over heat and natural light adaptively. Solar spectral irradiance is analyzed to separate solar energy components according to spectral regions and solar trajectories; and time and location are analyzed to obtain the variation of the angle of incidence on the window. Chapter 3 provides a detailed background on the principles of physical diffractive structures with current fabrication methods to create them. Furthermore, theoretical considerations for blazed diffraction gratings are discussed followed by

methods for efficiency measurement. Experimental testing on selected blazed gratings are performed which demonstrates spectral filtering. In addition, we propose and demonstrate the use of multiple physical diffractive structures in series that enhance the efficiency of the smart window system. Experimental results are also compared to analytical models. Chapter 4 extends the physical concept to electro-optic diffractive structures where a liquid crystal is introduced as the electro-optic medium that generates the diffractive structures by applying electric field. A binary approximation to a triangular physical profile is described followed by optical modeling and simulations. The diffraction pattern of a 4-step-profile blazed diffraction grating is simulated based on Huygen's principle and compared with theoretically calculated diffraction angles. Chapter 5 describes the overall fabrication process of the proposed electro-optic diffractive structure, which includes material selection for the electro-optic medium, experiments with unit fabrication process development and integration, and challenges. We also introduce a new and potentially cost-effective fabrication method for manufacturing blazed diffraction gratings with a wide range of groove angles. Finally, Chapter 6 summarizes the work to date and describes the future direction of the research project.

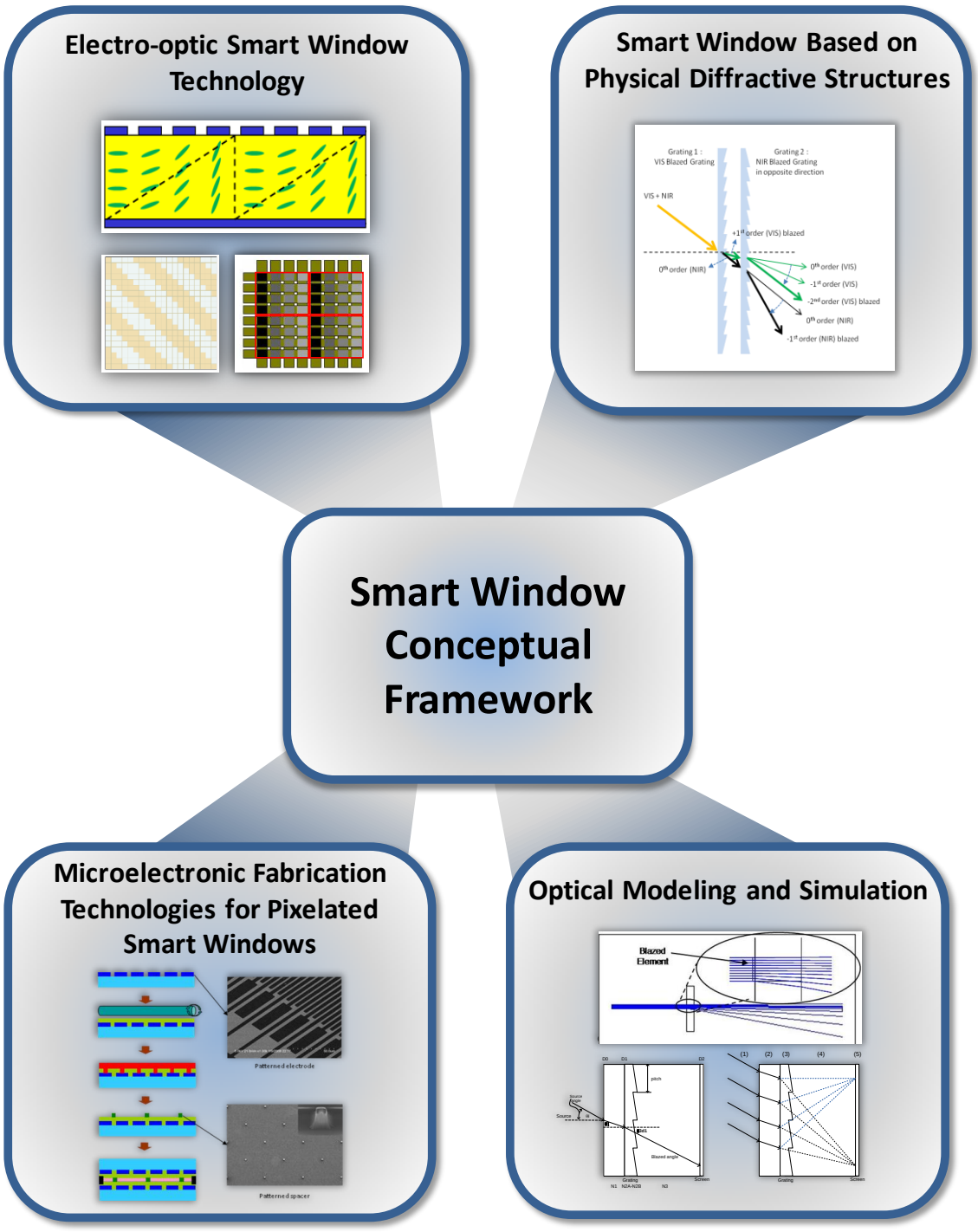

Figure 1.5: Key Components of the Smart Window Research Program.

CHAPTER 2

SPECTRALLY SELECTIVE WINDOW CONCEPT

This chapter first analyzes the solar spectral irradiance to obtain insight into the solar energy distribution depending on wavelengths. Then the solar trajectories depending on time and location are analyzed to develop an algorithm that allows us to calculate the angle of incidence at any time on our smart window. With the capability of predicting the sun's position during a day at a given time, we propose a novel concept of a spectrally selective window system which separates the heat-generating near-infrared radiation from the visible radiation in the solar spectrum by utilizing diffractive elements. Both physical diffractive structures and electro-optic diffractive structures are considered in the following chapters. The proposed new window technology has the potential to address the major drawbacks of current window technologies.

2.1. Solar Spectral Irradiance

The solar spectrum is defined as the range of electromagnetic energy emitted by the sun, extending from approximately 280 nm to 4000 nm and comprising of three major regions: ultraviolet, visible, and infrared. Although sunlight has a component in the ultraviolet regime, most of the solar energy lies in the visible and infrared regions which contribute as natural light and heat respectively. In order to visualize and

calculate the fractional contribution of the visible light and infrared heat components of the total solar energy, we adopted and analyzed the Simple Model of the Atmospheric Radiative Transfer of Sunshine (SMARTS), developed at the Florida Solar Energy Center (FSEC) in the 1990s and currently supported by National Renewable Energy Laboratory (NREL) which contains spectral irradiance data for a wide range of specified atmospheric conditions [31].

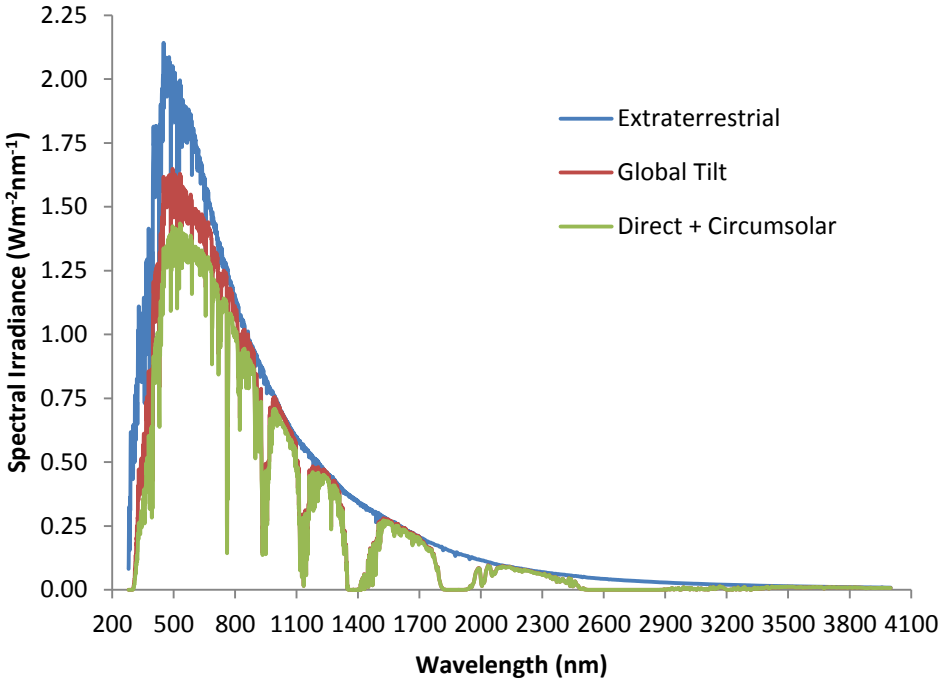

Figure 2.1: ASTM G173-03 Reference solar spectral irradiances for the case of extraterrestrial, direct normal, and hemispherical on a 37° tilted surface.

Figure 2.1 shows the American Society of Testing and Materials (ASTM) G173-03 reference spectra for the case of extraterrestrial, direct normal, and hemispherical on a 37° tilted surface (to represent the average latitude of the 48 contiguous United States) that are based on SMARTS v2.9.2 which is commonly used for photovoltaic

performance testing and materials durability exposure studies [32-34]. The "Extraterrestrial" plot refers to the case when the solar irradiance is at the top of the atmosphere at a mean distance of Earth and Sun. The Direct + Circumsolar plot is the solar spectral irradiance on the earth surface that is nearly parallel (0.5 degree divergent cone) to the surface normal pointing to the sun (Direct) plus the solar spectral irradiance within +/- 2.5 degree field of view centered on the 0.5 degree diameter solar disk, but excluding the radiation from the solar disk (Circumsolar). The Global Tilt plot is the solar irradiance from the solar disk plus the diffuse components such as scattering from the sky and reflection from the ground on a south facing surface tilted 37 degrees from horizontal. The data points in the reference spectra have a uniform wavelength interval: 0.5 nm below 400 nm, 1 nm between 400 and 1700 nm, an intermediate wavelength at 1702 nm, and 5 nm intervals from 1705 to 4000 nm.

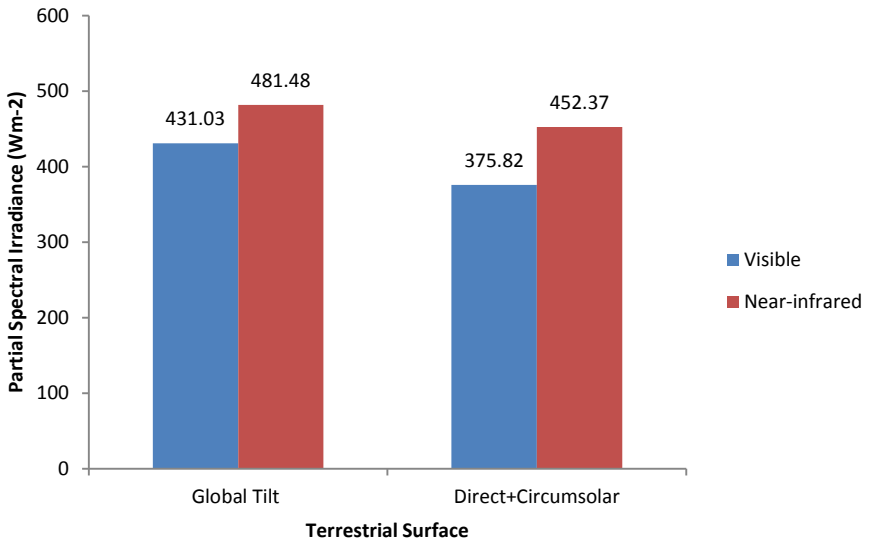

Figure 2.2: Partial spectral irradiance of visible (400 nm - 700 nm) and near-infrared (700 nm – 2500 nm) regions analyzed for global tilt and direct + circumsolar. The difference between the two plots indicates diffuse and reflected irradiance.

The total integrated irradiances for the Direct+Circumsolar plot and the Global Tilt plot are 887.65 $W \cdot m^{-2}$ and 1000.4 $W \cdot m^{-2}$, respectively. We define the visible region from 400 nm to 700 nm and the near-infrared region from 700 nm to 2500 nm to obtain and compare their fractions of the solar spectrum as shown in Figure 2.2. For direct irradiance, the visible region value is 375.82 $W \cdot m^{-2}$ (42.34%) and the near-infrared 452.37 $W \cdot m^{-2}$ (50.96%). For hemispherical irradiance which includes diffuse and reflected irradiance, the visible region value is 431.03 $W \cdot m^{-2}$ (42.98%) and the near-infrared 481.48 $W \cdot m^{-2}$ (48.01%). While the visible region has more diffuse components than the near-infrared region, most of the solar irradiation on a south facing window in the US for both visible and near-infrared regions is from direct irradiance.

2.2. Considerations of Solar Trajectory

To modulate the solar energy transmitting through the window with highest efficiency, we need to know the time-varying incidence angle of the solar irradiance as the sun moves during the day. National Oceanic and Atmospheric Administration (NOAA) provides a solar position calculator written in Java Script language which is based on astronomical algorithms and formulas [35, 36]. This program calculates the sun's position by its azimuth and elevation angles for a specified date and time by defining the geographical location based on latitude, longitude, and time zone [37].

The angle of incidence of the solar irradiance on a window can be obtained by retrieving first the azimuth and elevation angles for a specific time and location where

the window is placed and then calculating the angle of incidence from the appropriate geometrical relation with the two angles as depicted in Figure 2.3.

We converted the original source code written in Java Script to MATLAB to write a new code that generates data sets for plotting the solar trajectory graphically at any given time, date, and location. This also allows us to create automated software that controls the new window system in a way that accommodates the changes to the sun's position throughout the day. In addition, solar detectors attached to the window can be used as a complement to the automated software.

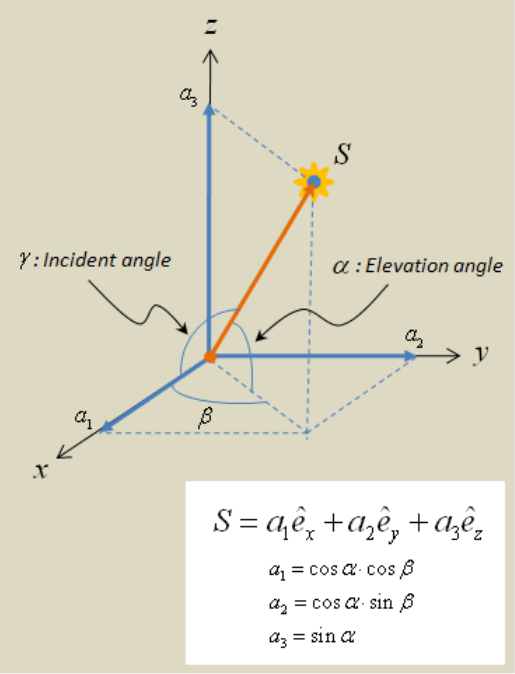

Figure 2.3: Illustration of the geometrical relationship of the angle of incidence on the yz-plane with the azimuth angle and elevation angle.

To validate our generated program, we retrieved the sun path chart for Chicago from University of Oregon Solar Radiation Monitoring Lab [38] and compared the results with our generated chart. The two plots match exactly, as shown in Figure 2.4.

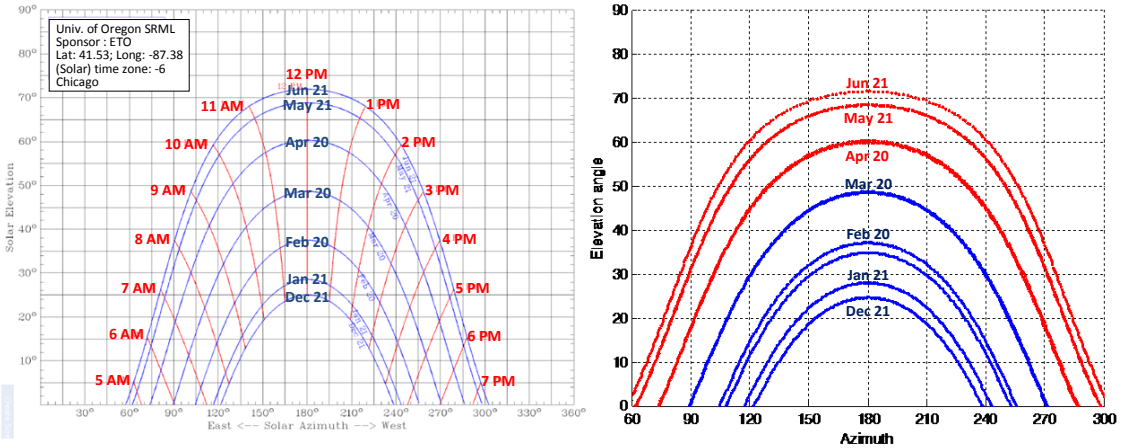

(a) (b)

Figure 2.4: Annual sun path chart for Chicago, IL. (a) From University of Oregon Solar Radiation Monitoring Lab. (b) Generated by converted MATLAB code.

Using the relationship of the incident angle to the given azimuth and elevation angles, we generate Figure 2.5 from Figure 2.4 (b) which shows the variation of the incident angle of the solar irradiance on a south facing window located in Chicago over an entire year.

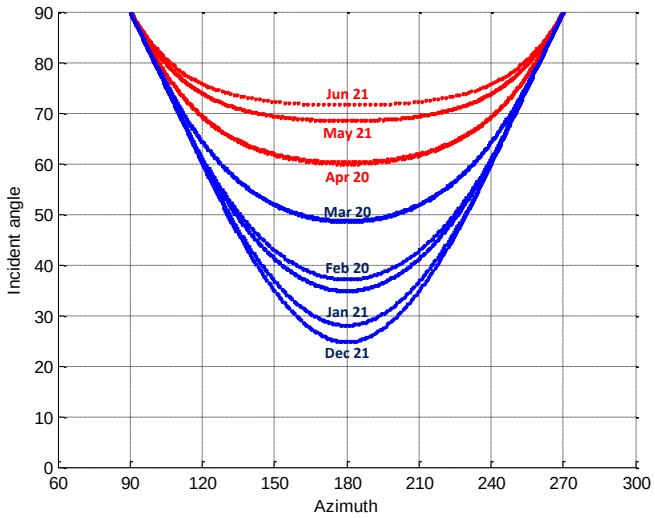

Figure 2.5: Annual variation of the solar angle of incidence on a south facing window located in Chicago, IL.

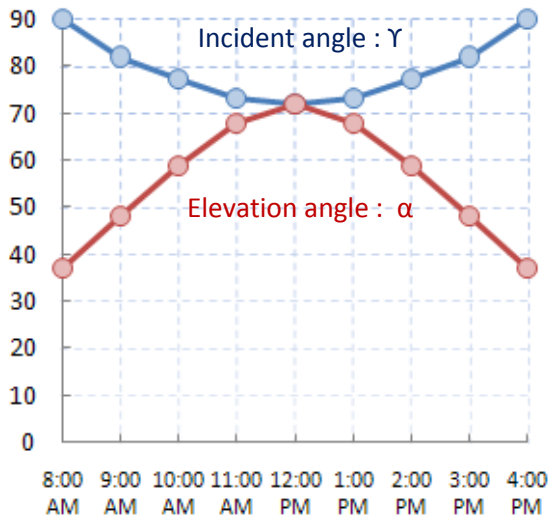

Figure 2.6: Combined plot of the solar incident and elevation angles for a south facing window located in Chicago, IL on June 21.

Here, we recognize that for a south-facing window, the incident angle is lowest at noon during a day, the time when the sun is at its highest position in the sky. Figure 2.6 is a combined plot of the incident and elevation angles for a south facing window on June 21 located in Chicago, IL as an example. Note that the incident angle spans only 18° during the day. This is indeed a nonintuitive and fortuitous finding. A narrow range of the angle of incidence on the window is favorable because it permits easier design of the energy-efficient window and allows broader operating parameters for optimizing and controlling the window's optical functionality.

Figure 2.7 illustrates the basic operation of the novel window system which comprises pixelated switchable electro-optic diffractive elements. The configuration of the diffractive elements can be controlled to change the groove orientation as necessary. Because the efficiency of a diffraction grating is highest when the plane of incidence is

perpendicular to the groove direction, the capability of switching the groove orientation ensures optimal performance of the smart window system throughout the day.

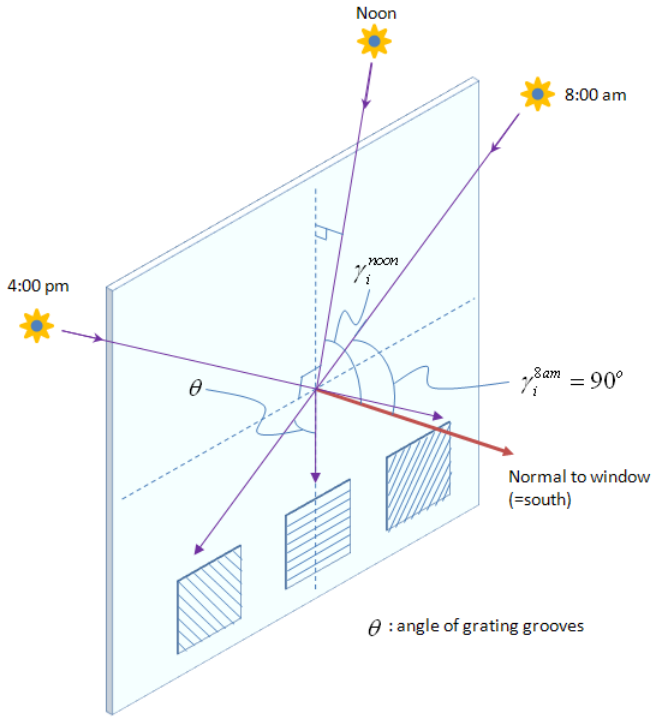

Figure 2.7: Schematic illustration of the smart window system showing how the grating plane switches adaptively to the sun's varying position during a day to maximize efficiency.

2.3. Overcoming Limitations of Current Technologies

A common limitation with current window technologies is that they also reduce visible radiation - which is useful for natural lighting – when the transmission of the incoming solar radiation is decreased to reduce heat gain during the hot season. A spectrally selective coating addresses this issue but it is not reversible and therefore the near-infrared is blocked when heat gain is desired during the cold season. To overcome these limitations, we explore a new window system that incorporates an electronically

controllable blazed transmission diffraction grating which is realized by using a transparent, high-birefringence liquid crystal as the optoelectronic material. This new window system is both spectrally selective due to the diffraction grating's inherent dispersive properties and also provides adaptive user-controllability by utilizing the electro-optic property of the liquid crystal material.

2.4. Proposed Smart Window System

The energy-efficient optoelectronic window system concept proposed in this work uses several key technical elements in novel ways. A fundamental component of the new window system is a transmissive blazed diffraction grating and a total internal reflection layer, which are attached, fabricated and configured in such a manner that their spectral characteristics can be selected in desirable ways to dynamically change the reflectivity and transmission for near-infrared as well as visible light.

The window structure, as illustrated in Figure 2.8, is comprised of an outer glass pane, a liquid crystal polymer (LCP) layer, an inner glass pane, and a total internal reflection (TIR) pane. The LCP layer is composed of many pixels, and each pixel can be independently modulated by an array of electrodes, enabling us to create a phase grating that can be programmed to function as a blazed grating only for the near-infrared spectral region of the solar radiation. The LCP is protected from solar UV radiation by a UV blocking layer. The window can be dynamically configured either as a heat rejection mode window or a heat acceptance mode window.

An example for the heat rejection mode is shown in Figure 2.8 (a). A key optical characteristic of blazed gratings is their high efficiency in directing most of the diffracted radiation in a single non-zero order [-1st order in Figure 2.8 (a)]. This enables us to direct the near-infrared radiation at the final optical surface at an angle greater than the critical angle for TIR, which redirects it to the exterior.

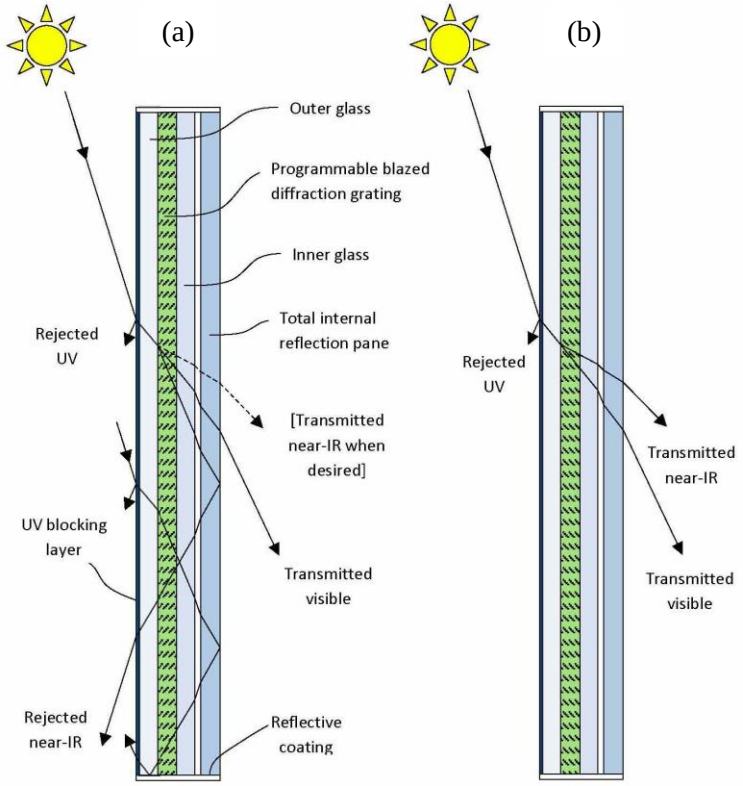

Figure 2.8: Schematic illustration of the dynamic, energy-efficient, optoelectronic smart window based on programmable blazed diffraction grating. (a) Near-IR radiation is rejected, while visible radiation is accepted. (b) Both near-IR and visible accepted.

Note that the visible component, being the 0th order, passes through to the interior. In Figure 2.8 (b), the grating is programmed to direct the diffracted near-infrared radiation towards the +1st order, which strikes the exit surface at an angle less than the critical angle so that it does not undergo TIR, and therefore enters the interior.

The visible component, again being the 0^{th} order, enters the interior. Further, as illustrated in Figure 2.9, the pixilated structure of the LCP layer enables us to orient the 'grooves' (i.e., refractive index modulations) of the blazed grating in any direction, providing the ability to track the elevation and azimuth of the sun, thus enabling the smart window to deliver its peak energy efficiency for different times of the day, seasons, and locations.

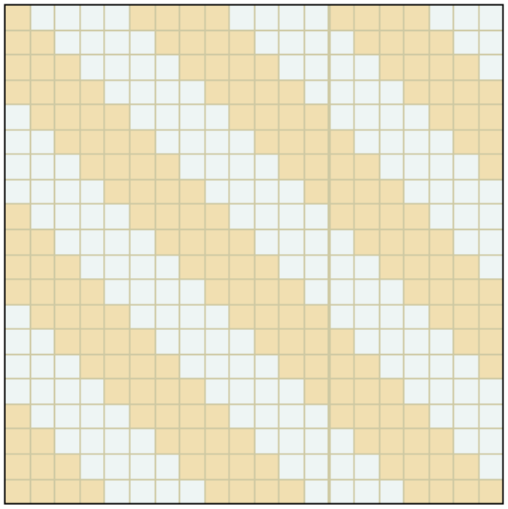

Figure 2.9: Schematic illustration of the pixelated grating structure and its groove orientation.

We remark that whereas generally a blazed grating is designed to function optimally at a specific wavelength, in the present application, it is used in a wavelength band, which results in spread of the diffraction angle in a small range, and also in a diffraction efficiency that may be slightly less than the maximum. Neither of these effects presents a major problem; as long as the deflection is such that the condition for TIR is met, the ray will be reflected back, and a diffraction efficiency that is a few percent less than the maximum (~90%) is still very effective for heat rejection. Figure 2.10 shows analytical modeling of these effects that verifies the above assertions. Note

that the boundary of critical TIR angle between near-IR and visible rays moves toward higher incident angle as grating spacing becomes larger.

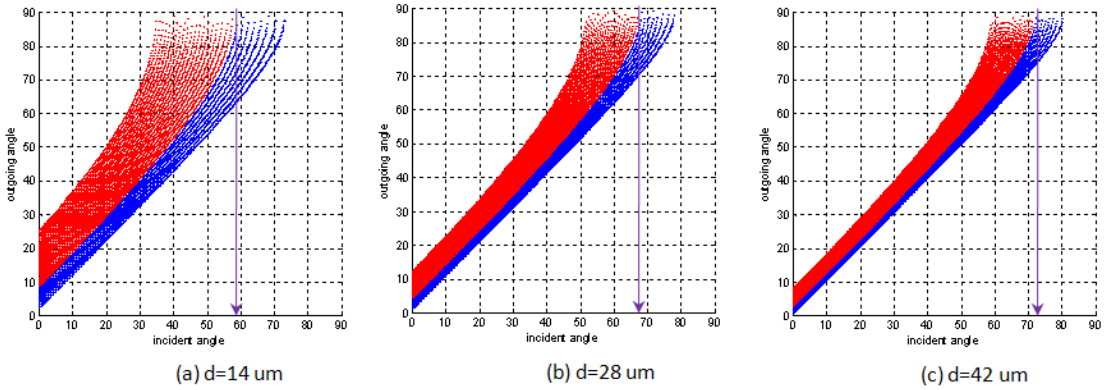

Figure 2.10: Solar spectrum after passing through the liquid crystal optical modulator whose grating period (d) is (a) 14 μm, (b) 28 μm, and (c) 42 μm. Red area represents near-IR rays, and blue area represents visible rays.

In our work, we investigate both physical and electro-optic blazed gratings to fulfill these requirements.

CHAPTER 3

SMART WINDOW BASED ON PHYSICAL DIFFRACTIVE STRUCTURES

3.1. Introduction

This section introduces the application of physical diffraction gratings in different configurations for spectral control, which will be used as a proof of concept to demonstrate the ability to independently steer the solar infrared and visible wavelengths for the 'Smart Window' application.

The angles of the diffracted orders from a conventional grating only depend on the period of the grooves, and not on their shape. By controlling the cross-sectional profile of the grooves, it is possible to concentrate most of the diffracted energy in a particular order for a given wavelength – this technique is known as "blazing". A triangular profile is commonly used for this purpose. The incident angle and wavelength for which diffraction is most efficient are often called blazing angle and blazing wavelength, respectively. The efficiency of a grating may also depend on the polarization of the incident light. When the groove spacing is less than half the wavelength of the incident light, the only order transmitted is the zeroth order. Gratings with such small periodicity are called subwavelength gratings and exhibit special optical properties. Subwavelength gratings made on an isotropic material exhibit anoisotropic

behavior, where the material behaves as if it were birefringent, which means the optical property of the material is directionally dependent. Diffraction gratings can be produced by modulating one of the following material properties: transparency (transmission amplitude gratings), reflectance (reflection amplitude gratings), and refractive index (phase gratings).

3.1.1. Conventional and Blazed Diffraction Gratings

To illustrate the concept of spectral selectivity and radiation control by diffractive structures, a brief description of the optical principles underlying blazed diffraction gratings is provided here. The difference between a conventional and a blazed grating is the way the diffracted radiation is distributed among various diffraction orders.

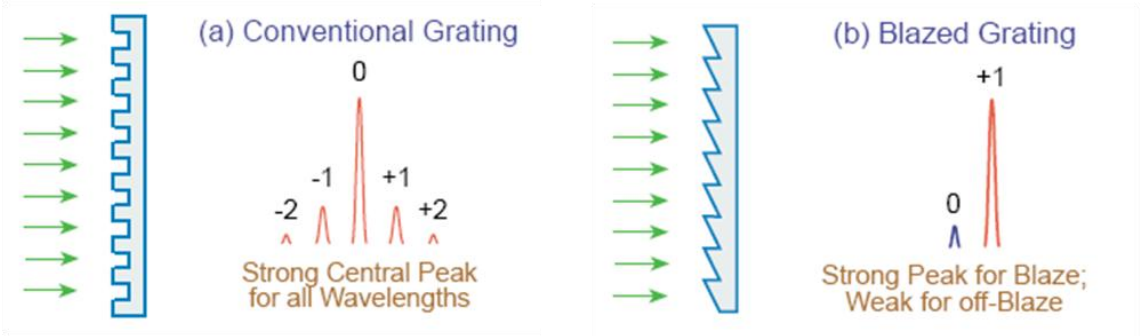

Figure 3.1: Diffraction of incident light: (a) into multiple diffraction orders in a conventional grating, and (b) into a single order in a blazed grating.

In a conventional grating, as shown in Figure 3.1 (a), the strongest diffracted order is the 0^{th} order, around which the higher orders (+1, -1, +2, -2, etc.) are symmetrically dispersed, with decreasing intensity. The diffraction angles θ_m of the various orders m are given by the diffraction grating equation [39-42],

$$m\lambda = d\,(\sin\theta_m - \sin\theta_i) \tag{3.1}$$

where θ_i is the angle of incidence and λ is the wavelength.

Since the 0^{th} order is along the optical axis for *all* wavelengths, a conventional diffraction grating cannot efficiently separate the near-infrared wavelengths from the visible wavelengths of the solar radiation.

A blazed grating is a special type of diffraction grating that allows the diffracted radiation in a given spectral region to be highly concentrated into a desired, *specific*, non-zero diffraction order (generally +1 or -1 order). This is accomplished by constructing grooves of a properly designed triangular (or sawtooth) profile on the grating surface, as shown in Figure 3.1 (b). The specific inclination of the groove surface provides a constructive phase relationship between light rays exiting from different grooves, thus enabling the diffracted light of the given spectral band to be concentrated into a desired *single* diffraction order, shown as the +1 order in Figure 3.1 (b) and determined by the blazed grating equation [39, 40],

$$\theta_m = \theta_i + (n - 1)\,\alpha \tag{3.2}$$

where α is the groove slope angle.

This allows a blazed grating to separate the near-infrared wavelengths from the visible wavelengths in the solar radiation extremely efficiently. Ideally, a sawtooth profile provides the highest blaze efficiency. In practice, a staircase profile is easier to fabricate and provides reasonably high efficiency — 81% with four steps and 95% with eight steps which will be discussed in Chapter 4.

Such phase gratings can be produced by creating physical grooves of a surface-relief type, or by inducing suitable refractive index changes by electronic means or other methods. As described in Section 2.4, we will use this unique property of blazed diffraction gratings to optimally control the transmission of solar radiation (infrared and visible) through nominally transparent windows in buildings and other large enclosures.

3.1.2. Reflection and Transmission Diffraction Gratings

A reflection grating and a transmission grating are distinguished by whether the grating grooves are formed on a reflective surface or on a transparent surface. As reflection gratings are typically fabricated by coating the grating surface with a reflective metal, a transmission grating can be made by stripping the metal coating from a reflection grating. The substrate material for transmission gratings must be highly transparent to the wavelength spectrum to be used and requires the absence of imperfections such as bubbles, inclusions, etc., which is not a concern for reflection gratings.

The absence of a reflective metal coating in transmission gratings makes the diffraction efficiency behavior less complex than for reflection gratings so that efficiency curves of transmission gratings show negligible polarization effects.

In the case of reflection gratings, high-efficiency blazing for a specific diffraction order occurs when the reflection angle of the input beam equals the diffraction angle which is determined by the grating period. On the other hand, it is the refraction angle in place of the reflection angle that ensures the high-efficiency blazing to occur for transmission gratings. Transmission gratings also involve reflection at the

interface between the substrate material and air which makes it less efficient than for reflection gratings but antireflection (AR) coatings can be applied to reduce reflections.

Coarser groove frequencies (pitches) are also preferred for transmission gratings than reflection gratings for high diffraction efficiency. The reason the efficiency is dependent partially on the groove frequencies is that the light going through the grating-air interface is subject to total internal reflection, which can result in backward-propagating orders (resulting in a weak reflection grating). The greater the number of grooves/mm, the greater the reflection effect which in turn affects the efficiency of the grating.

3.2. Current Fabrication methods for Physical Diffraction Gratings

There are several manufacturing techniques to construct physical gratings. The major techniques are mechanical ruling, holographic imaging, and photolithography. These are briefly described below.

3.2.1. Mechanical Ruling

Physical diffraction gratings in the early times were manufactured using hard diamond tips to mechanically scribe and form the grating grooves into a plane or concave substrate coated with a thin layer of evaporated metal [43, 44]. These diffraction gratings, called ruled gratings, suffered from periodic errors in the spacing of the grooves which resulted in spurious lines in the blazed spectrum, also known as Rowland ghosts. The primarily cause of this error is inherent in the mechanical ruling

engine's precision screw or bearings. High-quality ruling engines equipped with an interferometric control system, such as a Michelson engine, Mann engine, and MIT 'C' engine, have been developed to virtually eliminate the Rowland ghost error and to achieve a grating quality close to the theoretical resolving power [45, 46].

3.2.2. Holographic Recording

Another technique to manufacture diffraction gratings utilizes photolithographic imaging where the interference fringe pattern is exposed on photosensitive materials. Gratings of this type are commonly known as holographic gratings. Although the concept of using interference fringe fields with an imaging material was first developed when diffraction gratings were mostly manufactured by ruling engines [47], strong monochromatic light sources and high-resolution photoresists were not available until many decades later [48-50].

Typically, these gratings are manufactured by placing a photoresist coated substrate in an interferometer. Ambient light needs to be minimized to enhance the contrast of the image. After the interference fringe field is recorded on the photoresist, it undergoes chemical development where the exposed areas (bright fringes of the interference field) are washed away for a positive resist while the unexposed areas (dark fringes of the interference field) are dissolved for a negative resist. The region where the material is removed forms the valley and the remaining material forms the ridge of the holographic grating.

Another technique to manufacture holographic diffraction gratings without chemical development is called Volume Phase Holography (VPH) [51]. Instead of

dissolving a photoresist, this technique uses a photosensitive gel, like dichromated gelatin, sandwiched between two glass substrates. An interference fringe field exposes the gel as in the case of a photoresist in the surface relief holographic grating and is later wet processed but instead of removing the photoresist, the photosensitive gel transforms such that its refractive index is periodically modulated and it has no physical grooves, which causes less scattering effects than in other groove-type gratings. In addition, because VPH is created between two rigid glass substrates, it is safer against physical damage such as scratches, dents, or bending.

Ruled gratings and holographic gratings have differences in grating efficiency, scattered light, groove profile limitations, and groove frequency limitations. Grating efficiency depends largely on groove profiles where ruled gratings are mostly triangular while holographic gratings are sinusoidal. Surface imperfections of the grooves by mechanically ruled gratings, where the grooves are formed one after another, are the main cause for stray light. Light scattering in holographic gratings, where the grooves are recorded simultaneously, is therefore minimal and the grating is ideal for use in spectroscopic systems.

3.2.3. Photolithography

Semiconductor integrated circuit manufacturing technologies can also be used to create a master grating by imaging the desired surface profile onto a photoresist layer, which is then transferred into a mold by electroforming. This class of fabrication processes is especially suited for producing blazed gratings with high groove densities (e.g., > 1000 grooves/mm). After the master grating is created, subsequent gratings can

be replicated economically in a variety of plastics such as PMMA (polymethyl methacrylate) and polycarbonate. Fabrication costs are minimized by using precisely controlled processes to create desirable groove profiles and creating high-quality replicas from master gratings.

3.2.3.1. Conventional Photolithography

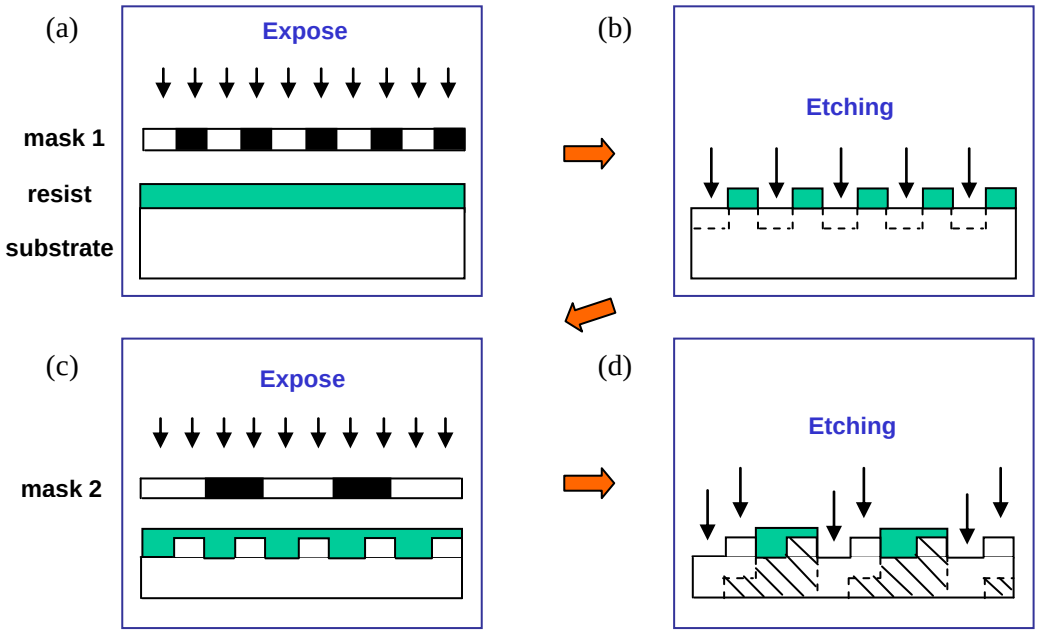

Figure 3.2: Fabrication process flow for blazed diffraction grating using conventional photolithography. (a) Photoresist coating and pattern 1 exposure. (b) Exposed photoresist removal and substrate etching 1. (c) Photoresis overcoating and pattern 2 exposure. (d) Exposed photoresist removal and substrate etching 2.

Figure 3.2 illustrates the most popular method which uses N binary photomasks to fabricate blazed profiles of 2^N levels on a substrate. Each binary photomask is illuminated by UV light followed by developing the resist. The resist pattern is then transferred onto the substrate by either dry etching or wet etching. However, the phase profile can be distorted because of misalignment between the photomasks; misalignment

reduces the grating efficiency. Precise control of etching is also required to achieve a smooth and uniform surface profile.

3.2.3.2. Gray-Scale Photolithography

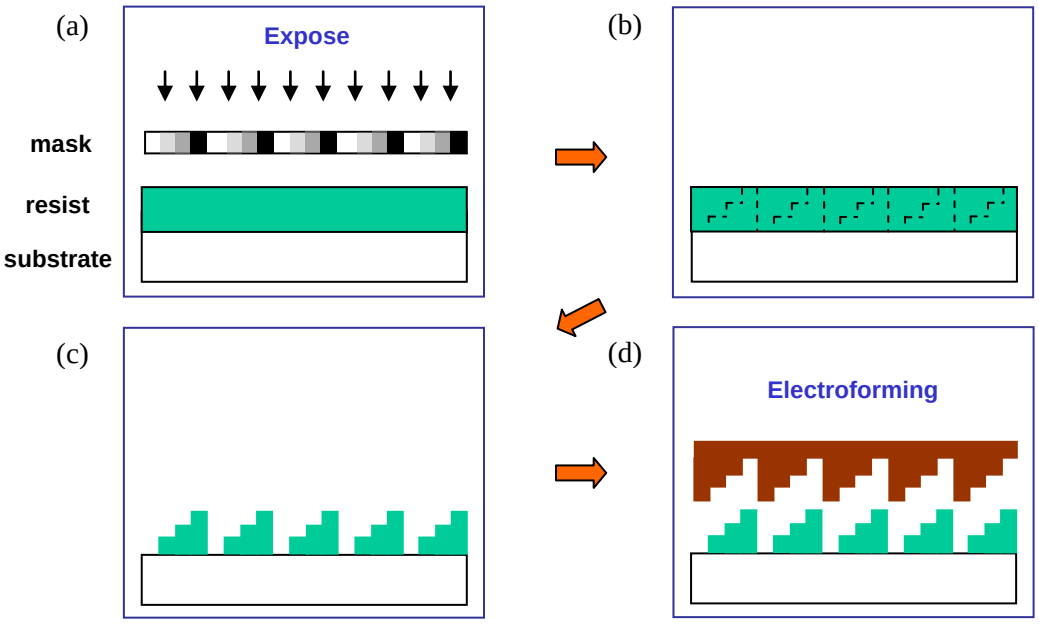

Figure 3.3: Fabrication process flow for blazed diffraction grating using gray-scale photolithography. (a) Photoresist coating and pattern exposure. (b) Areal image of the pattern in Photoresist. (c) Photoresist removal. (d) Photoresist profile transfer by Electroforming.

The problem of misalignment for the conventional method described in the previous section can be resolved by using a high-energy beam sensitive photomask with a gray-scale optical density value (Figure 3.3). This method requires only one gray-scale photomask and one exposure step to form the blazed profile directly in the photoresist without the need of etching steps. The resist profile is transferred into a master grating by electroforming to prevent any distortion of the surface profile by carrying out etching processes. However, the cost of the gray-scale photomask is very

high and the electroforming process adds one process step. Therefore, this method is not suitable for cost-effective energy-efficient window applications.

3.2.3.3. Step-and-Expose Photolithography

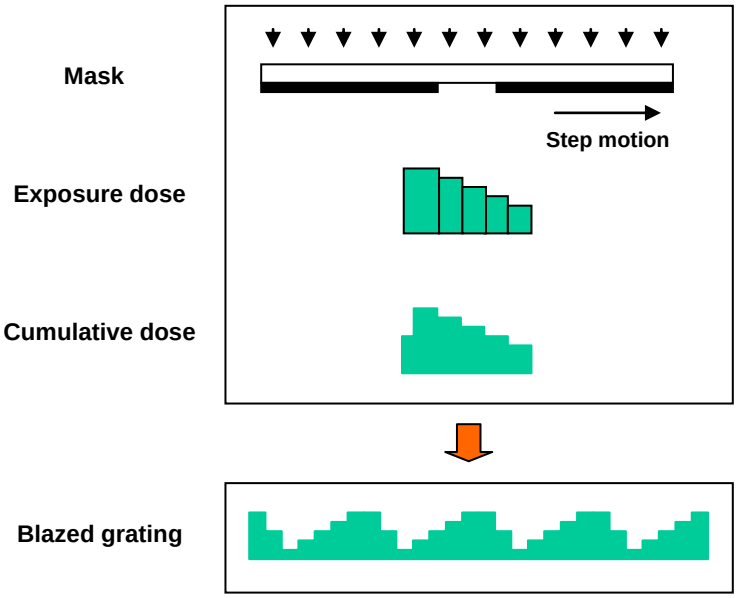

Figure 3.4: Schematic illustration of the step-and-expose photolithography method for the fabrication of a blazed diffraction grating.

In another fabrication method described in the literature [52], only one binary photomask is used to form the blazed profile in the resist by utilizing a step-and-expose procedure (Figure 3.4) – this method is more cost-effective than the gray-scale photolithography approach described in the previous section. In this method, the exposure dose given is such that the cumulative dose falls on the linear part of the resist sensitivity curve. After the first exposure, the substrate is moved and the next exposure is made. This step-and-expose procedure is then repeated for the same distance (pitch) of the grating.

However, the throughput of this method is low because each groove is formed one after the other. This method can be enhanced by using a mask with multiple openings even though the pitch of the grating is then fixed. We can also eliminate the mask and stepper from the process by using maskless systems such as e-beam lithography or optical lithography with a spatial light modulator.

Again, the photoresist surface profile can be transferred into a mold by electroforming and subsequent gratings can be replicated economically using a variety of plastics including polymethyl methacrylate (PMMA) and polycarbonate (PC). In general, the masters for replication are made of nickel. The surface of the master is then stamped into the plastic by compression molding, which uses heat and pressure to form grooves with a good feature quality (Figure 3.5). This technique is similar to the injection compression molding method used for making audio and video compact disks.

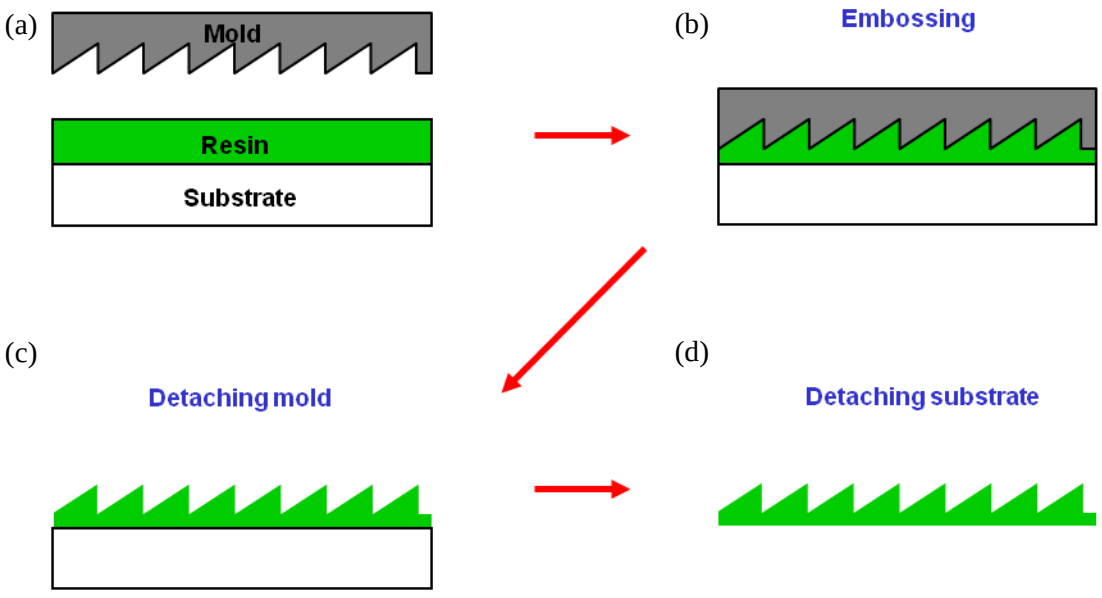

Figure 3.5: Replication process flow for the fabrication of a blazed diffraction grating from a master grating. (a) Resin deposition, (b) Compression molding, (c) Detaching mold, (d) Detaching substrate.

3.3. Theoretical Considerations of Blazed Transmission Diffraction Gratings

The following sections describe the theoretical considerations for diffraction gratings that are important in determining the blazed angle and maximizing the efficiency for blazed gratings.

3.3.1. Diffraction Grating Equation

Diffraction is a phenomenon caused by the propagation of waves. By the Huygens-Fresnel principle, each point on a wavefront that is unobstructed acts as a new source of secondary spherical wavelets [40-42]. The amplitude of the optical field at a distant point can be determined by the superposition of these newly generated spherical wavelets. The diffraction pattern caused by an optical disturbance (aperture) is the result of the addition of the amplitude and phase of all individual waves (Huygen's wavelets) which will have a series of minimum and maximum values.

The Fraunhofer diffraction criterion applies when the source and observation points are very far away (far-field) from the disturbance while the Fresnel diffraction criterion applies when the source and observation points are close to the disturbance (near-field). This is also determined by the Fresnel number [42]

$$F = \frac{w^2}{d\lambda} \tag{3.1}$$

where w is the size of the aperture, d is the distance between the aperture and the observation point, and λ is the incident wavelength.

Fresnel diffraction applies when $F \geq 1$ and Fraunhofer diffraction applies when $F \ll 1$. Because the interest of this work lies in the far-field diffraction condition, further discussion below is focused on the Fruanhofer diffraction regime.

The optical field at an observation point P(r) is given by [40]

$$\tilde{E}(r) = \frac{i}{\lambda}\tilde{E}_{inc}(r')\frac{e^{-ik|r-r'|}}{|r-r'|} \tag{3.2}$$

where $\tilde{E}_{inc}(r')$ is the incident field and r' is a general point in the opening (aperture) of an opaque screen.

Then the basic diffraction integral for the total optical field at an observation point P(r) is

$$\tilde{E}(r) = \frac{i}{\lambda}\iint_{\sum_0}\tilde{E}_{inc}(r')\frac{e^{-ik|r-r'|}}{|r-r'|}d\sigma \tag{3.3}$$

where $\sum_0$ is the open area of an opaque screen and $d\sigma$ is an infinitesimal element of surface area at the point r' in the opening $\sum_0$.

Starting from Equation 3.3, the general expression for the field within a single aperture is given as

$$\tilde{E}(r) = \frac{i}{\lambda}A\iint_{\sum_0}\frac{e^{-ik|R+R'|}}{RR'}d\sigma \tag{3.4}$$

where *A* is the amplitude of the incident wave at unit distance from the point source, *R* is the distance between the point source and the aperture, and *R′* is the distance between the aperture and the observation point.

By assuming the Fraunhofer approximation and inserting a transmission function which represents the shape of the aperture, Equation 3.4 yields

$$\tilde{E}(r) = \frac{i}{\lambda}\tilde{E}(O)\frac{e^{-ikR_0'}}{R_0'}\iint_{-\infty}^{\infty} t(x',y')e^{-2\pi i(ux'+vy')}dx'dy' \tag{3.4}$$

$$\text{with} = \frac{\alpha-\alpha'}{\lambda}, v = \frac{\beta-\beta'}{\lambda}$$

where $\tilde{E}(O) = \mathrm{A}\frac{\mathrm{e}^{-\mathrm{ikR}_0}}{\mathrm{R}_0}$ is the complex amplitude of the incident field at the origin O and $t(x',y')$ is the transmission function.

As an example, the transmission function of a rectangular aperture is

$$\mathrm{t}(\mathrm{x}',\mathrm{y}') = 1 \quad \text{if } \mathrm{x}' < \mathrm{x}_0 \text{ and } \mathrm{y}' < \mathrm{y}_0$$
$$\mathrm{t}(\mathrm{x}',\mathrm{y}') = 0 \quad \text{otherwise;}$$

and the flux density at P(r) is given by

$$E_e(r) = nC\left|\tilde{E}(r)\right|^2 \tag{3.5}$$

where $\left|\tilde{E}(r)\right|$ is the peak electric field strength, n is the index of refraction, and *C* is a constant.

Then, by inserting the transmission function into Equation 3.4 and from Equation 3.5, we obtain the flux density of a rectangular aperture at P(r),

$$E_e(r) = E_e(O)\frac{16x_0^2y_0^2}{\lambda\left(R_0'\right)^2}I_x^2I_y^2 \tag{3.6}$$

with $I_x = \frac{1}{2x_0}\int_{-x_0}^{+x_0} e^{-2\pi i u x'} dx' = \frac{\sin 2\pi u x_0}{2\pi u x_0}$, $I_y = \frac{1}{2y_0}\int_{-y_0}^{+y_0} e^{-2\pi i u y'} dy' = \frac{\sin 2\pi u y_0}{2\pi u y_0}$

where $E_e(O) = nC\left|\tilde{E}(O)\right|^2$ is the flux density of the incident beam at the center of the aperture O.

Now, a diffraction grating is an array of identical apertures. As each aperture in an array contributes to the total diffracted electric field, the assumption for the Fraunhofer diffraction criterion gives the total field at P(r) to be the sum of the phase factors times the field from a single aperture.

We start with two identical apertures, one at O for which the field is $\widetilde{E}(r)$ and one at O' for which the field is $\widetilde{E}(r)e^{i\Delta}$.

Here the phase factor is,

$$e^{i\Delta} = exp\left\{\frac{2\pi i}{\lambda}[m_1(\alpha - \alpha') + m_2(\beta - \beta')]\right\} \tag{3.7}$$

where m_1 is the distance between the two apertures in the x' direction, and m_2 is the distance in the y' direction.

Then, the resultant total field at P(r) is

$$\tilde{E}(r)_{Total} = \tilde{E}(r) + \tilde{E}(r)e^{i\Delta} = \tilde{E}(r)(1 + e^{i\Delta}). \tag{3.8}$$

Let $\widetilde{E}(r) = D\widetilde{E}(O)$ with the incident field at O to be $\widetilde{E}(O) = A\frac{e^{-ikR_0}}{R_0}$, where $D = \frac{i}{\lambda}\frac{e^{-ikR_0'}}{R_0'}\iint_{-\infty}^{\infty} t(x', y')\exp\left\{-\frac{2\pi i}{\lambda}[(\alpha - \alpha')x' + (\beta - \beta')y']\right\}dx'dy'$ is the term that

corresponds to the diffraction caused by a single aperture which is described by the transmission function $t(x', y')$. Therefore, for the total field at P(r), we have

$$\tilde{E}(r)_{Total} = \tilde{E}(O) \cdot D \cdot I \tag{3.9}$$

where $I = 1 + e^{i\Delta}$ is the term that corresponds to the interference caused by multiple apertures.

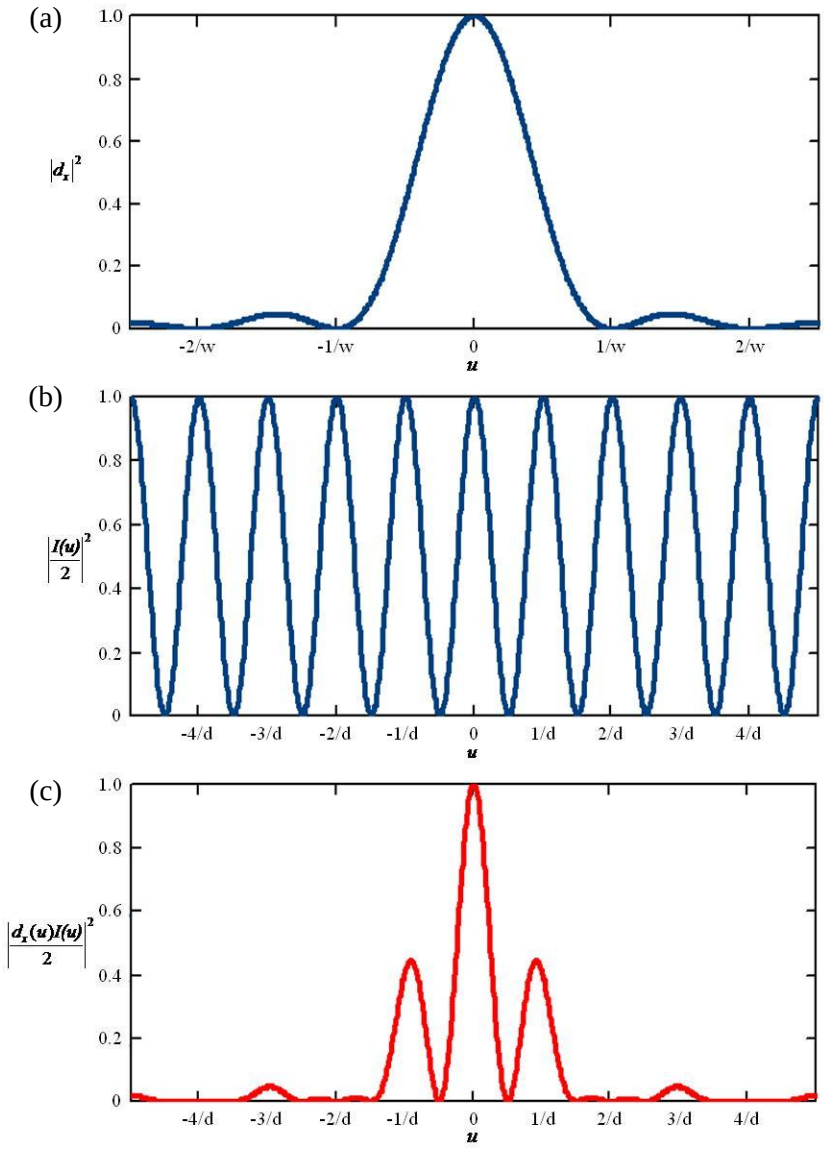

Figure 3.6: Theoretical plot of (a) the diffraction factor, (b) the interference factor, and (c) the combined flux density in the case of double-slit aperture.

The diffraction pattern we observe is the flux density at P(r) which is,

$$E_e(r) = E_e(O) \cdot |D|^2 \cdot |I|^2. \tag{3.10}$$

If we consider the diffraction pattern by an array of N identical slits where the width of a slit is w, the height is h, and they are separated by d, then the flux density is,

$$E_e(r) = \frac{E_e(O)}{\lambda^2 R_0'^2}(2whN)^2 d_y{}^2 \left(\frac{sin\pi uw}{\pi uw}\right)^2 \left(\frac{sin\,\pi udN}{N\,sin\,\pi ud}\right)^2 \tag{3.11}$$

where $D = \frac{\mathrm{i}}{\lambda}\frac{\mathrm{e}^{-\mathrm{ikR}_0'}}{\mathrm{R}_0'} 2\mathrm{whd_x d_y}$, with $d_x = \frac{\sin\pi\mathrm{uw}}{\pi\mathrm{uw}}, u = \frac{\alpha-\alpha'}{\lambda}$, and $d_y = \frac{\sin\pi\mathrm{vh}}{\pi\mathrm{vh}}, v = \frac{\beta-\beta'}{\lambda}$.

For example, the diffraction pattern for two slits (N=2) is plotted in Figure 3.6 (c) which is a combined plot of the diffraction factor (Figure 3.6 (a)) and the interference factor (Figure 3.6 (b)).

Now, a diffraction grating is composed of large numbers of slits that are equally spaced in an array. Each diffraction order that appears for a grating is a maximum flux density condition, which is given by

$$ud = \text{integer}$$

or

$$(\alpha - \alpha') = \frac{m\lambda}{d} \quad \text{where } m=0, \pm1, \pm2, \ldots \tag{3.12}$$

By defining the angles $\theta_x=\sin^{-1}\alpha$, $\theta_x'=\sin^{-1}\alpha'$, $\theta_y=\sin^{-1}\beta$, and $\theta_y'=\sin^{-1}\beta'$, and if θ_y and θ_y' are negligible (normal to the grating plane), then θ_x represents the angle of

incidence and θ_x' represents the angle of diffraction which will turn Equation 3.12 to the form of the familiar grating equation,

$$d(\sin\theta_x - \sin\theta_x') = m\lambda. \tag{3.13}$$

In the case of a blazed diffraction grating, the optical path length difference contributes to a phase lag of

$$\Delta = \frac{4\pi x_\perp' \tan\theta_b}{\lambda} \tag{3.14}$$

where $x_\perp' = \mathrm{x}'\cos\theta_\mathrm{b}$ represents the distance along the reflecting facet and the diffraction factor $\mathrm{d_x}$ is

$$d_x = \frac{\sin\pi u' d}{\pi u' d},\ u' = u + \frac{2\sin\theta_b}{\lambda} = \frac{(\alpha-\alpha')+2\sin\theta_b}{\lambda}. \tag{3.15}$$

Compared to the slit-type diffraction grating where $\alpha' = \alpha$, $\mathrm{d_x}$ describes a single-slit pattern for a slit of width d centered about $\alpha' - \alpha = 2\sin\theta_\mathrm{b} = 2\alpha_\mathrm{b}$.

Figure 3.7 shows the new diffraction factor together with the interference factor and their combined plot. The spacing between the peaks of the interference factor and the zeros of the diffraction factor are now both 1/d. The combined plot shows the overall pattern is asymmetrical about zero order, meaning most of the energy that is incident on a blazed diffraction grating is available in the non-zero order region. The peak of the diffraction pattern synchronizes with an interference maximum when $\lambda = \lambda_\mathrm{b}$, $\lambda_\mathrm{b}/2$, $\lambda_\mathrm{b}/3$, and so on, while all other interference maxima are eliminated by zeros in the diffraction pattern.

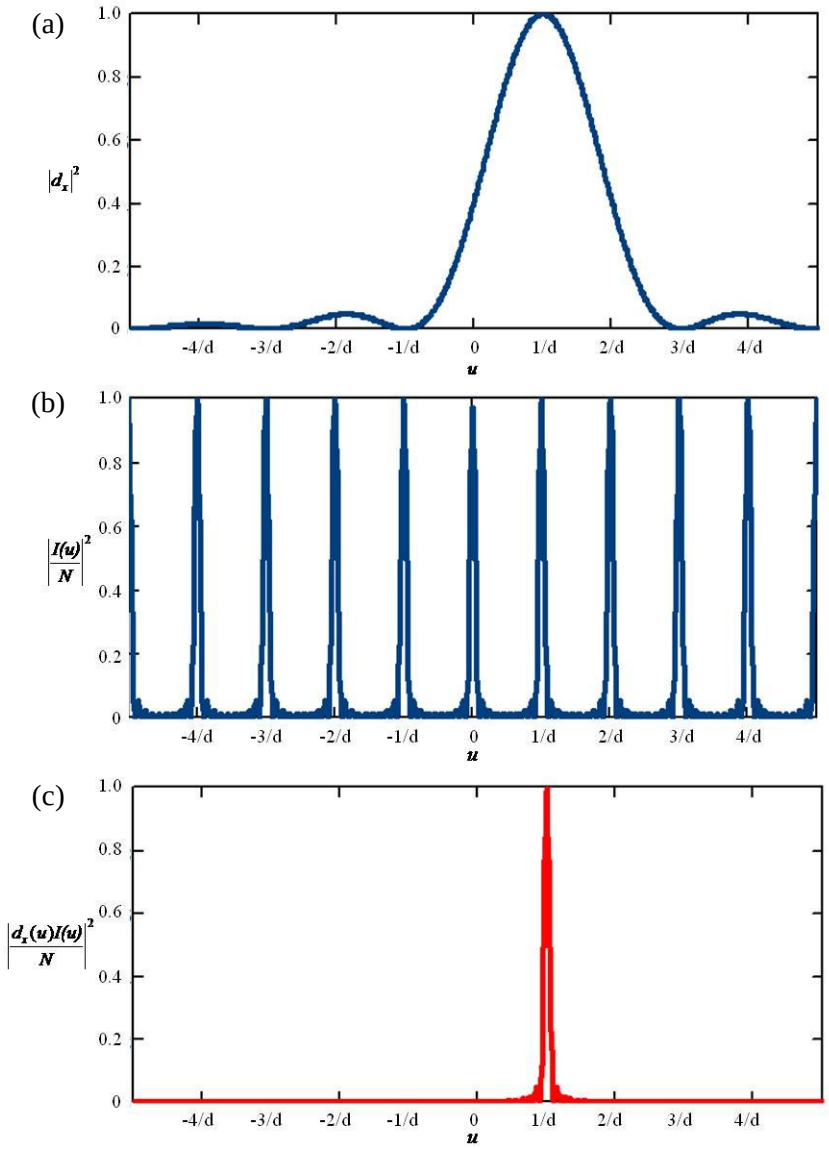

Figure 3.7: Theoretical plot of (a) the diffraction factor, (b) the interference factor, and (c) the combined flux density in the case of blazed diffraction grating.

3.3.2. Determination of the Blaze Wavelength

The phenomenon in which most of the incident energy on a diffraction grating with specific configurations can be concentrated into a specific diffraction order (angle) is called blazing. A diffraction grating that follows this specific configuration is said to

be in “blaze condition” and the wavelength that diffracts into this specific diffraction order (angle) with the highest efficiency is known as the blaze wavelength.

In the case of a blazed transmission diffraction grating, the highest diffraction efficiency is realized when the exit angle determined by refraction through the grating medium (as determined by Snell’s law) and the exit diffraction angle (as determined by the grating equation) are identical. The condition where these requirements are met can be determined precisely. Thus, the blaze wavelength can be analytically determined for any grating configuration by calculating both the exit refraction angle and the exit diffraction angle as a function of wavelength and then finding the wavelength for which these two exit angles are identical. In a similar manner, the ideal grating configurations can also be determined for a desired target blaze wavelength (e.g., NIR wavelengths in the 700 - 1500 nm range for our window system application) by varying the grating parameters to find solutions that maximize the blazing efficiency when the difference between the exit refraction angle and the exit diffraction angle is negligible.

As an illustration of the benefits of the optical modeling capability, Figure 3.8 shows multiple solutions, (i.e., blazed grating configurations) for a 1 μm target wavelength by varying each parameter by 1° increments and calculating the solutions where the difference between exit refraction angle and exit diffraction angle is less than 0.1°. Note that ideal blazed diffraction gratings suitable for a range of low to high angles of incidence can be configured by adjusting both the grating pitch and blaze angle.

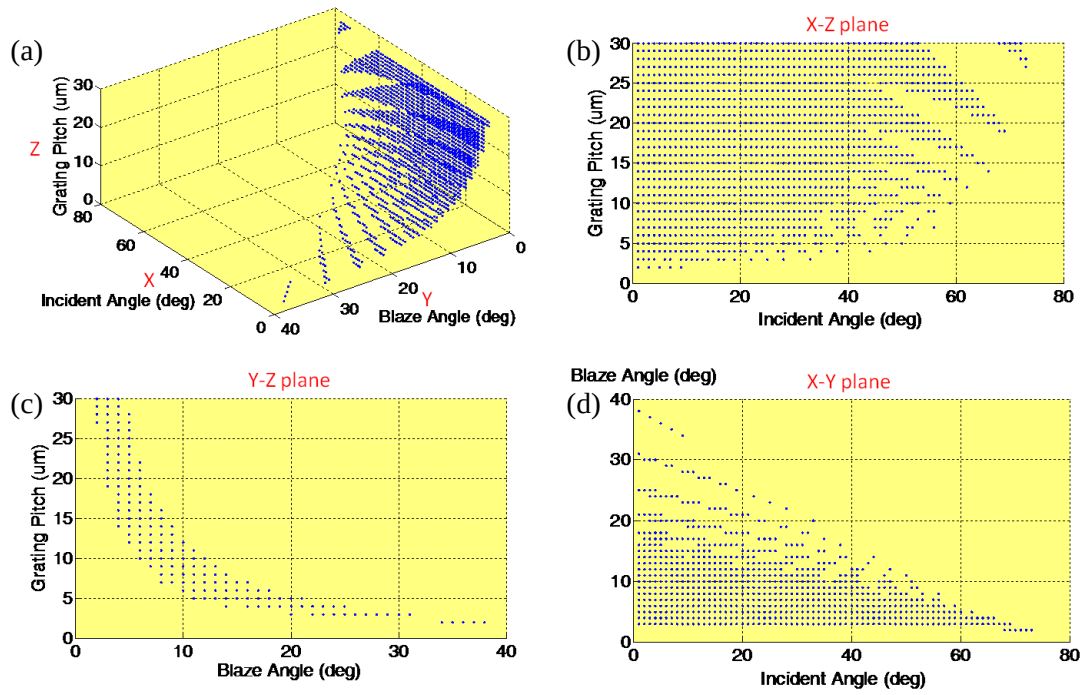

Figure 3.8: Optical modeling solutions to peak blazing efficiency for 1 μm target wavelength depending on three grating parameters. (a) Combination of grating pitch, incident angle, and blaze angle. (b) Blaze angle as a function of grating pitch and incident angle. (c) Incident angle as a function of grating pitch and blaze angle. (d) Grating pitch as a function of blaze angle and incident angle.

3.3.3. Dependence on Grating Period, Groove Angle, and Angle of Incidence

A diffraction grating configuration can be varied by the following parameters: refractive index of grating material, blaze wavelength, grating period, groove angle, and angle of incidence. The dependencies of the parameters on each other are correlated such that an optimum configuration can be found for a given irradiance condition.

Figure 3.9 shows the light pathway as a ray travels through a grating groove with the angles shown in detail to determine their relationship for high-efficiency blazing : θ_i is the angle of incidence on the grating plane, θ_{r1} is the angle of refraction at the first

interface, α is the groove angle, θ_{r2} is the angle of refraction at the second interface, and θ_b is the -1st order diffraction (blaze) angle.

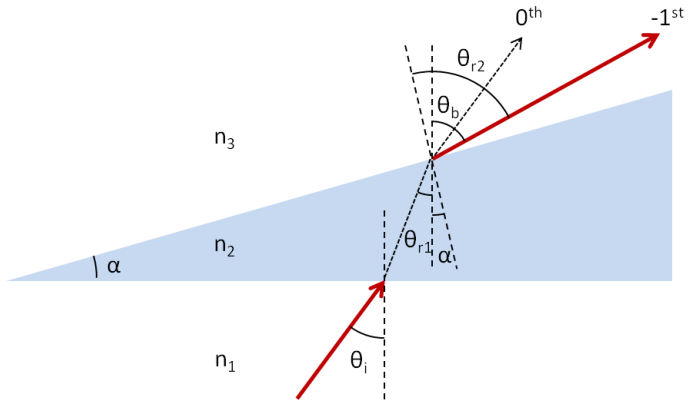

Figure 3.9: Optical pathway of the incident light on a triangular groove in the case of high-efficiency blazing: Refraction angle determined by Snell's law and -1st order diffraction angle determined by grating equation are identical.

To design a proper grating configuration for a target wavelength (λ_b), (i.e., visible or near-infrared for the smart window system), to be blazed at the -1st diffraction order (m=-1), the groove angle (α) needs to be determined for a given grating pitch (d). For transmission gratings, the desired groove (blaze) angle (α) can be calculated by applying Snell's law at the second interface since the blazing occurs when the direction of refraction is same as the diffraction angle. Therefore, we obtain the following relationship,

$$n_2 \, sin(\theta_{r1} + \alpha) = n_3 sin(\theta_b + \alpha). \tag{3.16}$$

After expanding Equation 3.16 and dividing it by cosα, we get

$$n_2 \, [sin(\theta_{r1}) + cos(\theta_{r1}) tan(\alpha)] = n_3 [cos(\theta_b) tan(\alpha) + sin(\theta_b)] \tag{3.17}$$

Rearranging Equation 3.17 returns a generallized equation for the groove angle,

$$\alpha = tan^{-1}\left[\frac{n_2\, sin(\theta_{r1}) - n_3\, sin(\theta_b)}{n_3\, cos(\theta_b) - n_2\, cos(\theta_{r1})}\right] \tag{3.18}$$

where $\theta_{r1} = \sin^{-1}\left[\frac{n_1 \sin(\theta_i)}{n_2}\right]$ and $\theta_b = \sin^{-1}\left[\frac{m\lambda}{d} - \sin(\theta_i)\right]$.

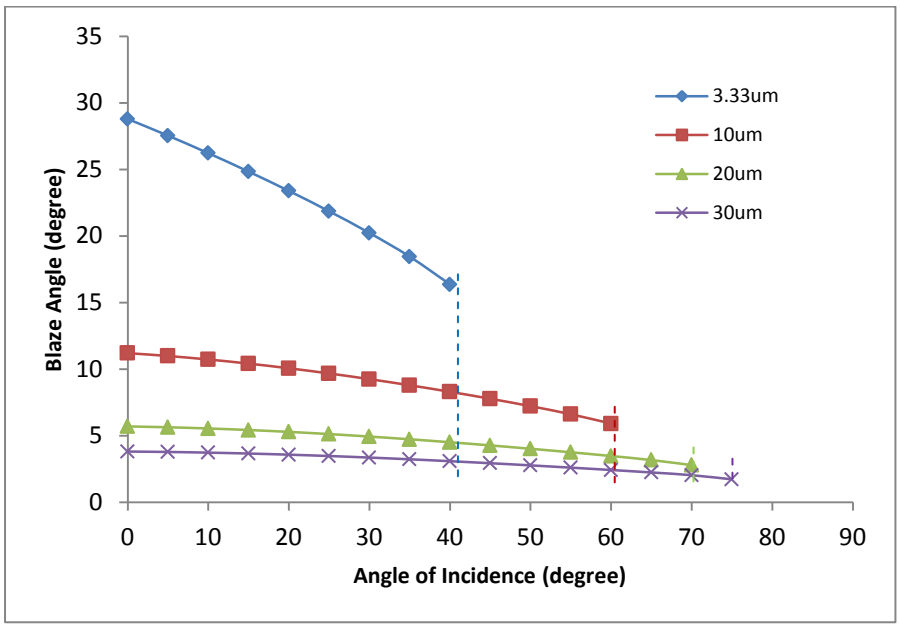

Figure 3.10: The effect of grating period on blaze angle as a function of incident angle.

Figure 3.10 shows the relationship between the desired blaze angles as a function of angle of incidence for 1 μm target wavelength and compares the effect of grating periods. The 1st order diffraction angle of the higher spatial frequency grating is larger and thus requires a steeper groove angle. However, this high spatial frequency grating will undergo total internal reflection (TIR) on the groove side by its steep groove angle and thus irradiance at a large angle of incidence cannot be blazed. Therefore, to address

higher angles of incidence, a lower spatial frequency grating is desired, which requires a smaller groove angle to meet the blazing condition. As the angle of incidence from the solar irradiance changes through the day, it will be possible to dynamically adjust the grating period and groove angle to blaze the heat generating near-infrared wavelengths accordingly. Chapter 4 describes a method to achieve this using an electrically controllable optical medium.

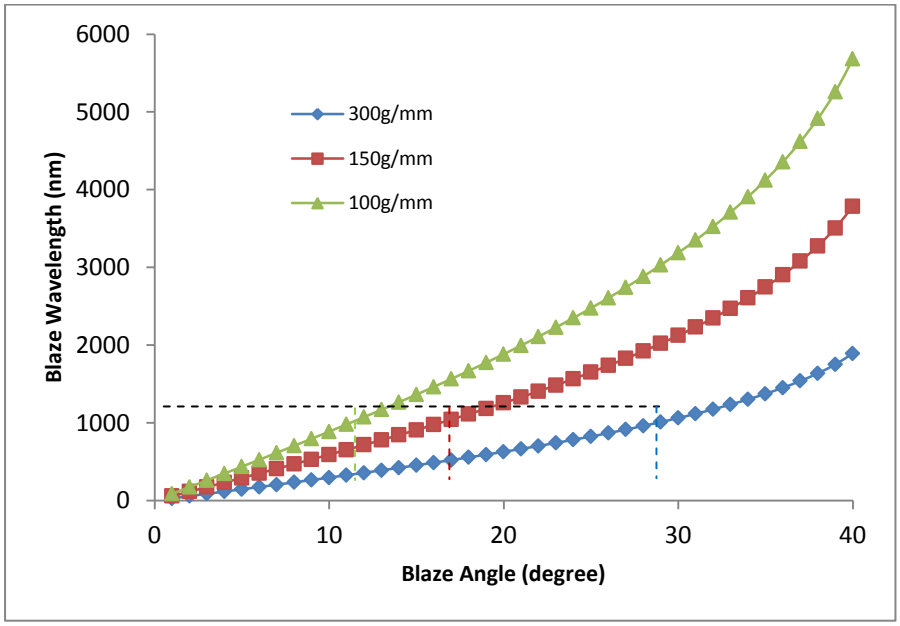

Figure 3.11: The effect of grating period on blaze wavelength as a function of blaze angle.

Figure 3.11 is a combined plot of the relationship between the blaze wavelength, the grating period, and the groove angle. First, for a target wavelength to be blazed, a higher groove angle is required as the spatial frequency of the grating period increases. Second, the blazing wavelength increases as the groove angle increases for a given grating period. Finally, the blazing wavelength increases as the special frequency of the grating period decreases for a given groove angle.

Now, as we are interested in blazing the near-infrared wavelength band, a 1 μm target wavelength can be blazed to its first diffraction order by having a transmission grating which has a groove angle of 11.20°, 16.35°, and 28.78° for a grating period of 100 grooves/mm, 150 grooves/mm, and 300 grooves/mm, respectively, at a normal angle of incidence.

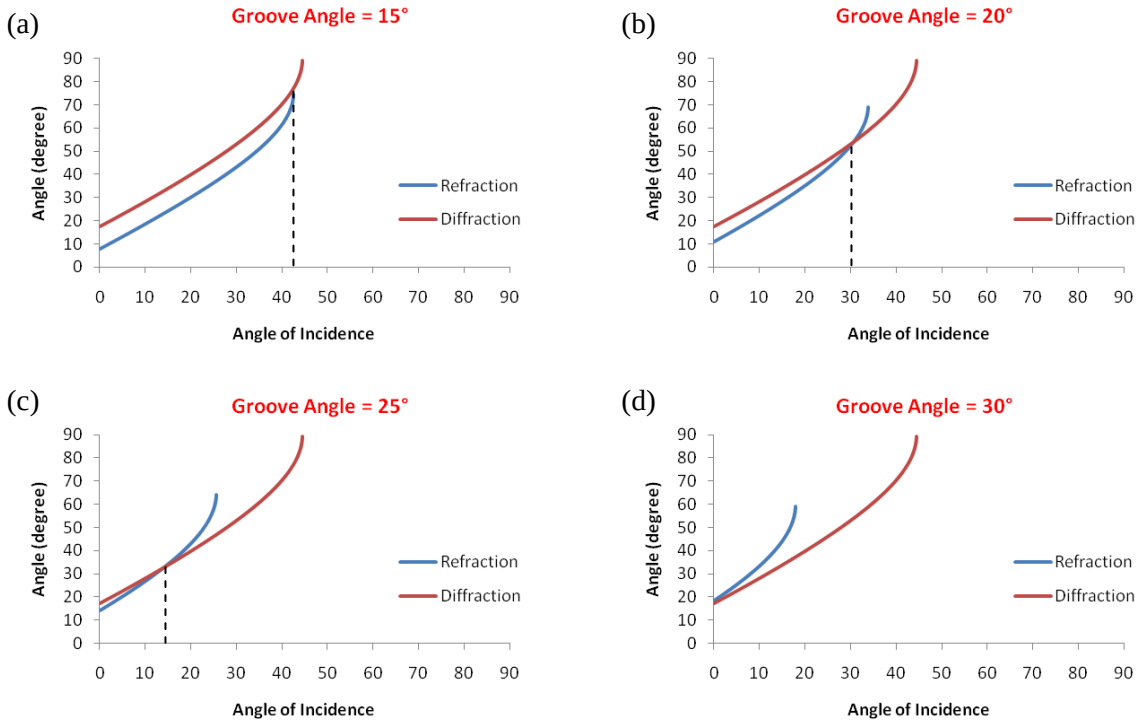

Figure 3.12: The effect of groove angles on the angle of incidence for a 1 μm target wavelength incident on a 300 grooves/mm (3.33 μm pitch) grating. (a) Weak blazing at 42.57°. (b) Strong blazing at 30.67°. (c) Strong blazing at 14.42°. (d) Moderate blazing at 0°.

Finally, we inspect the effect of groove angle on the angle of incidence for a 1 μm target wavelength that is incident on a 300 grooves/mm (3.33 μm pitch) grating. As shown in Figure 3.12, we plot both the refraction angle and the diffraction angle to find the crossing point which gives the angle of incidence that is blazed. There is very weak blazing when the groove angle is too shallow (Figure 3.12 (a)). By increasing the

groove angle, only rays with a high angle of incidence are able to blaze (Figure 3.12 (b)). Note that the range of incident angles that blaze increases as the angle of incidence decreases (Figure 3.12 (c)). The final graph shows moderate blazing for a normal angle of incidence (Figure 3.12 (d)). This tells us that the blazing of a specific target wavelength for different angles of incidence can be achieved by adjusting the groove angles accordingly. An electrically controllable and switchable grating will be ideal to accommodate this change, which is discussed in Chapter 4.

3.4. Blazed Transmission Diffraction Grating Efficiency Measurement

3.4.1. Efficiency Measurement

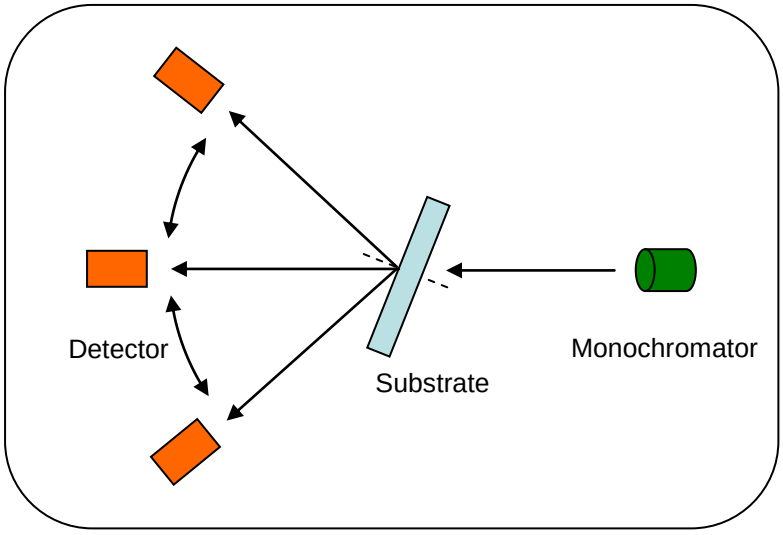

Figure 3.13: Optical components of the Variable Angle Spectroscopic Ellipsometer (VASE) for the measurement of diffraction grating performance.

Diffraction efficiency measurement of transmission blazed gratings is carried out using a Variable Angle Spectroscopic Ellipsometer (VASE) which is equipped with all

necessary optical components that are essential for characterizing diffraction grating performance (Figure 3.13) : An input light source which provides wavelengths ranging from the ultraviolet region to the visible and near-infrared region, a substrate holder that rotates along the optical axis from 0° to 90° which enables precise measurement for angled incidence, and a sweeping detector that measures only positive angles (negative diffraction orders).

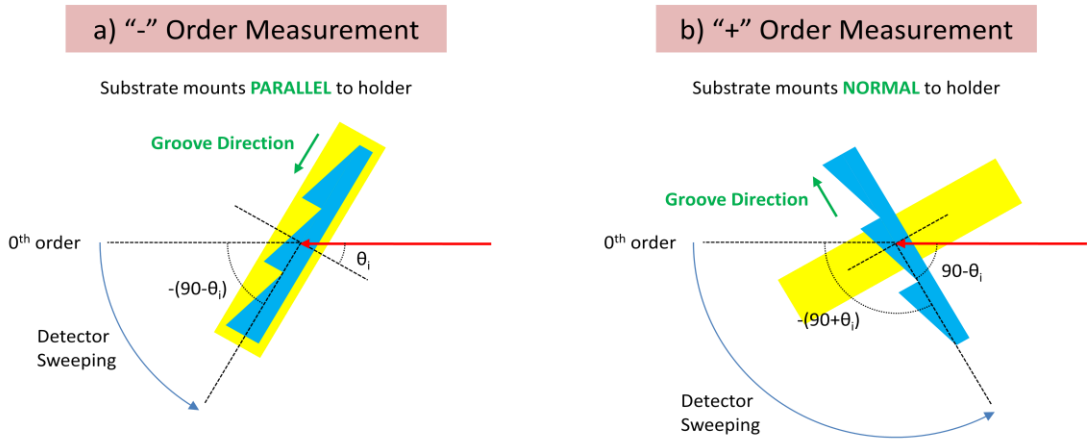

Parameters Setting	
Incidence Angle	θ_i
Sweeping Angle	$-(90-\theta_i)$

Parameters Setting	
Incidence Angle	$90-\theta_i$
Sweeping Angle	$-(90+\theta_i)$

Figure 3.14: Schematic diagram of the modification of the substrate holder and corresponding parameter settings on the Variable Angle Spectroscopic Ellipsometer (VASE) to measure both (a) "-" diffraction orders and (b) "+" diffraction orders.

We modified the substrate holder to measure also negative angles (positive orders) as shown in Figure 3.14. The diffraction orders are measured by scanning the detector perpendicularly to the output (diffracted) light for a peak signal.

3.4.2. Results and Discussion

This section describes the measured efficiency behavior of commercially available physical gratings of various configurations that provides an insight into the grating optical properties. Gratings we selected to investigate include a) holographic grating (1000 grooves/mm), b) visible blazed gratings (1200 grooves/mm, 600 grooves/mm, and 300 grooves/mm), and c) near-infrared blazed grating (300 grooves/mm). We used Atomic Force Microscopy (AFM) to precisely image the groove profile from which the grating pitch and blaze angle are obtained.

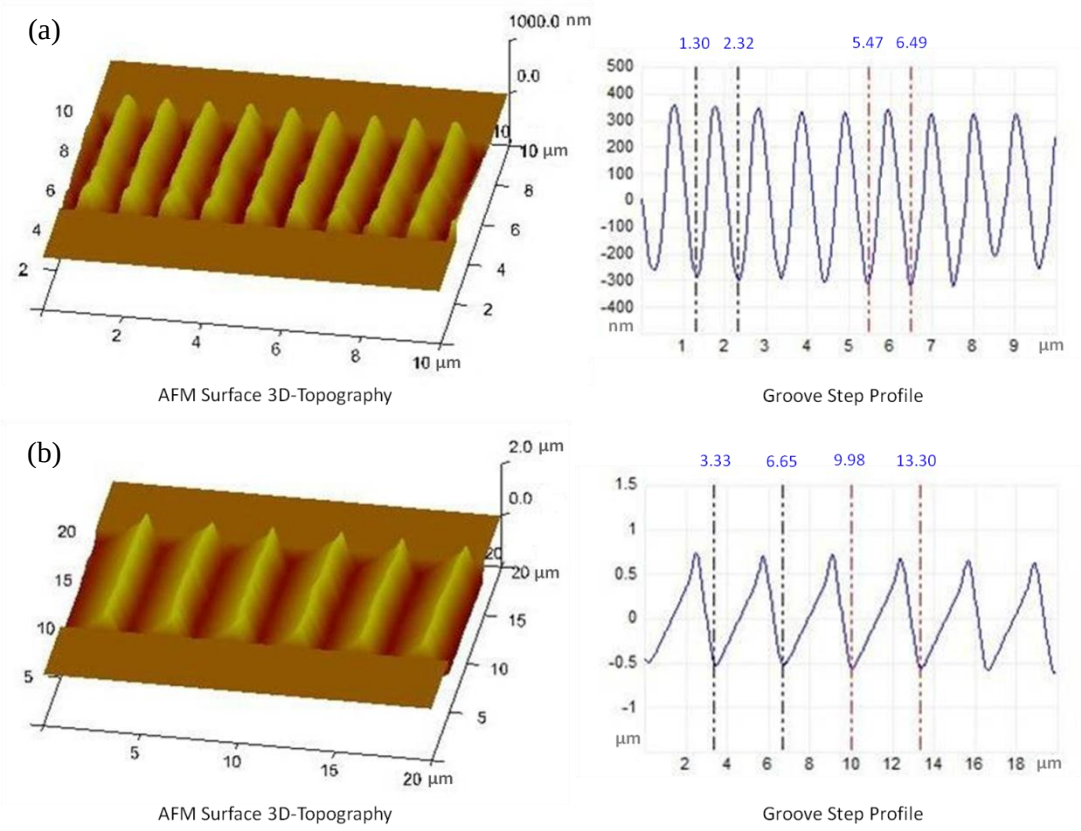

Figure 3.15: Atomic force microscopy image of diffraction grating surface profile. (a) Holographic grating. (b) Blazed grating.

As an example, Figure 3.15 shows the surface image obtained by AFM for a visible holographic grating (a) which has a sinusoidal groove profile with a grating period measured to be 1.02 μm (approximately 1000 grooves/mm) and the surface image for a ruled grating (b) with a triangular groove profile, a grating period measured to be 3.32 μm (approximately 300 grooves/mm), and a groove angle of 31.13°.

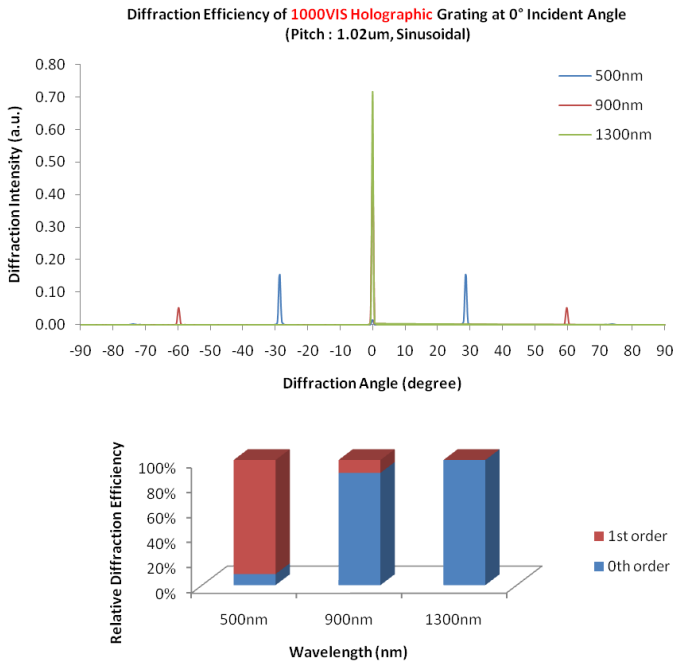

Figure 3.16: Diffraction peak measurement on a 1000 grooves/mm (1 μm pitch) visible holographic grating with relative diffraction efficiency of the 0^{th} and 1^{st} order.

After the groove profile is measured and the related parameters are determined, diffraction intensities are measured using VASE as described in the previous section. Figure 3.16 shows the diffraction intensities of the visible holographic grating measured for three wavelengths where the grating pitch is 1.02 μm. First, we observe that the highest diffraction intensities for the two wavelengths picked from the near-infrared spectrum are in the 0^{th} order but for the wavelengths picked from the visible spectrum

are in the 1st order. The 500 nm wavelength, which is half of the grating pitch, shows very strong 1st order diffraction. However, because of the symmetrical groove profile of the holographic diffraction grating, both -1st and +1st diffraction orders appear strong, which means that these types of grating are not suitable for efficient separation of the near-infrared radiation from the visible radiation of the solar spectrum. Second, the diffraction angle increases as the wavelength increases, but diffraction becomes negligible as the wavelength (900 nm) approaches the grating pitch and no diffraction appears for wavelengths larger than the grating pitch (1300 nm). Note that any wavelengths larger than the grating pitch will have no diffraction at normal angle of incidence.

Figure 3.17 shows the diffraction intensities of the visible blazed grating measured for three wavelengths. The groove pitch for this grating is measured to be 833 nm. Because the grating pitch is smaller than the visible holographic grating, the diffraction angle for each wavelength is larger. Again, diffraction becomes negligible as the wavelength (700 nm) approaches the grating pitch and no diffraction appears for the wavelength larger than the grating pitch (900 nm) as in the case of the visible holographic grating. However, the -1st order diffraction appears stronger (blazed) than +1st order because of the triangular groove profile of the blazed diffraction grating which is a distinct property compared to the symmetrical holographic grating. This makes this type of gratings suitable for efficient spectral separation because all radiation can be redirected to one diffraction order (angle).

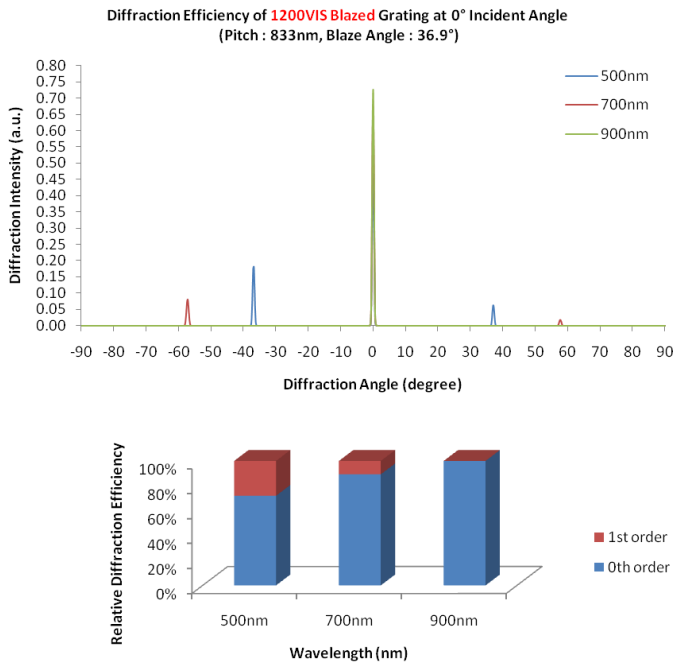

Figure 3.17: Diffraction peak measurement on a 1200 grooves/mm (833 nm pitch) visible blazed grating with relative diffraction efficiency of the 0^{th} and 1^{st} order.

We further investigated the dependence of blazing efficiency on the grating pitch along with the blaze angle. Figure 3.18 shows the diffraction intensities for the 600 grooves/mm (1.67 μm pitch) visible blazed grating and Figure 3.19 shows the diffraction intensities for the 300 grooves/mm (3.33 μm pitch) visible blazed grating. We observed the blazing of 500 nm visible wavelength to the 1^{st} order for the 1200 grooves/mm (833 nm pitch) visible blazed grating, but the intensity of 1^{st} order peak is relatively weak compared to the 0^{th} order diffraction. As the grating pitch increases, angular dispersion decreases but the blazing efficiency of the visible light (500 nm) is higher. However, the blazing efficiency of the near-infrared is also higher which is not desired for a visible blazed grating. Therefore, selection of an optimal visible blazed grating that will efficiently blaze the visible while the near-infrared passes through depends on the grating pitch and blaze angle.

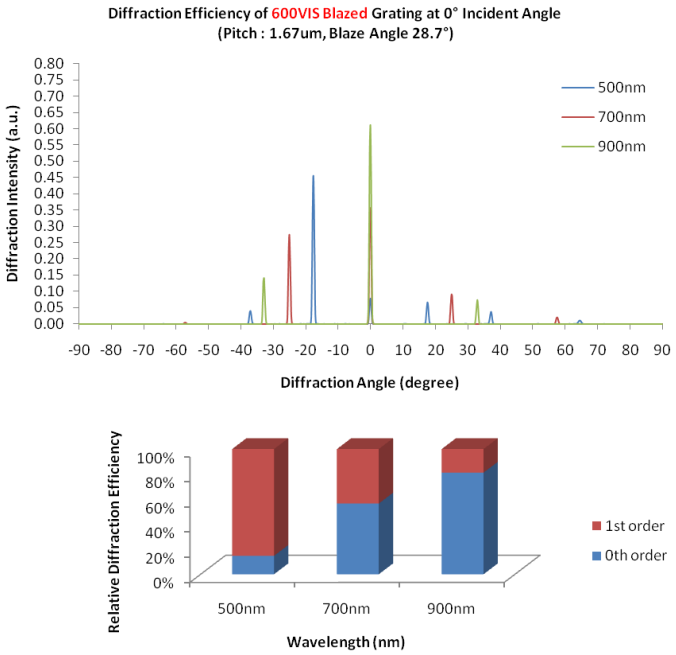

Figure 3.18: Diffraction peak measurement on a 600 grooves/mm (1.67 μm pitch) visible blazed grating with relative diffraction efficiency of the 0^{th} and 1^{st} order.

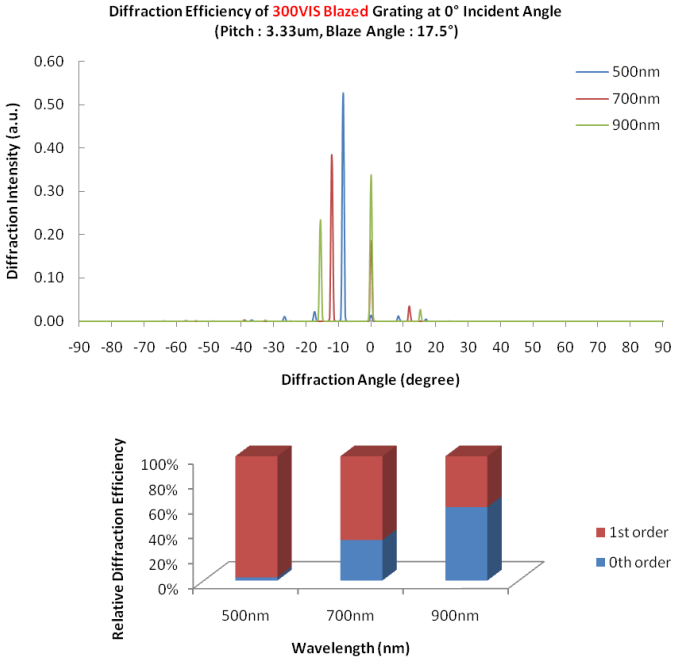

Figure 3.19: Diffraction peak measurement on a 300 grooves/mm (3.33 μm pitch) visible blazed grating with relative diffraction efficiency of the 0^{th} and 1^{st} order.

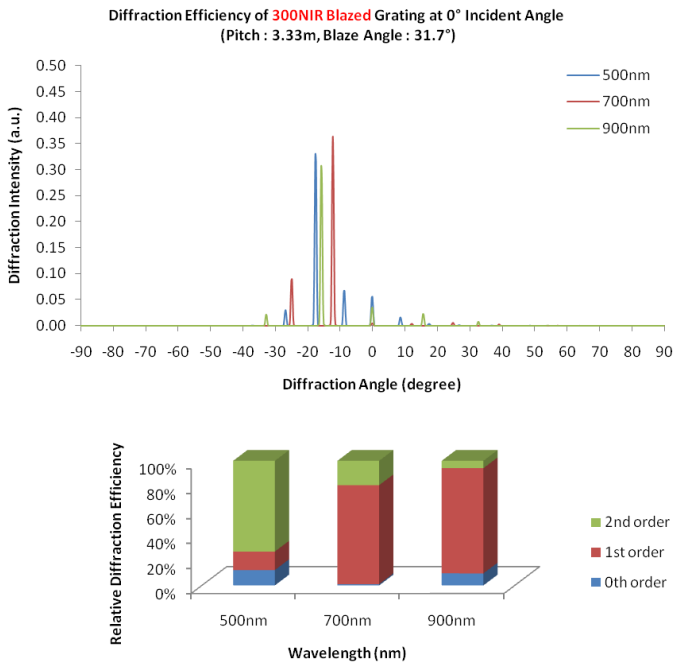

Figure 3.20: Diffraction peak measurement on a 300 grooves/mm (3.33 μm pitch) near-infrared blazed grating with relative diffraction efficiency of the 0^{th} , 1^{st}, and 2^{nd} order.

We further investigated a 300 grooves/mm (3.33 μm pitch) blazed grating with a blaze angle of 31.7° which is targeted for the near-infrared radiation (Figure 3.20). Note that the difference from the 300 grooves/mm (3.33 μm pitch) blazed grating targeted for the visible radiation is the blaze angle which is 17.5°. The shallower groove angle ensures that the blazing occurs for the visible spectrum. Another important fact that is observed is that the 2^{nd} order diffraction of the visible wavelength (500 nm) appears strong which lies at the 1^{st} order diffraction angle of the near-infrared wavelength (1000 nm). This is not desired for the smart window system, because only the near-infrared wavelength should be blazed. We have devised a novel solution to resolve this inherent limitation of a physical diffraction grating, which will be described in the following section.

Lastly, we plotted the 1st order blazing efficiency of the 600 grooves/mm visible blazed grating and the 300 grooves/mm near-infrared grating measured from our experimental setup which agrees well with theoretically calculated blazing efficiency as shown in Figure 3.21.

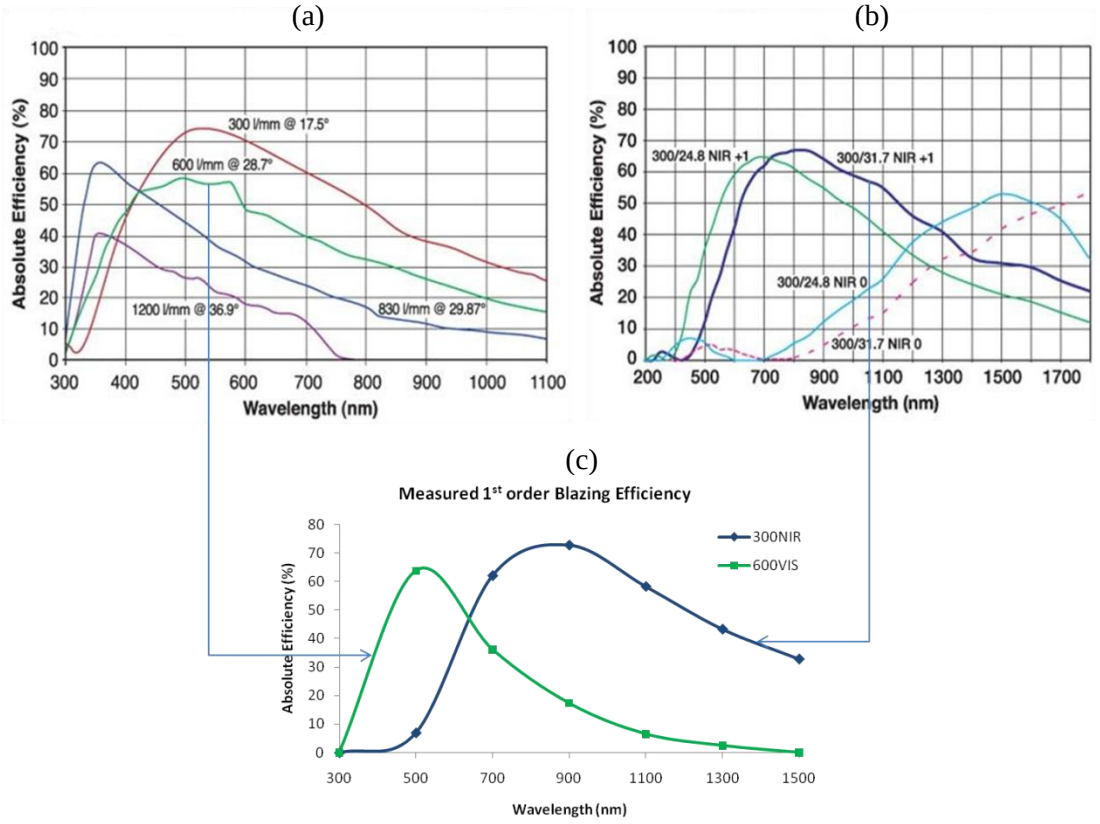

Figure 3.21: 1st order diffraction efficiency as a function of wavelength. (a) Visible blazed gratings (theoretical); (b) Near-infrared blazed gratings (theoretical); (c) Visible (600 grooves/mm) and near-infrared (300 grooves/mm) blazed gratings (experimental).

3.5. Multiple Physical Blazed Transmission Diffraction Gratings in Series

In light of the limitations of physical blazed gratings as described above, we investigate the use of multiple blazed gratings to separate the visible (VIS) and the near-infrared (NIR) spectral region of solar radiation. The first and most important requirement of our smart window is to separate the VIS spectral region of the solar radiation from its NIR region. In general, the VIS and NIR regions can be separated angularly by a simple diffraction grating. The efficiency of a diffraction grating is maximized if it is fabricated as a 'blazed' grating. The blaze condition is met when the relationship expressed by Equation 3.18 between the grating parameters, the wavelength, and the incident and transmitted optical rays is satisfied.

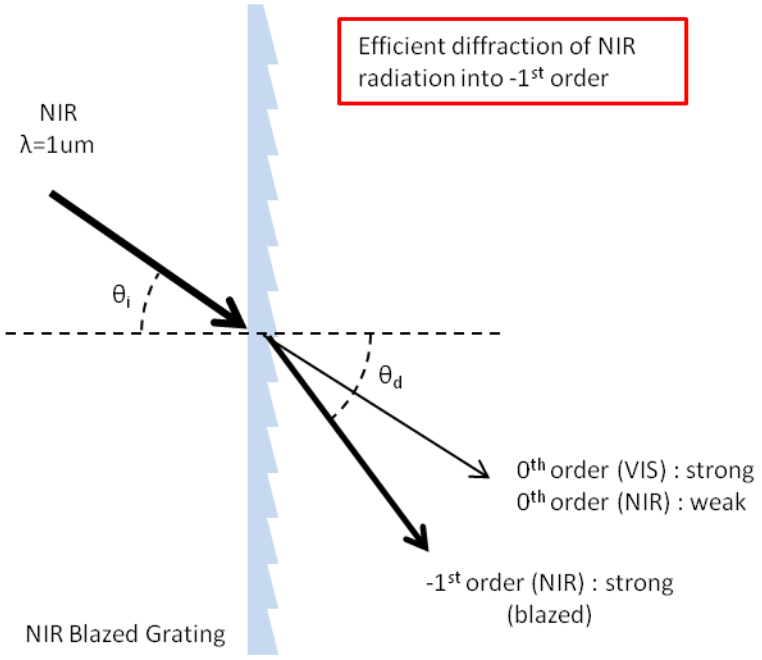

Figure 3.22: Schematic illustration of a near-infrared blazed grating incident with 1 μm near-infrared wavelength shows strong blazing efficiency for the 1st diffraction order.

A blazed grating is designed for a specific wavelength region such that most of the diffracted radiation for that wavelength region is directed into the first order, i.e., the diffraction efficiency is the highest for the first order and very low for the 0^{th}, 2^{nd}, and other orders, as illustrated in Figure 3.22.

If such a blazed grating is designed for the NIR region around 1µm, the NIR radiation will be diffracted into the first order (-1^{st} shown in Figure 3.22) with high efficiency, whereas the first order diffraction of the VIS radiation will not meet the blaze condition and therefore its efficiency will be very low. Thus, in principle, such a grating should enable effective angular separation of the VIS and NIR spectral components of the solar radiation. However, such is not the case because a problem arises due to the 2^{nd} diffraction orders, as follows.

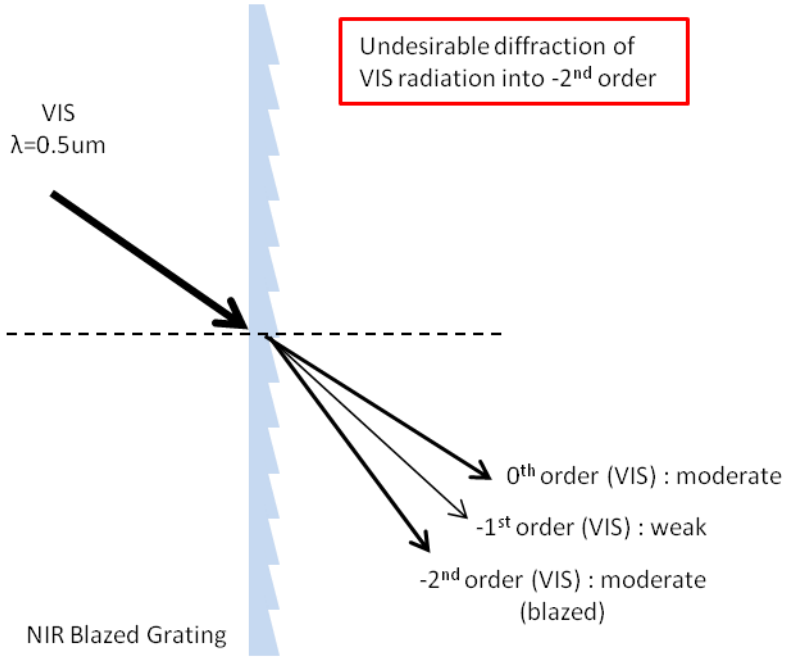

Figure 3.23: Schematic illustration of a near-infrared blazed grating incident with 0.5 µm visible wavelength shows moderate blazing efficiency for the 2^{nd} diffraction order.

A blazed grating that is designed for 1 μm in the 1st order (λ = 1 μm and m = 1 in Equation 3.13) also acts as a blazed grating in the 2nd order for 0.5 μm (λ = 0.5 μm and m = 2), albeit with a lower efficiency. Thus, as shown in Figure 3.23, the grating will diffract 0.5 μm radiation in 2nd order at the same angle as it diffracts 1 μm radiation in 1st order, thereby making their angular separation difficult. The same situation will be obtained for other wavelengths pairs that are apart by a factor of 2, e.g., 1.1 μm and 0.55 μm, 0.9 μm and 0.45 μm, etc. Thus, generally, the 1st order diffracted NIR radiation will be mixed with 2nd order diffracted VIS radiation.

A key technique employed to eliminate this problem is the use of two blazed diffraction gratings in series where the gratings are *blazed for different wavelength regions*, (e.g., one grating is optimized for the VIS region and the other blazed for NIR region), and their *blaze directions are opposite* to each other.

Figure 3.24 illustrates the technique. The solar radiation first passes through a diffraction grating that is blazed for, say, 0.5 μm, and its grooves are so oriented that the blaze occurs for the +1st order that deviates the diffracted rays counterclockwise from the incident direction, as shown in Figure 3.24 (a). As an example, such a grating can be fabricated with 600 grooves per millimeter (i.e., a grating pitch of 1.67 μm) and a blaze angle of 28.7 degrees, which will provide a deviation of +17.46 degrees for the 1st blaze order for the VIS blaze wavelength of 0.5 μm. We emphasize that for NIR incident radiation of 1 μm wavelength, this VIS blazed grating is very ineffective as a grating; therefore, most of the transmitted NIR radiation is directed into the 0th order, i.e., in the same direction as the incident rays.

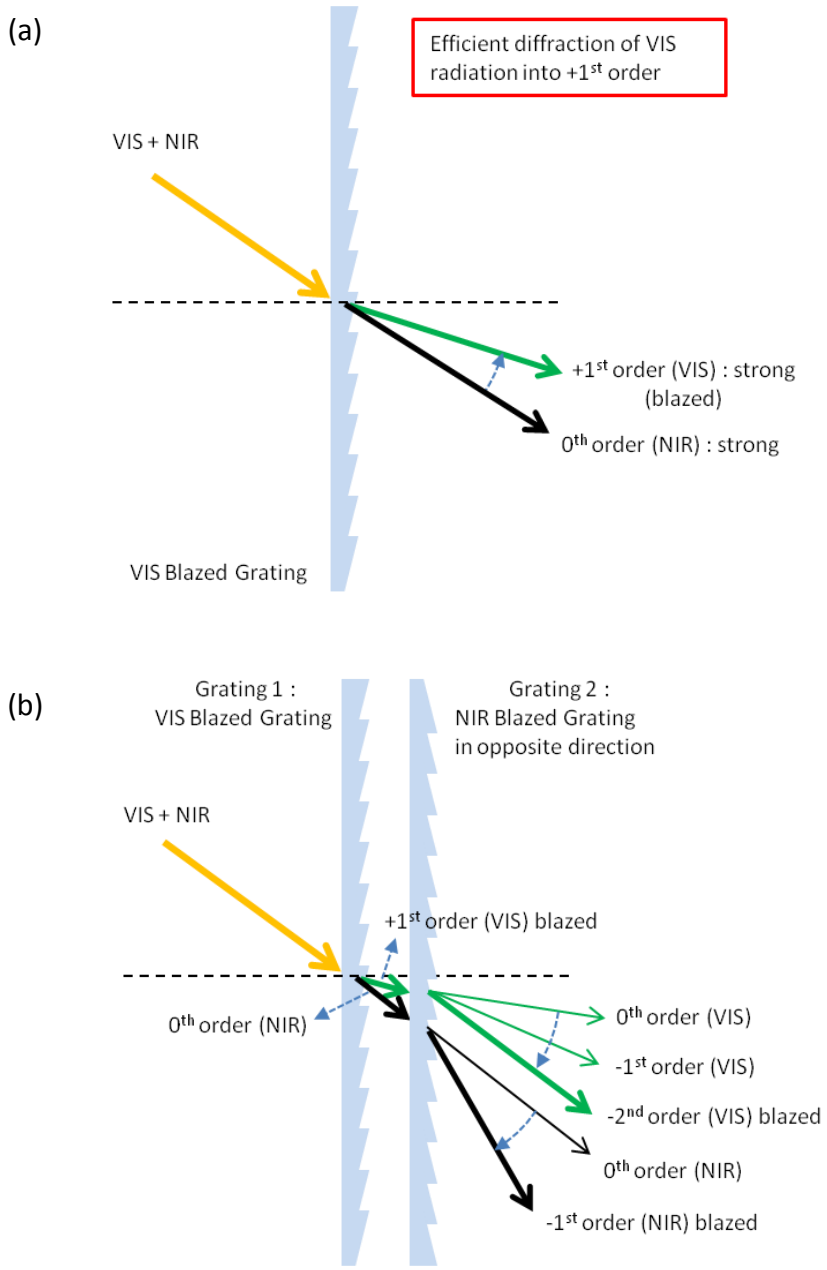

Figure 3.24: Schematic illustration of the concept using two blazed gratings in series for efficient separation of the near-infrared from the visible radiation. (a) Grating 1 is a visible blazed grating (b) Grating 2 is a near-infrared blazed grating placed after Grating 1.

The VIS radiation passes through the second grating as follows. In addition to diffracting the VIS rays into the 0^{th} and $\pm 1^{st}$ orders, the second grating will act also as a blazed grating in the *-2nd order* for the VIS radiation, directing the -2^{nd} order diffracted

VIS rays at an angle 17.46 clockwise from the VIS rays *incident on the second grating*. However, since the first grating had already caused deviation of the VIS rays *counterclockwise* by 17.46 degrees (for the $+1^{st}$ order), the VIS rays emerging from the second grating in the -2^{nd} blazed order are angularly separated by 17.46 degrees from the NIR rays emerging from the second grating in the -1^{st} blazed order, as shown in Figure 3.24 (b).

It is this angular separation between the NIR and the VIS rays that is the key to making the window energy-efficient: it allows us to either accept or reject the NIR radiation (thereby reducing heating or cooling costs), while always accepting the VIS radiation (thereby reducing interior lighting costs). More details of how to exploit the angular separation between the NIR and the VIS rays are described below.

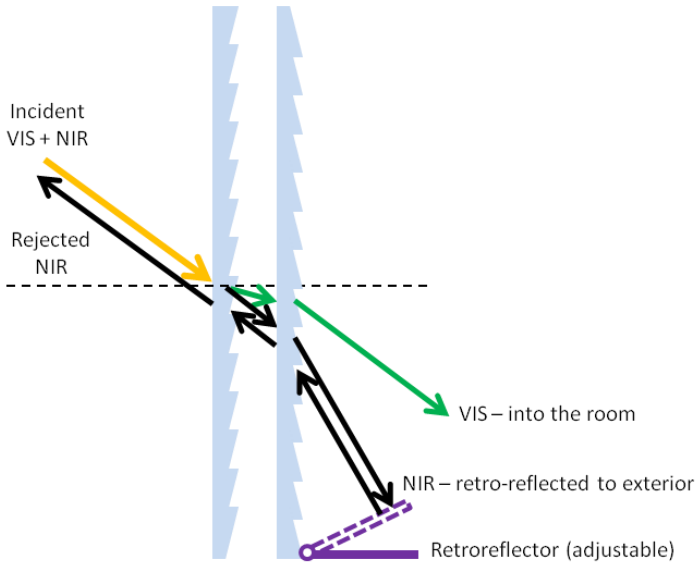

Figure 3.25: Schematic illustration of using adjustable retro-reflector to either reject or accept the angularly separated near-infrared radiation.

Once the NIR diffracted radiation is angularly separated sufficiently from the VIS radiation, a variety of techniques can be employed to either reject of accept the NIR. For example, we can retro-reflect the NIR spectrum to transmit it back to outside the window; this is illustrated in Figure 3.25. A technique to accept the NIR is to absorb the radiation as heat and then utilize the heat as an energy source for other beneficial purposes, such as heating water or air. Many other techniques can be considered for utilizing the NIR radiation. In all cases, the key step for energy efficiency is to create an angular separation between the NIR from the VIS radiation.

It is also desirable to use more than two blazed gratings in series to further enhance the overall energy efficiency of the window system as shown in Figure 3.26. For the VIS band, one blazed grating will be normally sufficient to enable acceptance of most of the VIS spectral component of the sun. However, since the NIR component extends in wavelength from ~ 700 nm to several μm, two or more NIR blazed gratings are desirable to control acceptance or rejection of different segments of the NIR radiation.

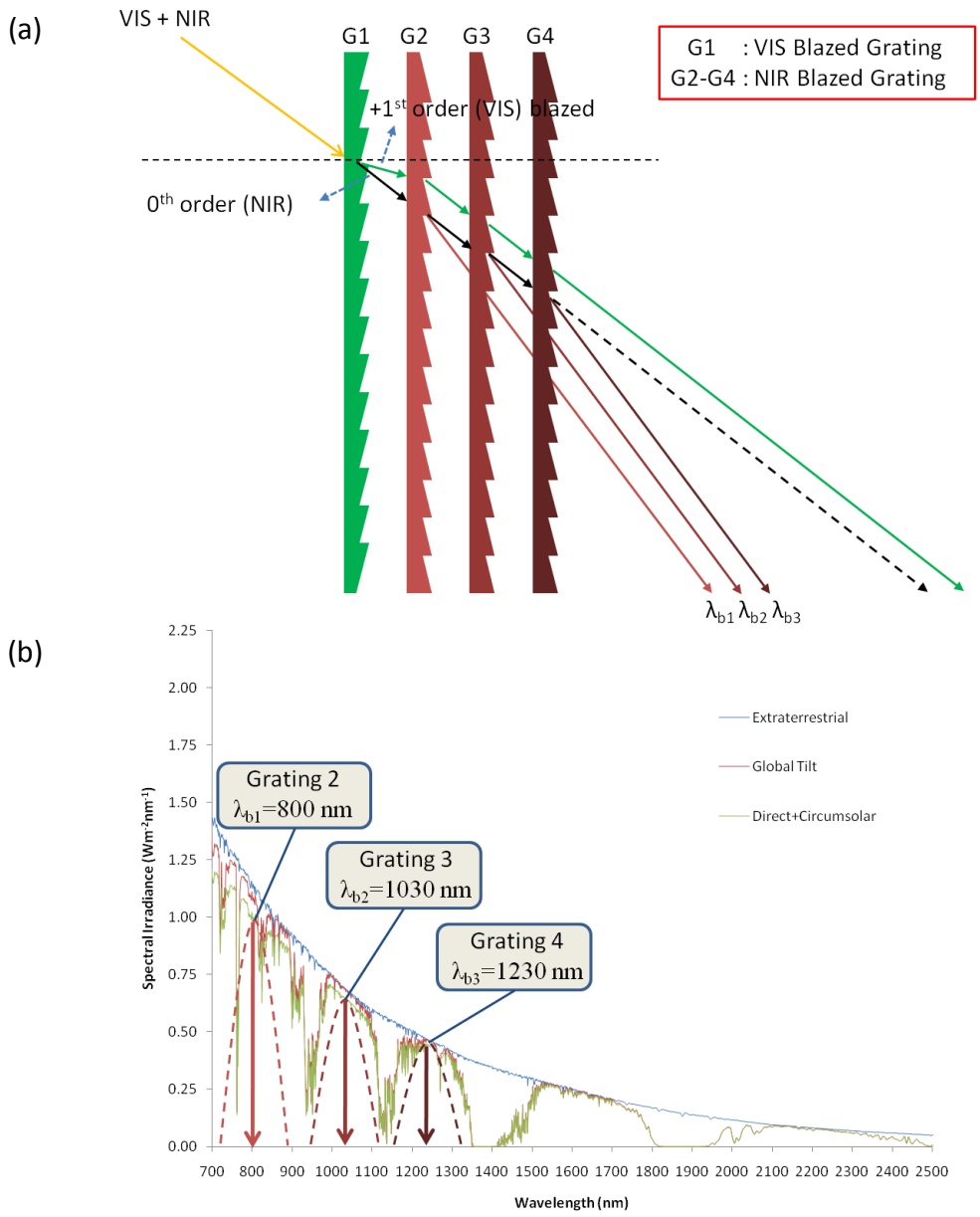

Figure 3.26: (a) Schematic illustration of the concept using multiple blazed gratings in series for highly efficient separation of the near-infrared from the visible radiation. (b) Near-infrared component of the solar spectral irradiance and target wavelengths for the multiple blazed gratings.

3.5.1. Energy-Efficient Window at 30° and 60° Angles of Incidence

Since the angle of incidence of the solar radiation on the window changes throughout the day, we have analyzed the performance of the above window system for

different angles and, as examples, designed the window system parameters for 30° and 60° angles of incidence. Note that both the blazed grating plane and the grating profile need to be dynamically controlled to follow the incident solar radiation. As discussed above, two gratings in series, 600 grooves/mm for VIS and 300 grooves/mm for NIR, achieved a separation angle of 17.46° at normal incidence.

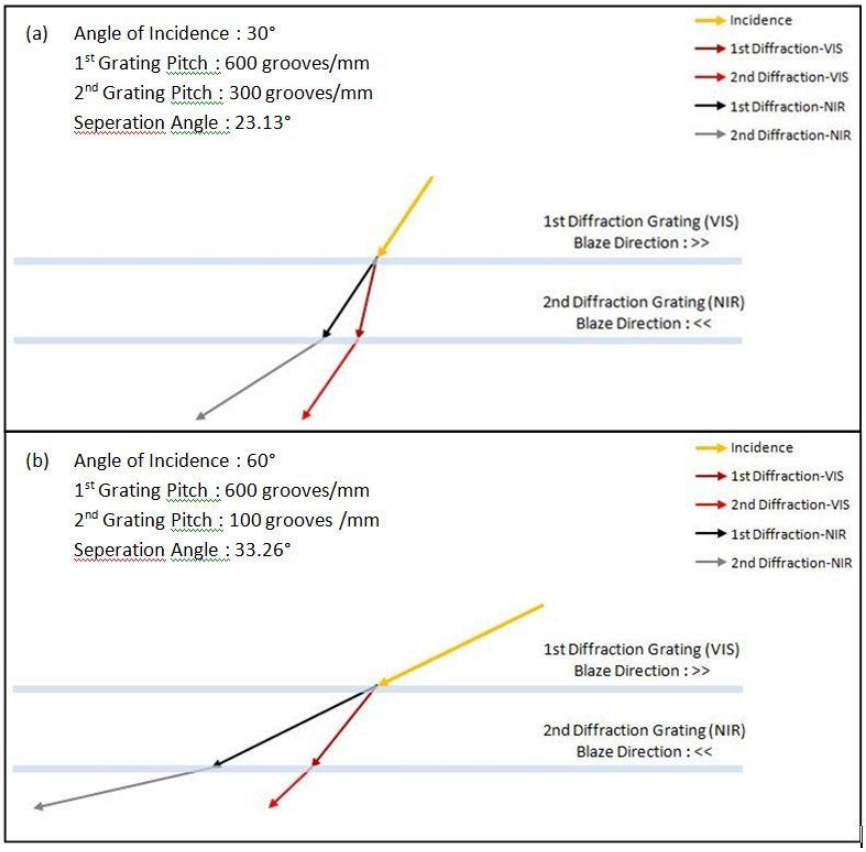

Figure 3.27: Analytical model for calculating the separation angle between 0.5 μm visible wavelength and 1 μm near-infrared wavelength in the case of two blazed gratings in series for (a) 30° incident angle and (b) 60° incident angle.

Figure 3.27 shows a ray diagram of two gratings positioned in series at (a) 30° angle of incidence (Figure 3.27 (a)) and 60° angle of incidence (Figure 3.27 (b)). In the case of 30° angle of incidence, the same grating configuration as that used for normal

incidence performs well; in fact it yields a larger separation angle of 23.13° (between the VIS and NIR). As the angle of incidence increases to 60°, the pitch of the 2nd grating needs to be adjusted to lower spatial frequencies for the NIR diffraction. For example, a 100 grooves/mm pitch for the 2nd diffraction grating results in a separation angle of 33.26°, indicating that the requirement of separation of the VIS and NIR rays becomes easier for larger angles of incidence.

For example, one blazed NIR grating may be designed for the wavelength band 700-900 nm light, a second blazed NIR grating may be designed for the wavelength band 900-1100 nm light, a third grating may be used for 1100-1300 nm light, while a fourth grating may be used for 1500-1700 nm light as shown in Figure 3.26 (b). Each of these NIR blazed gratings works in conjunction with the VIS grating as described above and together they enhance the overall energy efficiency of the window systems.

3.5.2. Experimental Demonstration

We have used physical gratings in series to experimentally demonstrate their ability to separate the solar NIR and VIS spectral regions. We measured the optical performance of a 600 grooves/mm transmission grating (grating pitch of 1.67 μm) with a blaze angle of 28.7° that was designed for the VIS spectral band. We also measured the optical performance of a 300 grooves/mm grating (grating pitch of 3.33 μm) with a blaze angle of 31.7° which was designed for NIR radiation, to demonstrate the efficient separation of the VIS and NIR components. In our measurements, the wavelengths span from 500 nm to 1500 nm by 200 nm increments; thus, our results include 500 nm and

700 nm as the VIS wavelengths and 900 nm, 1100 nm, 1300 nm and 1500 nm as the NIR wavelengths.

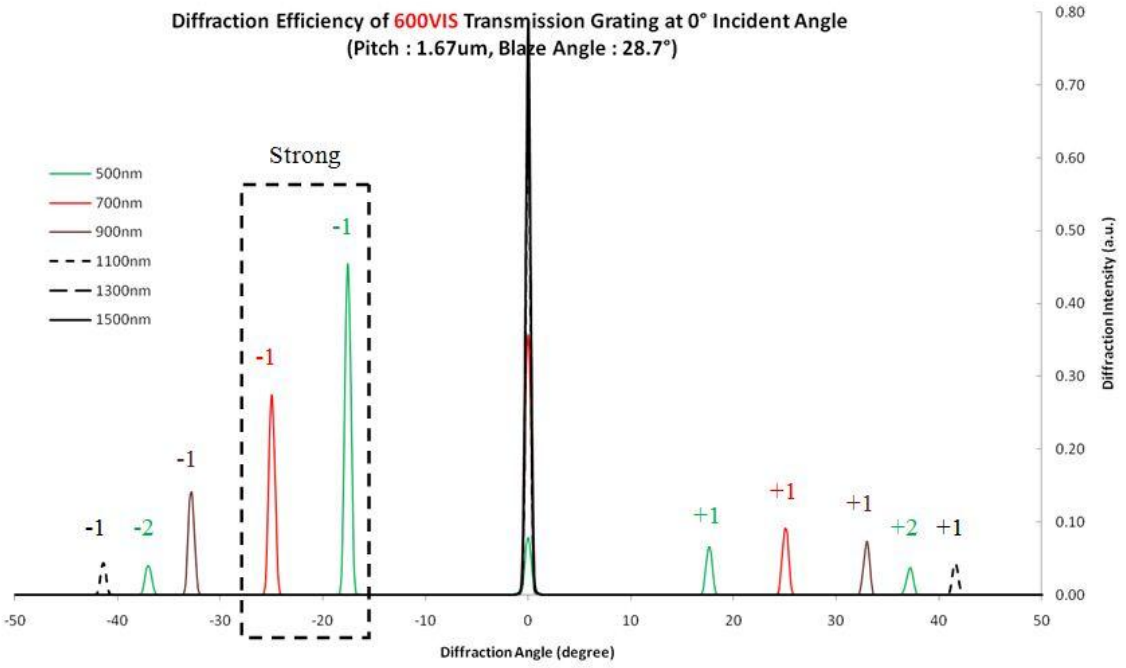

Figure 3.28: Distribution of diffraction peaks as a function of diffraction angle for the 600 grooves/mm (1.67 µm pitch) visible blazed grating shows strong 1st order blazing of the visible wavelengths.

Figure 3.28 illustrates the distribution of the diffracted intensities in different diffraction orders as a function of diffraction angles for several wavelengths selected from VIS and NIR regions for the case of a 600 grooves/mm grating (grating pitch of 1.67 µm) with a blaze angle of 28.7° nominally designed for the VIS band. Note that the -1st order blazing for 500 nm wavelength occurs with the highest efficiency while the 0th order becomes stronger as the wavelength increases into the NIR region. Therefore, as expected, most of the transmitted VIS radiation is directed toward -1st diffraction order while most of the NIR radiation is directed into the 0th diffraction order.

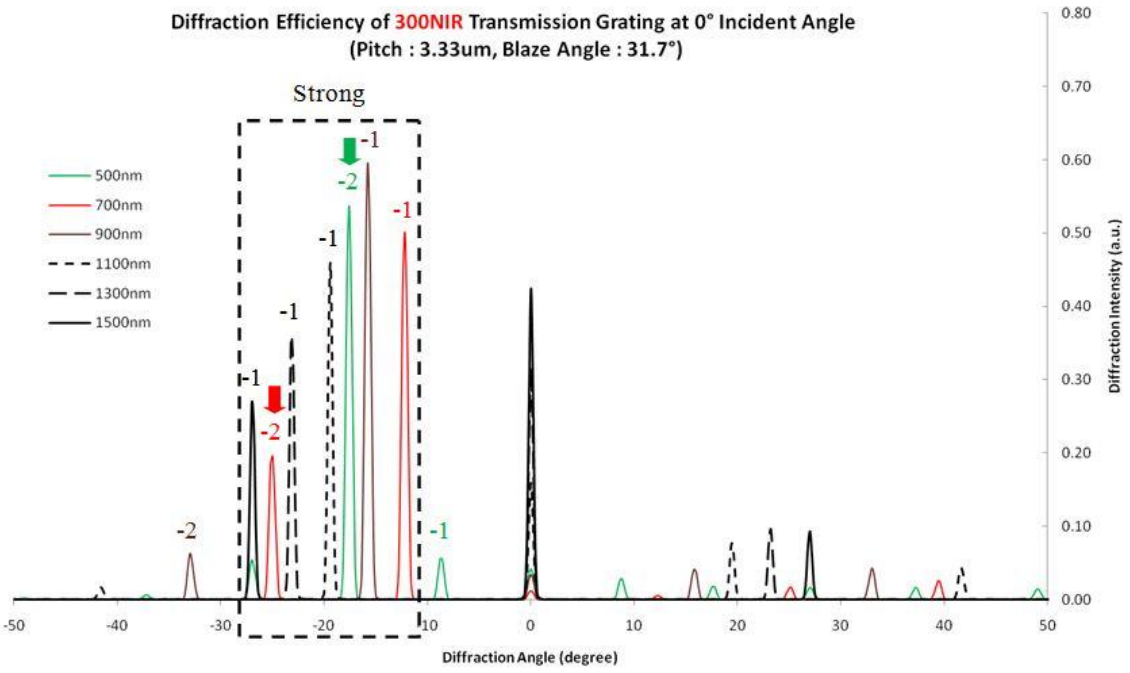

Figure 3.29: Distribution of diffraction peaks as a function of diffraction angle for the 300 grooves/mm (3.33 µm pitch) near-infrared blazed grating shows strong 2nd order blazing of the visible wavelength in addition to strong 1st order blazing of the near-infrared wavelengths.

Figure 3.29 shows the distribution of the diffracted intensities in different diffraction orders as a function of diffraction angles for several wavelengths selected from VIS and NIR spectral bands passing through a 300 grooves/mm grating (grating pitch of 3.33 µm) with a blaze angle of 31.7° and nominally designed for the NIR region. As the figure illustrates, the -1st order blazing occurs with the highest efficiency for 900 nm wavelength and decreases as the wavelength moves away from it but still the blazing for the NIR remains strong. However, among the strong -1st diffraction orders blazing in the NIR region, -2nd diffraction orders blazing for 500 nm wavelength and 700 nm wavelength in the VIS region also appear strong. Therefore, this grating alone is not effective in separating the NIR and VIS wavelengths.

As discussed in section 3.5, the above obstacle is overcome by the use of two blazed diffraction gratings in series where one is blazed for the VIS region and the other is blazed for NIR region, and orienting the grooves of the two diffraction gratings such that their blaze directions are opposite to each other.

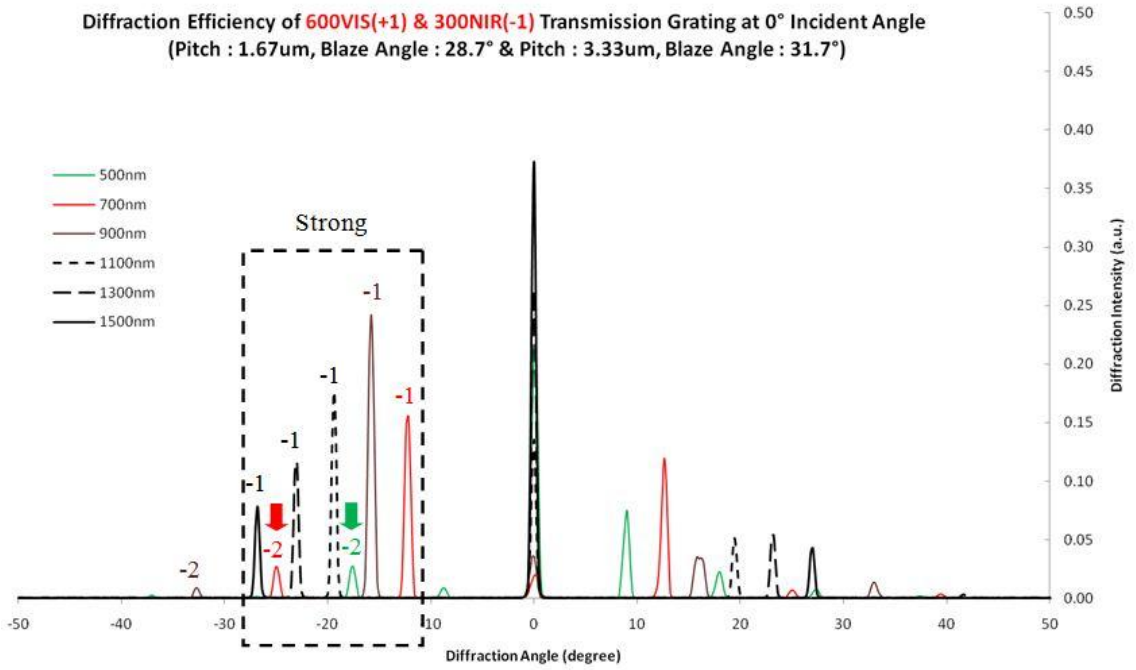

Figure 3.30: Distribution of diffraction peaks as a function of diffraction angle for the 600 grooves/mm (1.67 µm pitch) visible blazed grating plus the 300 grooves/mm (3.33 µm pitch) near-infrared blazed grating shows drastically reduced 2nd order blazing the visible wavelength while retaining strong 1st order blazing of the near-infrared wavelengths.

Figure 3.30 illustrates the distribution of the diffracted intensities in different diffraction orders as a function of diffraction angles for several wavelengths selected from VIS and NIR regions where the two gratings are positioned in series; the first grating has a pitch of 600 grooves/mm (grating pitch of 1.67 µm) and a blaze angle of 28.7° designed for VIS, and the second grating has 300 grooves/mm (grating pitch of 3.33 µm) with a blaze angle of 31.7° and designed for NIR. Here we can observe that

the previously strong -2nd order blazing that occurred for the VIS 500 nm wavelength is now directed to the 0th order because the first grating deflects VIS rays in the opposite direction from the second grating. Therefore, very efficient angular separation between the NIR and the VIS rays is achieved.

3.5.3. Analytical Optical Modeling : Ray Diagram of Multiple Grating System

We have performed detailed optical modeling of the operation of the multiple-grating system using ray tracing algorithms. As an illustration of the benefits of the optical modeling capability, ray diagram of all possible light pathways up to 2nd order diffraction is calculated and generated as shown in Figure 3.31. This simulation allows us to visualize the maximum separation angle between the visible and near-infrared radiation.

The window system is composed of two diffraction gratings where the first grating is designed to blaze the visible radiation and the second grating is designed to blaze the near-infrared radiation in opposite direction. The first grating has a configuration that barely affects the near-infrared, so that the infrared wavelengths are transmitted. In contrast, the visible radiation is blazed or redirected to its +1st order diffraction angle. The second grating has an opposite groove direction so that near-infrared radiation is redirected to its -1st order but in the other direction from the visible radiation. In this case, most of the visible wavelength is transmitted without bending but the -2nd order of visible wavelength that is half of the target near-infrared blaze wavelength is as shown in Figure 3.32.

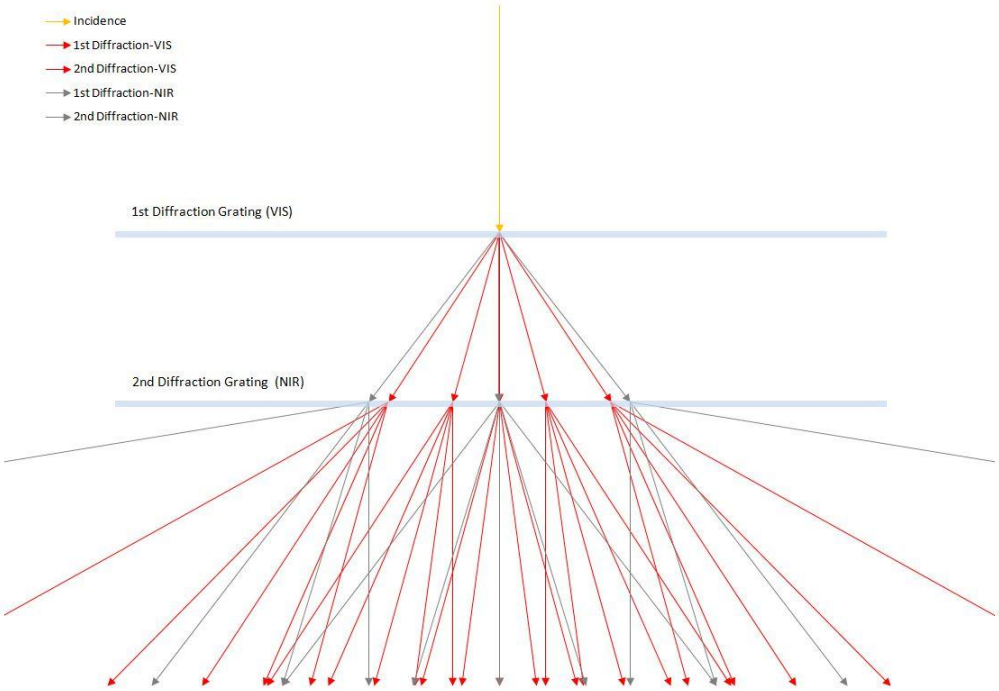

Figure 3.31: Ray diagram of theoretically calculated light pathways that shows up to 2nd order diffraction of the incident visible and near-infrared wavelength for the two blazed gratings in series system.

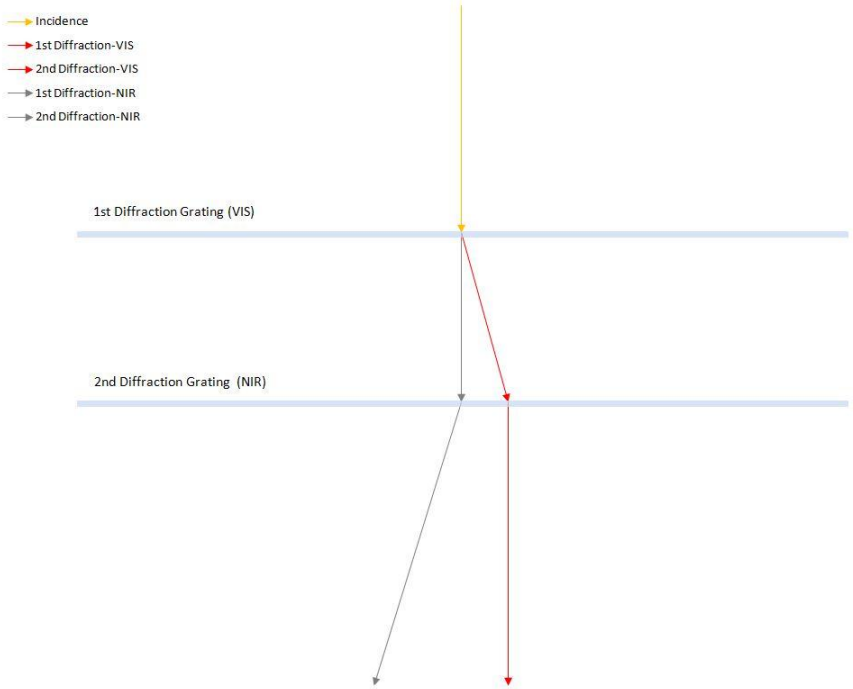

Figure 3.32: Ray diagram of theoretically calculated light pathways that shows only the highest efficient diffraction order of the incident visible and near-infrared wavelength for the two blazed gratings in series system.

For example, if the second near-infrared grating blaze wavelength for 1st order diffraction is 1000 nm, then 2nd order diffraction of the visible 500 nm wavelength is blazed as well. However, because the first grating has already blazed the visible wavelength to the opposite direction, the second grating only redirects the visible wavelengths back to its original incoming pathway.

To summarize, the solar irradiance on this multiple grating window system rejects the near-infrared beam by blazing the near-infrared radiation to a higher angle than the incident angle. Meanwhile, most of the visible wavelengths remains undeflected on its pathway (with some transmitting diffusely), such that the window system does not lose the visible radiation that is useful for interior lighting.

CHAPTER 4

SMART WINDOW BASED ON ELECTRO-OPTIC DIFFRACTIVE STRUCTURES

4.1. Introduction

In addition to demonstrating the properties of blazed gratings for smart window application using physical gratings, we have extended the concept to design a dynamically programmable, 2-dimensional, large-area, energy-efficient device. The major requirements to realize such a device are: angular separation of the near-infrared radiation from the visible radiation of the incident solar irradiation by a specified angle (> 10º); high efficiency of deflection (at least 80%); tracking of the direction of the incident solar rays; and low power consumption.

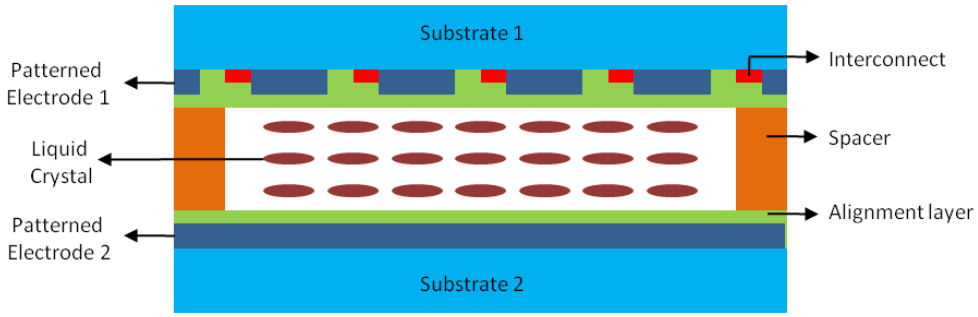

Figure 4.1: Schematic diagram (cross-section) of an electrically controllable pixelated diffraction grating which utilizes liquid crystal as the optoelectronic medium.

To meet our objective of controllable acceptance or rejection of selected spectral regions of the solar radiation, we propose an electrically controllable and configurable

blazed diffraction grating that is realized by individually addressable 2-dimensional pixelated electrodes where an electro-optic material such as a liquid crystal is sandwiched between two sets of electrodes, as shown in Figure 4.1.

By applying spatially periodic voltages ($V_1 < V_2 < V_3 < V_4$) to adjacent electrodes while keeping a second set of electrodes constant, an electric field is applied which changes the director orientation (optical axis) of the liquid crystals. The applied spatially periodic electric field across the liquid crystal layer induces a sawtooth-shaped refractive index variation in the liquid crystal layer that steers an incident optical beam in a fashion analogous to that of a surface-relief blazed diffraction grating as shown in Figure 4.2,

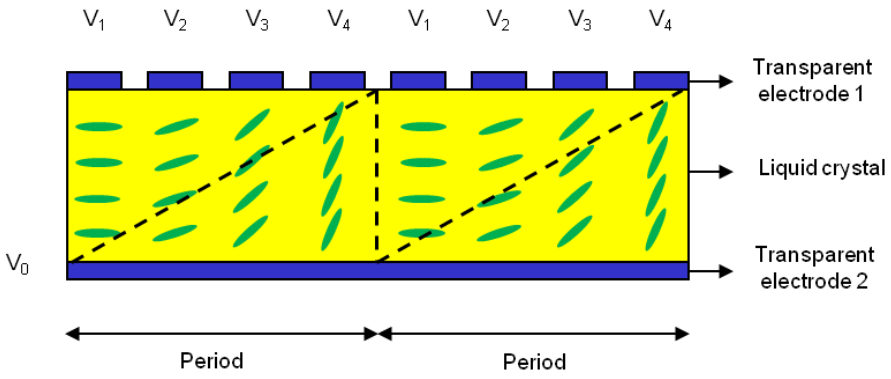

Figure 4.2: Schematic diagram (cross-section) of the change in effective refractive index (dotted line) of the liquid crystal layer by applying spatially periodic voltage.

The electric fields can be optimized for a specific spectral band to adjust the phase retardation, such that selective efficient beam separation is achieved by blazed diffraction. The pixelated grid structure is electronically programmed to create effective groove configurations in various desirable orientations that enable the window to function in the required mode. The control signals to the groups of pixels are provided

through thin-film electrodes of a transparent conductive material such as indium tin oxide (ITO). A passive-matrix driving method addresses the pixels by dividing the control signals into columns and rows as shown in Figure 4.3. By using row and column addressing, we can modulate individual pixels in the smart window device. The phase of the incident light is altered by the voltage-controlled refractive index modulation. The desired linear phase shift is approximated by a series of constant phase steps. When there is no voltage applied to the cell, the liquid crystal molecules are oriented parallel to the plates of the cell. When a voltage is applied to the cell, the liquid crystal molecules rotate. The rotation of the liquid crystal molecules causes the change in the effective index of refraction, resulting in the desired optical path length change and relative phase shift.

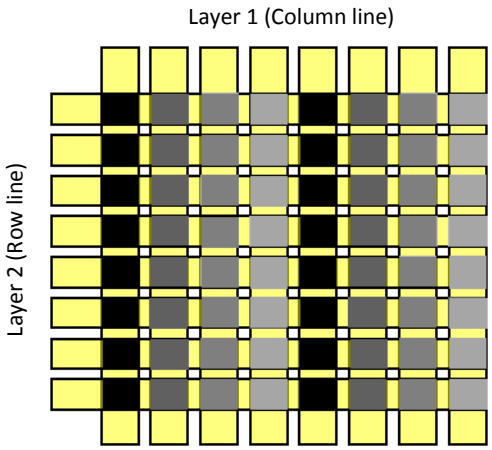

Figure 4.3: Schematic illustration of a passive-matrix driving method where two layers of electrode lines are running perpendicular to each other with the liquid crystal layer in-between

4.2. Binary Approximation to Triangular Groove Profile

The fabrication process for a physical blazed grating utilizing photolithography and etching technology was described in Chapter 3. As compared to a physical blazed

grating, an electro-optic blazed grating is generated by creating a step profile of the effective index of refraction in the liquid crystal layer by applying an electric field. Here, the number of steps is determined by the number of electrodes used for the grating pitch.

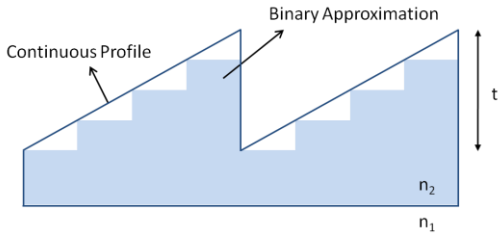

Figure 4.4: Binary step profile approximation to triangular groove profile that is ideal for high efficiency blazed diffraction gratings.

The diffraction efficiency of this stepped profile as shown in Figure 4.4 (binary approximation to a continuous triangular profile) can be calculated by expanding its amplitude transmittance (periodic function) into a Fourier Series. The calculation shows that the diffraction efficiency of the mth diffraction order is [53],

$$\eta_m = sinc^2\left(\frac{m}{2^N}\right) \times \frac{sinc^2\left(m-\frac{\delta}{2\pi}\right)}{sinc^2\left(\frac{m-\frac{\delta}{2\pi}}{2^N}\right)} \tag{4.1}$$

where N is an integer for 2^N number of steps and δ is the maximum phase difference of the continuous triangular profile which is given by

$$\delta = 2\pi \frac{t(n_2-n_1)}{\lambda} \tag{4.2}$$

where t is the height (thickness) of the continuous triangular profile, n_2 is the index of refraction of the grating material, n_1 is the index of refraction of the surrounding medium (typically air), and λ is the wavelength in the surrounding medium.

Because we are interested in the case for a blazed diffraction grating where the phase difference (δ) is 2π, substitution in Equation 4.1 yields,

$$\eta_m = sinc^2\left(\frac{m}{2^N}\right)\frac{sinc^2(m-1)}{sinc^2\left(\frac{m-1}{2^N}\right)}. \tag{4.3}$$

Here, the second factor of Equation 4.3 becomes zero except when

$$m - 1 = n2^N \tag{4.4}$$

where *n* is a non-zero integer, and the diffraction efficiency can be expressed as

$$\eta_{(n2^N+1)} = sinc^2\left(n + \frac{1}{2^N}\right). \tag{4.5}$$

Therefore, the 1st order (n=0) diffraction efficiency of a 2^N step-approximated grating profile is,

$$\eta_{m=1} = \left[\frac{sin\frac{\pi}{2^N}}{\frac{\pi}{2^N}}\right]^2. \tag{4.6}$$

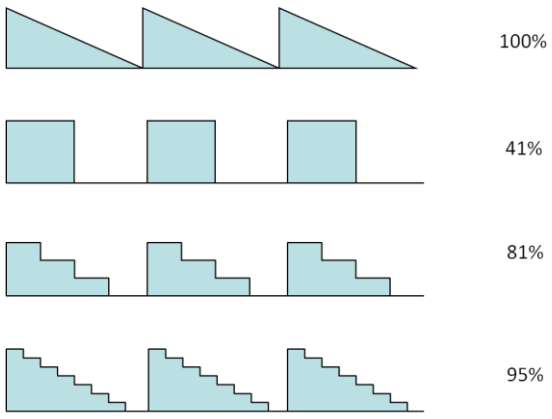

Figure 4.5: Theoretical 1st order diffraction efficiency by binary step approximation.

Figure 4.5 shows the theoretical 1st order diffraction efficiency for 2, 4, and 8 step approximations compared to the continuous triangular groove profile which has 100% efficiency. The first order blazing efficiency increases when a larger number of steps is used to approximate the ideal triangular profile. However, as the number of steps used increases for a given step size (i.e. the electrode pixel size in our device structure), the grating pitch also increases, which reduces the angular separation between the visible and near-infrared radiation, which is not desired. It is also not desired to reduce the electrode pixel size to increase the number of steps for a given grating pitch to achieve higher diffraction efficiency, because of the increase in complexity for manufacturing smaller feature size and driving electronics. Therefore, as a compromise, we selected a 4-step profile as the ideal number of steps for our window application.

4.3. Electro-Optic Materials – Liquid Crystals

A key advantage that liquid crystals have over other electro-optic media is that they exhibit a large refractive index modulation ($n > 0.2$) with relatively small applied voltages (< 10 V) [54-56]. This large change in the refractive index allows for large phase changes with thin and low-voltage liquid crystal devices.

Liquid crystals have very complex structures which are often comprised of a side chain, aromatic rings, linkage groups, and a terminal group [57-59]. The chemical stability of liquid crystals is strongly dependent on the central linkage group. All the

physical and optical properties of LCs are governed by the properties of these constituent groups and how they are chemically synthesized together.

Many physical properties, such as dielectric constants, elastic constants, viscosities, absorption spectra, transition temperatures, anisotropies, and optical nonlinearities are also dependent on the molecular constituents and how they are engineered. Since liquid crystals have complex structures, it is possible to manipulate the molecular architecture and change the physical properties of the liquid crystal to some extent [60-64].

The liquid crystal candidate used for the smart window application is E7 from Merck. Consisting of a mixture of four liquid crystalline molecules, E7 exhibits a high birefringence and optical transmittance in the visible and near-infrared spectral range [65]. The optical properties, birefringence, and viscosities are very different from those of the individual constituents. Creating engineered mixtures is an art guided by complex techniques that is not within the scope of our research; however, our supplier, Merck, is able to modify the physical properties of E7 if it does not fulfill our needs.

4.3.1. Liquid Crystal Light Modulation

A wide variety of liquid crystal materials are used in light modulation applications. For example, twisted nematic liquid crystals are commonly used in flat-panel displays for intensity modulation [66-69]. The liquid crystal cell is placed between two polarizers. In the off state, the incident light becomes linearly polarized by the first polarizer and follows the twisted nematic liquid crystal pathways and transmits through the second polarizer; therefore, no absorption occurs. However, when a voltage

is applied, the liquid crystals begin to align along the applied electric field direction, thus reducing the alignment between the incident polarization direction and the second polarizer, thereby decreasing the transmitted light. The flat-panel display industry has investigated and developed liquid crystal light modulation technologies to an extremely high level of maturity and reliability.

Electrically controllable nematic liquid crystals have a high optical anisotropy and high transmission efficiency [65], and can also be used as phase modulation devices; they are widely used in applications such as non-mechanical beam steering [70-76] and tunable focusing [77-80]. Liquid crystals with high birefringence provide large changes to the refractive index with increase in the applied electric field. These changes are precisely controlled to adjust the phase retardation; thereby wide-angle beam deflection is achieved by diffraction.

4.3.2. Effects of Electric Field on Liquid Crystal

The liquid crystal deformation inside the cell depends on the applied electric fields which regulate the orientation of the liquid crystal optical axis, also known as director, with respect to the electrode grating. The reorientation of the liquid crystal molecules produces the phase modulation. The Frederick's transition formula indicates that the reorientation starts when the voltage exceeds the threshold voltage. The threshold voltage for the Frederick's transition of the planar aligned liquid crystal cell is given as [58, 59]

$$V_{th} = \pi \frac{p}{d} \sqrt{\frac{K}{\Delta\varepsilon \bullet \varepsilon_0}} \tag{4.7}$$

where $\Delta\varepsilon$ is the dielectric anisotropy, p the electrode distance, d the cell thickness, and K is an elastic constant. To achieve phase modulation, the electrode voltage has to be higher than the threshold voltage, which is 1.1 V for E7 ($\Delta\varepsilon$ = 17.3, K = 17.9 pN) when the electrode period and cell thickness are each 5 μm. This comfortably meets the requirements for low voltage operation and low power consumption.

4.3.3. Advantages of Electro-Optic over Physical Blazed Diffraction Gratings

In Chapter 3, we observed from the diffraction intensity curves that a physical blazed diffraction grating that blazes the near-infrared wavelengths to its 1st order diffraction angle also blazes visible wavelength, which is half of the blazed near-infrared wavelength, to the 2nd order diffraction angle. This is because the diffraction grating equation (Equation 3.13) dictates that if the product of the diffraction order (m) and wavelength (λ) is the same for a given diffraction grating (d), then the diffraction angle (θ_d) is the same. Thus the 1st order (m=1) diffraction of λ_1, and 2nd order (m=2) diffraction of λ_2 will both diffract to the same direction (diffraction angle) if λ_2 is half of λ_1.

The differences between a physical grating and an electro-optic grating can be explained by discussion of optical phase delay (OPD). For a commonly employed "reflection-type physical grating" as illustrated in Figure 4.6 (a), the OPD caused by successive grooves is $2d\sin\theta_b$. If this value is a multiple (m) of the target wavelength (λ), blazing occurs. When the groove depth is large enough so that multiple diffraction orders are possible, both 1st order (m=1) λ_1, and 2nd order (m=2) λ_2, whose wavelength is half of λ_1, will be blazed.

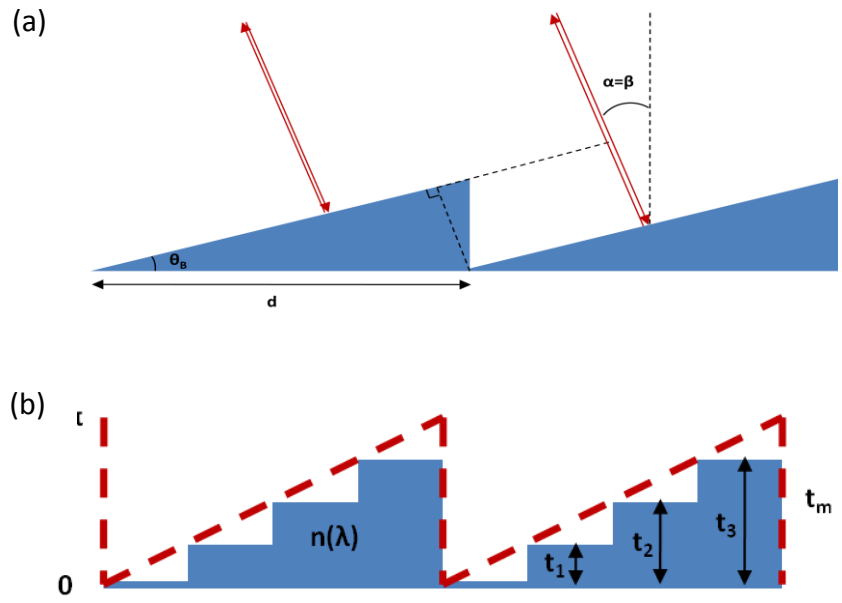

Figure 4.6: Optical phase delay (OPD) for (a) Reflective blazed grating (b) Transmissive blazed grating.

This is also the case for a "transmission-type physical grating" in which the OPD caused by successive groove is $\frac{2\pi}{\lambda} t_m \Delta n(\lambda)$ for normal angle of incidence (Figure 4.6 (b)).

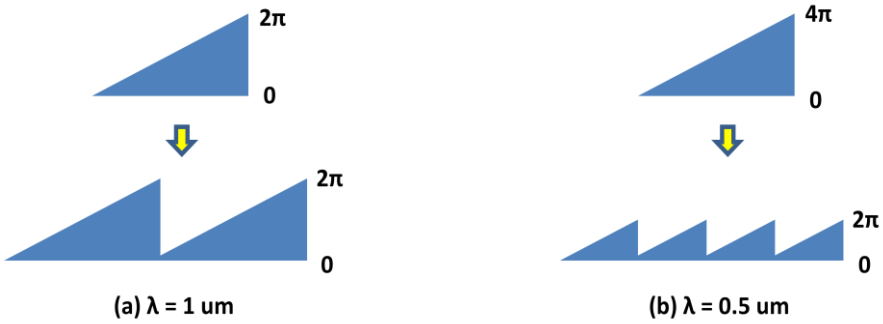

Figure 4.7: Optical phase delay (OPD) in physical blazed grating. (a) 2π OPD (continuous) for 1 μm wavelength. (b) 4π OPD (continuous) for 0.5 μm wavelength is effectively half pitch 2π OPD (continuous).

Figure 4.7 illustrates a physical diffraction grating that has a groove depth of 2π OPD for 1 μm wavelength (Figure 4.7 (a)) will have 4π OPD for 0.5 μm wavelength

(Figure 4.7 (b)). In this example, the effective groove pitch for the 0.5 μm wavelength is half of the effective groove pitch for 1 μm wavelength with a continuous blazing groove profile. Therefore a physical diffraction grating that will blaze the 1 μm wavelength will also blaze the 0.5 μm wavelength to the same angle with equal efficiency, which is not desired for efficient separation of the near-infrared and the visible radiation. In Chapter 3, we eliminated this unwanted blazing of visible radiation by placing two or more physical gratings in series, each intended for different wavelengths.

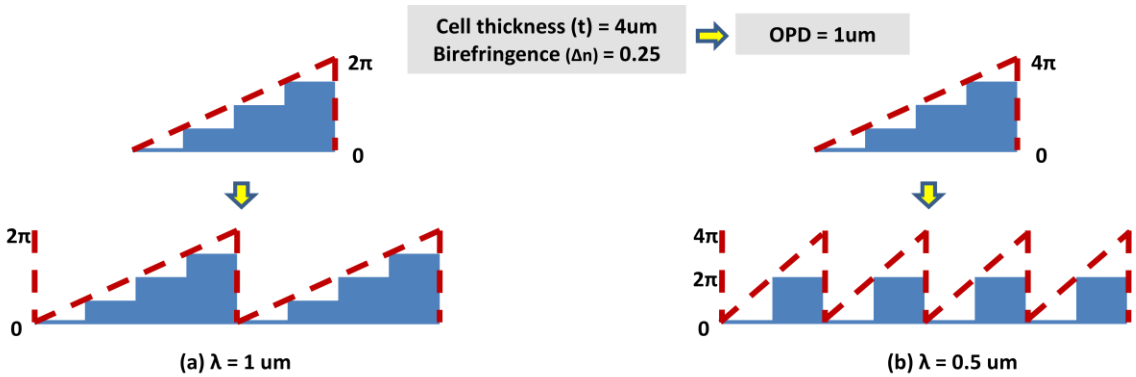

Figure 4.8: Optical phase delay (OPD) in eletro-optic blazed grating. (a) 2π OPD (4-step) for 1 μm wavelength. (b) 4π ODP (4-step) for 0.5 μm wavelength is effective 2π OPD (2-step).

On the other hand, the "transmission-type electro-optic blazed grating" has a step groove profile where the diffraction efficiency is highly dependent on the number of steps, as discussed in the next section. Therefore, as illustrated in Figure 4.8, the effective groove pitch for the 0.5μm wavelength (Figure 4.8 (b)) is still half of the grating pitch compared to the 1 μm wavelength (Figure 4.8 (a)) but the diffraction efficiency is reduced from 81% (for 4-step) to 41% (for 2-step). This is favorable because the unwanted visible radiation, which was reduced by placing additional gratings in the case of physical diffraction grating, is inherently reduced in the case of

the electro-optic diffraction grating. We also carried out detailed optical modeling (Section 4.4.1) and the results agree well with this assertion.

4.4. Optical Modeling and Simulation

4.4.1. Diffraction Pattern Based on Huygen's Principle

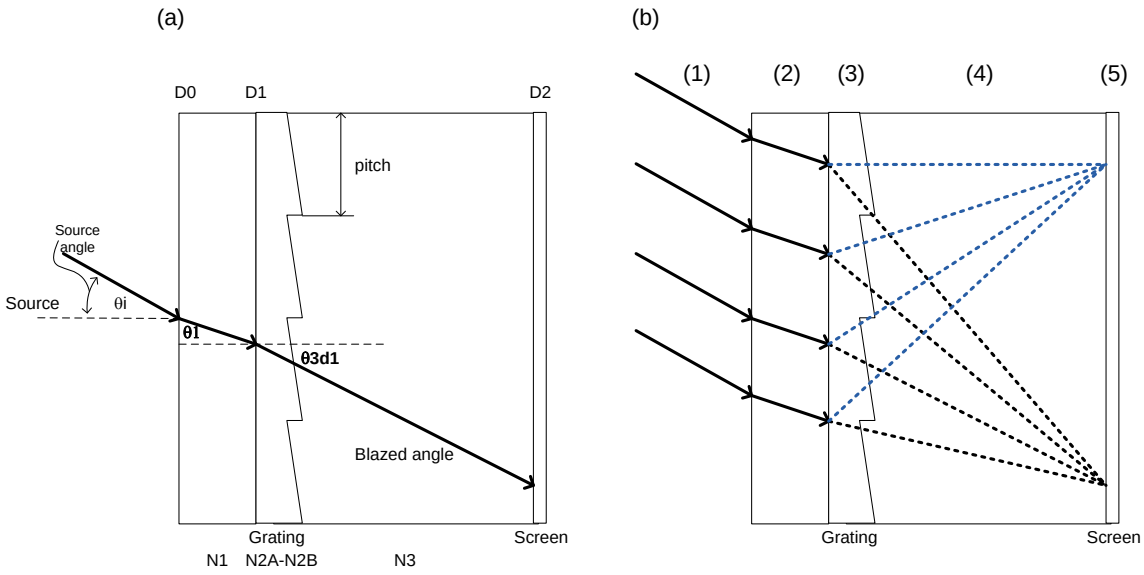

Figure 4.9: (a) Diagram showing simulation setup. (b) Diagram showing beam propagation through simulation.

We have developed a MATLAB simulation to estimate the beam intensity profile of a blazed grating with a saw-tooth profile. Parameters such as the blazed grating profile (pitch, and index of refraction) and the incident beam properties (incident beam size, incident angle, and wavelength) can be changed in the simulation (Figure 4.9 (a)). The output of the simulation shows the relative beam intensity profile after the beam has propagated through the grating. The simulation estimates the beam profile by

discretizing the input, and calculating the individual optical path lengths as the beam propagates through the grating. First, the beam is set at an incident angle θ_i , as shown in Figure 4.9 (b.1). The beam then propagates through a medium with index of refraction n1 (Figure 4.9 (b.2)), and then passes through the blazed grating (Figure 4.9 (b.3)). To mimic the properties of the electro-optic blazed grating, the grating material has an index refraction of n2a to n2b. After the beam passes through the grating, secondary wavelets are generated, as governed by Huygen's Principle. The simulation approximates secondary wavelets generated by the blazed grating by propagating a secondary set of beams, each with a unique angle (Figure 4.9 (b.4)). Lastly, the secondary wavelets reach the screen, which is placed a distance D2 away from the source (Figure 4.9 (b.5)). The optical path lengths of the incident beams are summed at each discrete point on the screen. Those points where the optical path lengths are out of phase will destructively interfere, while other regions where the optical path lengths are in phase will constructively interfere.

The output of the MATLAB simulation is used to compare the blaze angle and blaze efficiency with analytical calculations. For example, various wavelengths of light from 500 nm to 1500 nm are simulated through a 4-step blazed grating with index of refraction of 1.5 to 1.65, and a pitch of 10 μm and 30 μm with 0 degree incident angle (Figure 4.10). As predicted, the blazed grating acts like a binary grating to the 500 nm light, and it is most efficient at wavelengths near 1000 nm. When the angle of the incident beam is changed to 20 degrees (Figure 4.11), the blaze angle follows that which is predicted by analytical calculations. Results are summarized in Table 4.1.

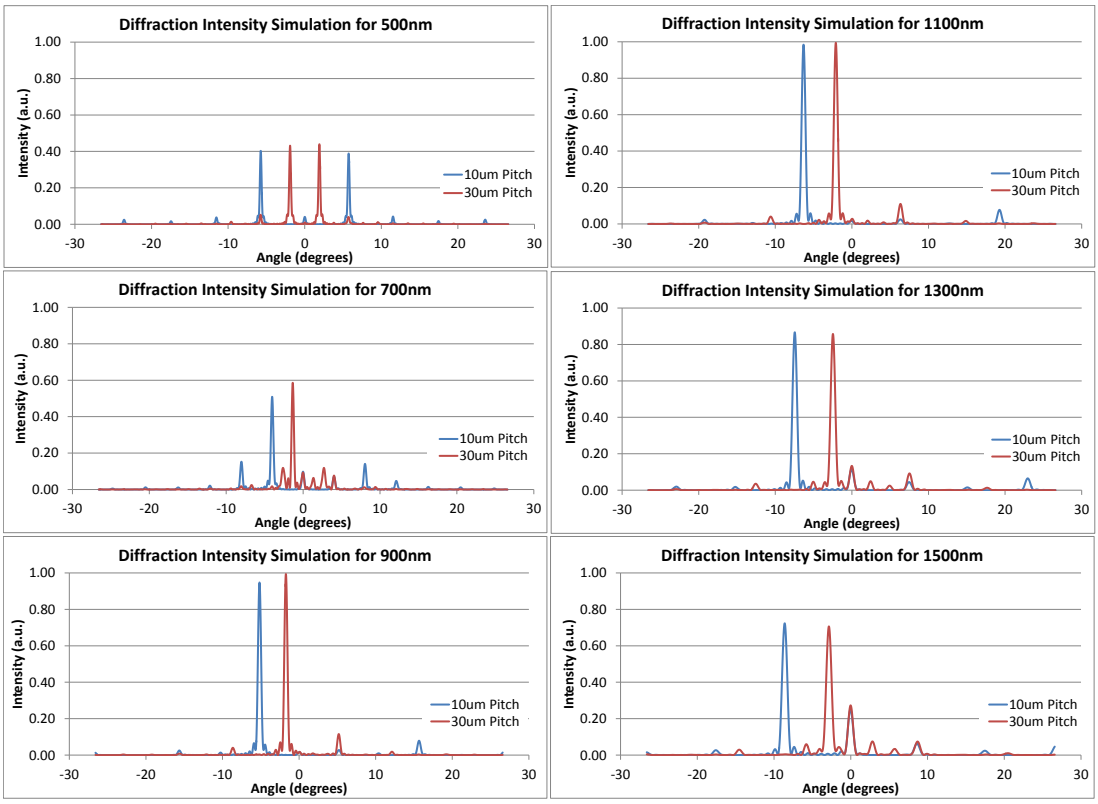

Figure 4.10: Diffraction intensity simulation for 0° angle of incidence.

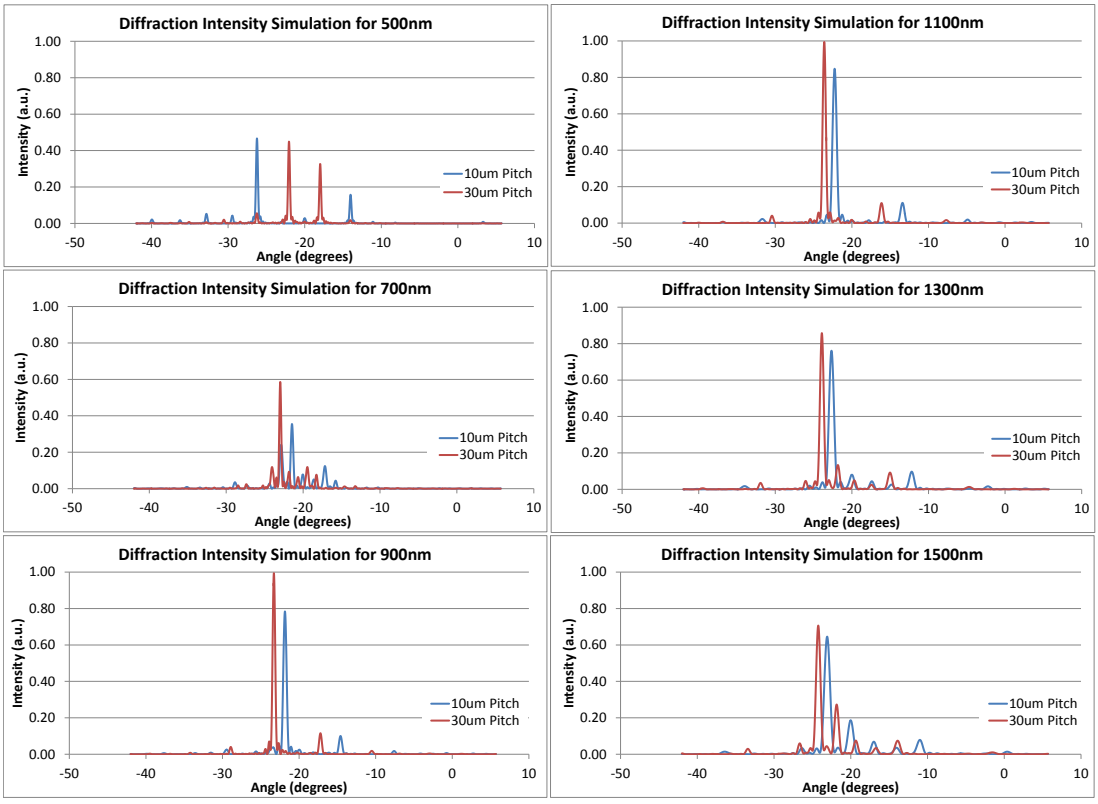

Figure 4.11: Diffraction intensity simulation for 20° angle of incidence.

(a)

Wavelength	Pitch =30 µm, Simulation	Pitch=30 µm, Analytical	Pitch=10 µm, Simulation	Pitch=10 µm, Analytical
500 nm	-1.909	-1.910 (-2nd)	-5.739	-5.739 (-2nd)
700 nm	-1.348	-1.337	-4.025	-4.014
900 nm	-1.72	-1.719	-5.165	-5.164
1100 nm	-2.098	-2.101	-6.312	-6.315
1300 nm	-2.47	-2.484	-7.409	-7.470
1500 nm	-2.848	-2.866	-8.601	-8.627

(b)

Wavelength	Pitch=30 µm, Simulation	Pitch=30 µm, Analytical	Pitch=10 µm, Simulation	Pitch = 10 µm, Analytical
500 nm	-22.0531	-22.046 (-2nd)	-26.23	-26.233 (-2nd)
700 nm	-21.4445	-21.429	-24.3445	-24.332
900 nm	-21.8508	-21.840	-25.6028	-25.596
1100 nm	-22.2548	-22.252	-26.8716	-26.873
1300 nm	-22.6663	-22.666	-28.1573	-28.166
1500 nm	-23.0753	-23.080	-29.4649	-29.473

Table 4.1: (a) Diffraction peak angles obtained from simulation results are compared with theoretically calculated diffraction angles. (a) 0° incident angle. (b) 20° incident angle.

4.4.2. Optical Simulation of Proposed Window System

A more detailed analysis and modeling of the proposed smart window system in the form of an electro-optic blazed phase grating is discussed by incorporating the typical optical properties and the corresponding light modulation characteristics of liquid crystal in the presence of an electric voltage distributed across the surface of the crystal.

As described in section 4.1, our blazed grating smart window system would be realized by addressing the pixels by passive-matrix driving method in row and column signals. This is expected to introduce birefringence and also localized index variations based on the voltage regulations across the surface. Optical refraction / diffraction phenomenon is systematically analyzed using optical design ray tracing software by creating such blazed element structures and providing necessary software add-ons to trace these structures.

4.4.2.1 Birefringence and Graded Index in Liquid Crystals

Many liquid crystals are birefringent and the electro-optic effect in a nematic liquid crystal modulates its refractive index for extraordinary light in the presence of a driving voltage. The selected liquid crystal E7 (Merck) has refractive-indices at 633 nm wavelength for extraordinary and ordinary light as 1.737 and 1.5185, respectively [75]. The refractive index decreases continuously as the driving voltage increases. As the voltage varies from 0V to a large value such as 5V, a birefringence of 0.2 is introduced, with refractive index dropping from n_e to n_o with a threshold voltage around 1V, as shown in Figure 4.12.

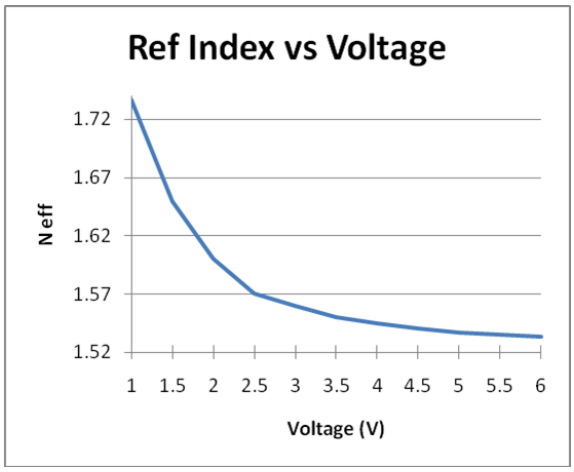

Figure 4.12: Liquid crystal refractive index variation with increasing voltage.

We can obtain the necessary graded index distribution to produce a 4-step phased blazed element, as shown in Figure 4.13, distributing such voltage variation horizontally along the first 4 x 4 pixels in the passive matrix. The X-axis has been deliberately normalized over the width/aperture of the blazed element. Normalization over the width helps in automatically making the gradients steeper for small blazed elements and

shallower for broad elements, causing the refractive/diffractive properties to be taken into account automatically by the software.

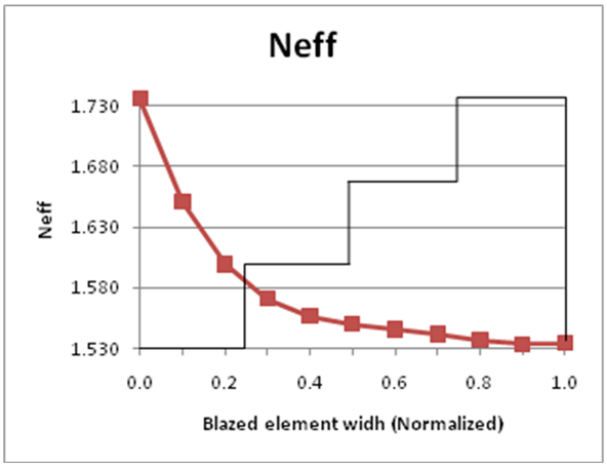

Figure 4.13: Liquid crystal refractive index variation across blazed element width for 4 x 4 passive matrix distribution.

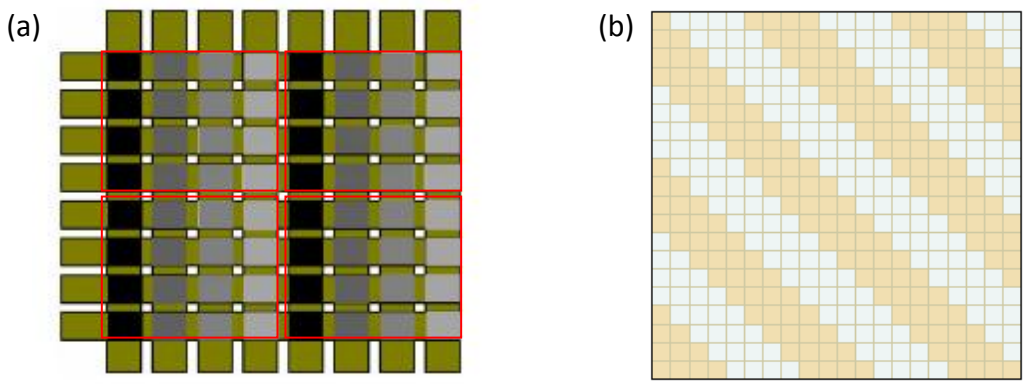

Figure 4.14: Array of blazed elements each with a 4 x 4 passive matrix pixels with innumerable programming patterns and light modulations. Each red square matrix of 4 x 4 elements in (a) corresponds to a square blazed element pixel in (b).

Having defined such a 4 x 4 matrix as one blazed element, the Smart Window structure may be represented as an array of these blazed elements that may be

programmed in numerous possible ways to obtain several combinations of phase profiles for desired light modulations in transmission (Figure 4.14).

In the following sections, a method using optical design software such as ZEMAX is briefly described to model the optical properties of the smart window with an array structure in place [81].

4.4.2.2 Optical Modeling of Liquid Crystal Blazed Grating Surface [81]

A computational model is developed to design the smart window to function like a programmable window and provide necessary combinations of light modulations for different seasons. The optical thickness of a nematic liquid crystal can be controlled to consist of a 2-D array of equally spaced liquid crystal phase shifters/directors that orient progressively with increased voltage provided by the striped electrodes on top of the liquid crystal [76]. Thus each set of 4 directors along a column of 4 x 4 matrix in Figure 4.14 sees the same voltage and the 4 directors along each row see a graded voltage pattern causing graded index profiles shown in Figures 4.12 and Figure 4.13.

The liquid crystal layer is continuous and the multitude of conducting striped electrodes is patterned to create an array of 4 x 4 matrices equally spaced to form a programmable blazed diffraction grating that steers the incoming light beams in preferred -1 grating order. The spacing between the blazed elements decides the angle of diffraction with increased angles for smaller stripes and element spaces.

The next step is to construct such a blazed optical surface in the optical design software and attribute to it optical properties such as shape, refractive index and thickness, and also optical properties of the surrounding media. We have assumed that

the blazed element formed by a 4 x 4 passive matrix pixels is a square of 4 conducting stripes in the X- and Y- directions. The voltage distribution is made to vary in the X-direction for each matrix element while the voltage along the Y-direction remains constant for each matrix element. This makes the molecule directors reorient their axis as shown in Figure 4.15 causing effective refractive index to vary along the X-axis as in Figure 4.13 for LC E7. In order to enter the refractive index profile in ZEMAX we fitted the data in Figure 4.13 to a polynomial of 4th order in X for least residual error.

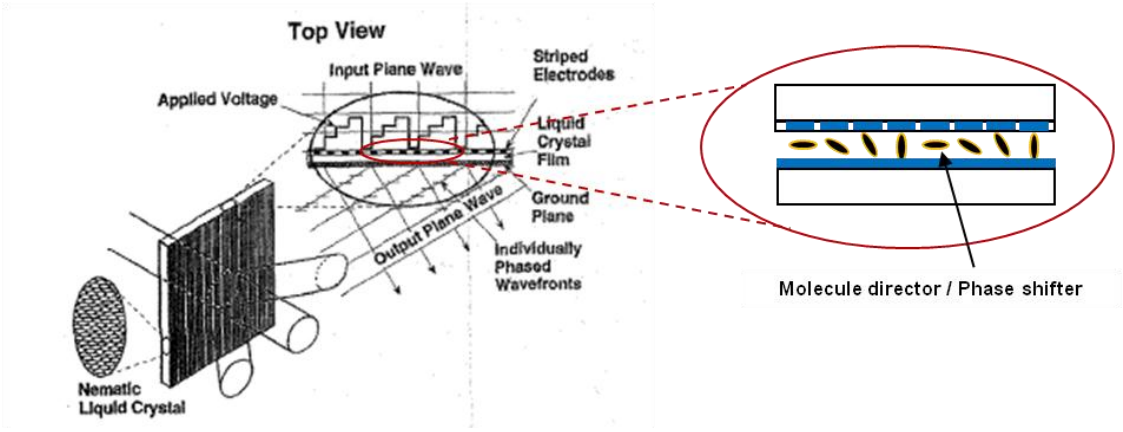

Figure 4.15: View of 2-D beam steering device [76] and a conceptual imposed phase shift by progressively oriented liquid crystal molecules with graded voltage on striped electrodes.

We used MathSoft's AXUM software to fit the data and obtained the polynomial coefficients. We represent the variation of effective index with voltage and/or position along X-axis in blazed element as follows:

$$n = N_0 + N_{x1} \cdot \frac{x}{A_p} + N_{x2} \cdot \left(\frac{x}{A_p}\right)^2 + N_{x3} \cdot \left(\frac{x}{A_p}\right)^3 + N_{x4} \cdot \left(\frac{x}{A_p}\right)^4 \qquad (4.8)$$

where N_0, N_{x1}, N_{x2}, N_{x3}, and N_{x4} are the index profile coefficients and the positional coordinates are normalized over the aperture A_p of the blazed element.

For Merck E7 liquid crystal, these coefficients become

$$N_0 = 1.736;\ N_{x1} = -1.065;\ N_{x2} = 2.342;\ N_{x3} = -2.347;\ N_{x4} = 8.68E\text{-}01 \qquad (4.9)$$

Using this index distribution, a blazed element is constructed in ZEMAX as a non-sequential object. The library of optical objects in ZEMAX does not contain blazed elements so we have constructed one that is traceable and allows all diagnostic functions of ZEMAX to be available for analyzing the element. An Array of the new object (blazed element) is then attached to a glass element in ZEMAX which is populated as shown in Figure 4.14 (b) to analyze the light modulation characteristics of the electro-optic blazed grating smart window system.

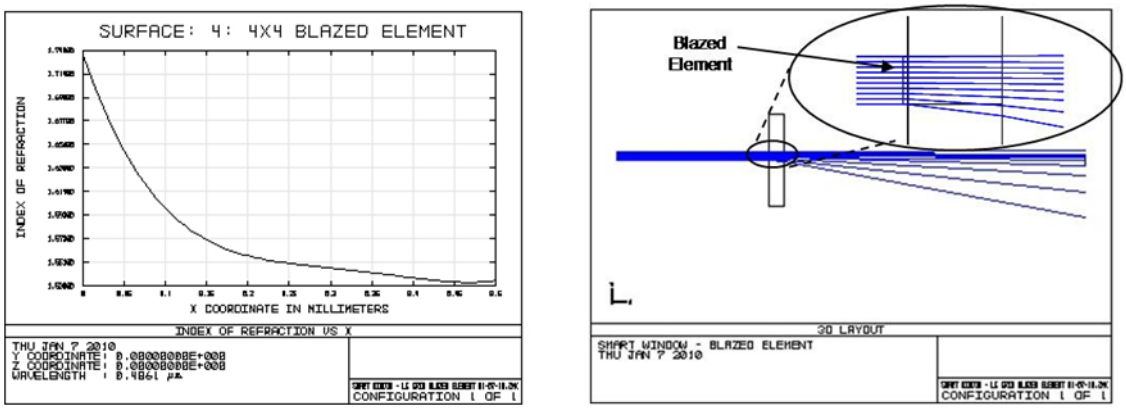

Figure 4.16: (a) Refractive index profile as read by ZEMAX. The profile matches with Figure 4.13. (b) Rays incident normally on a blazed element are bent by the blazed elements. Non-uniform refraction of rays caused by the typical index profile depicted in (a).

Figrue 4.16 (a) shows the refractive profile computed and used by ZEMAX for a glass element holding a 500 µm x 500 µm blazed element. Figure 4.16 (b) shows the blazed element progressively refracting the rays in the X-direction as directed by the graded index profile within the element.

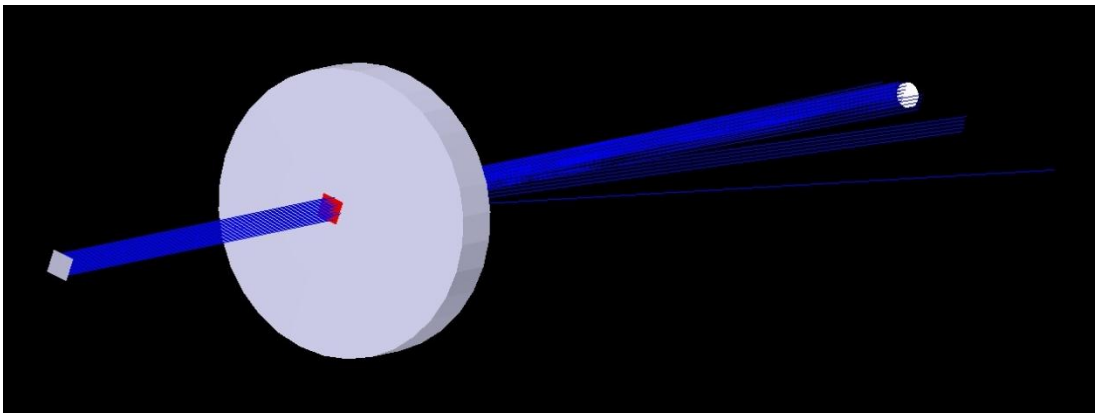

Figure 4.17: Solid model version of Figure 4.16 (b). Rays incident along X-direction are refracted as directed by the index profile while rays incident along Y transmit undeviated.

Figure 4.17 illustrates the solid model version of Figure 4.16 (b) with a perspective view. Note that the incident light polarized along the X-direction, which is the optical axis of the liquid crystal layer, is deflected while the ordinary incident light polarized along the Y-direction is transmitted without deviation. Therefore, the solar irradiance, which is unpolarized light, can be deflected by placing two layers of blazed elements in series where the optical axes (directors in the nematic liquid crystalline material) of the two blazed elements are oriented perpendicular to each other.

CHAPTER 5

MATERIALS AND FABRICATION PROCESSES

The execution of this research will benefit substantially from the applicability of the manufacturing technologies that have been developed in the last decade in the highly mature flat-panel display industry. In all of the fabrication steps, the requirements for the smart window application are less demanding than those for large flat-panel displays. But most importantly, since our optoelectronic smart window technology does not require the fabrication of thin-film transistors (TFTs)—which is the most demanding segment in display production—we expect that the overall manufacturing cost structure (per unit area) for the smart window will be significantly lower than for flat-panel displays.

This chapter introduces unit fabrication process steps to build an electro-optic device that has the ability to produce an approximated linear phase gradient which is achieved by using applied voltages within the linear region of the liquid crystal electro-optic characteristics.

At the end of this Chapter, we also introduce a unique low-cost fabrication technique for physical diffraction grating manufacturing that has not been explored previously.

The overall fabrication process flow (illustrated in Figure 5.1) that we investigated and developed is as follows:

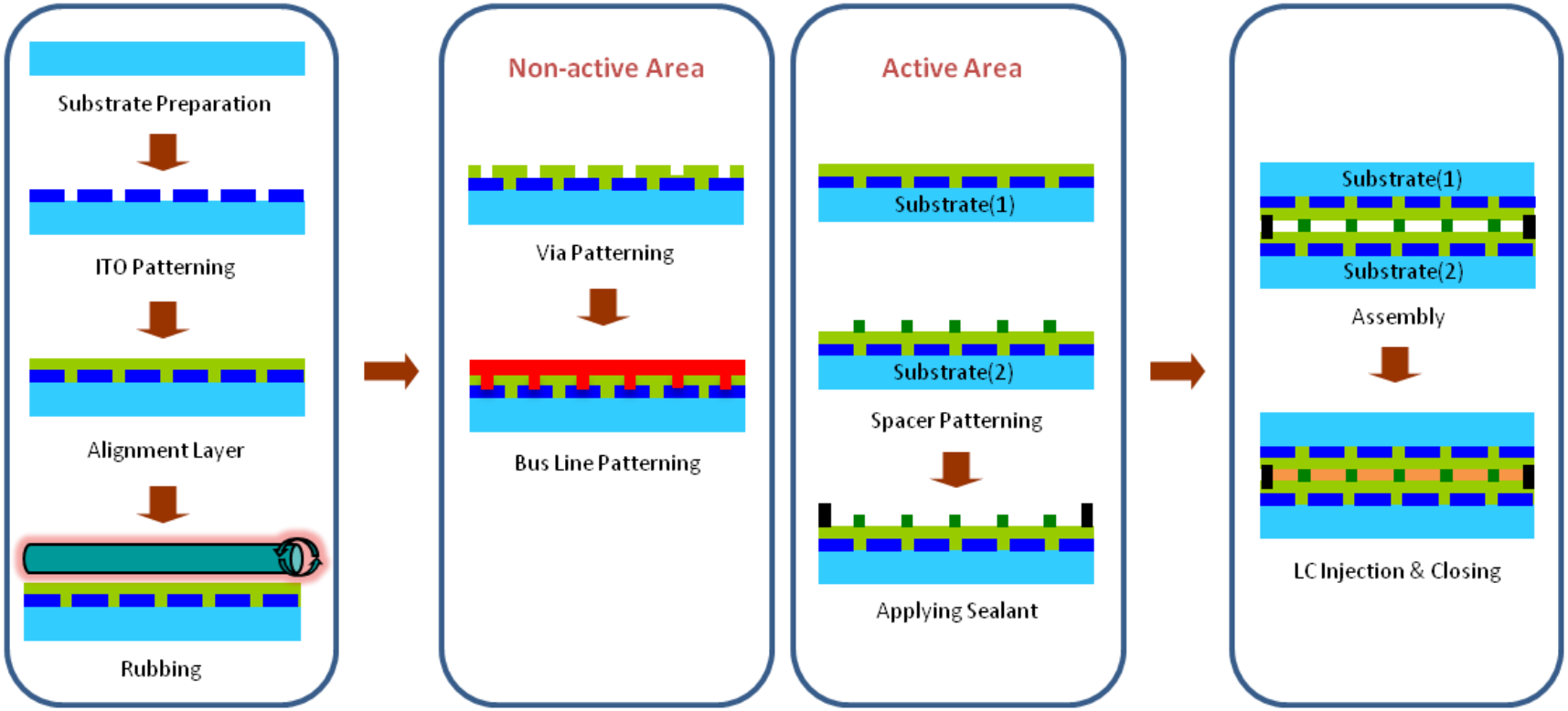

Figure 5.1: Optoelectronic smart window fabrication steps. Two window panes are prepared independently among which the process steps are divided. The panes are then assembled, the liquid crystal is injected, and the assembly is sealed.

(1) Two window panes are processed independently. High purity glass substrates, e.g., Corning 1737, which is a common glass used in LCD industry, are cleaned with chemical cleaning solutions and oxygen plasma ashing.

(2) A thin film of transparent conductive oxide (TCO, e.g., ITO) is RF-sputtered on the cleaned substrates in a controlled way to obtain good conductivity as well as high transmittance. The TCO is then patterned by photolithography followed by wet etching to form the electrodes that drive the electro-optic material, i.e. liquid crystal. Defects are inspected under an optical microscope and removed by Focused Ion Beam etching to prevent electrical shorts.

(3) A transparent polymer layer is spin-coated over the patterned electrodes and cured in a furnace to passivate the underlying electrodes. This cured polymer layer is also used as the alignment layer for the LCP. The passivated substrates are rubbed with a rotating barrel on which a rubbing cloth is attached.

(4) Extra lithographic steps are required outside the active area (blazed diffraction grating) after the cured polymer layer is rubbed. Vias are etched through the polymer layer to make contacts with the electrodes. A high-conductivity material is then deposited by e-beam evaporation on each pane and patterned to fabricate the bus lines and contact pads.

(5) Spacers provide a uniform cell gap, and are patterned using a photodefinable polyimide. A high-temperature curing cycle in an inert atmosphere is carried out to drive off any remaining solvents and to complete the imidization process.

(6) An epoxy sealant is applied on the edges of the active area, leaving an opening for LC injection. The two independently processed window panes are assembled together for a tight seal. The fabrication process is finished by injecting LCP through the opening and sealing the assembly.

5.1. Liquid Crystal Selection

LC	Δn	K11(pN)	Δε
BL009	0.281	8.9	15.5
BL006	0.278	17.9	17.3
E44	0.2627	15.5	16.8
E7	0.2246	11.1	13.8
K15	0.212	12.3	6.7
E170	0.147	11.4	5.3
ZLI-3096	0.1411	8.9	21.4
ZLI-1132	0.1396	11.1	13.1
ZLI-2471	0.1235	13.9	4.5

Table 5.1: Selected liquid crystals with high birefringence that are suitable for beam steering applications.

A variety of liquid crystal materials are commercially available, most of which are targeted for Liquid Crystal Display applications. We investigated and secured several liquid crystal candidates, listed in Table 5.1, that are suitable for beam steering applications. Important material properties for Smart Window applications include high clearing temperature (the temperature at which the liquid crystal loses its anisotropic properties and turns into an isotropic material) to ensure operability during daytime, high birefringence to reduce required cell gap and accordingly materials volume or cost, and moderate elastic constant that affects Frederick's threshold voltage and response

time. After reviewing all the candidates, we selected E7 from Merck, which meets all of the requirements stated above.

5.2. Transparent Conductive Oxide (TCO)

5.2.1. Thin-Film Deposition and Characterization

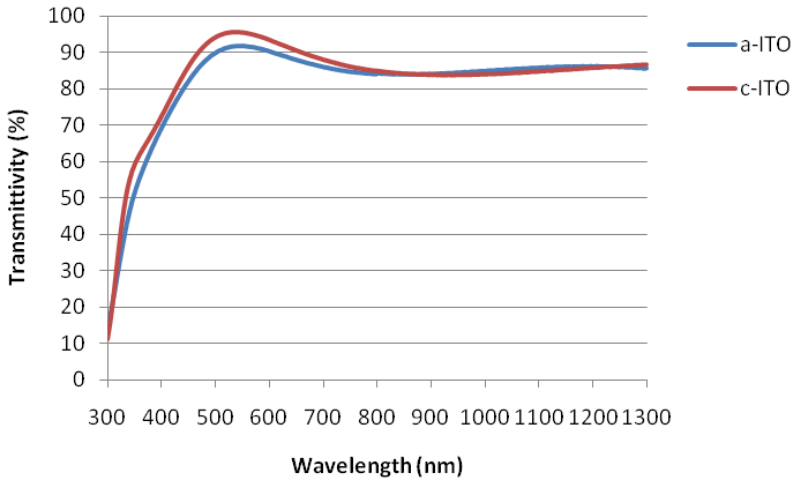

Figure 5.2: Spectral transmittance of as-deposited amorphous ITO (a-ITO) thin films by RF sputtering at room temperature and crystallized ITO (c-ITO) thin films formed by post-deposition annealing.

A thin film of a transparent conductive oxide (TCO, e.g., ITO) is RF-sputtered at room temperature on a clean glass substrate in a controlled method to obtain high optical transparency (Figure. 5.2) in the visible and near-infrared spectrum. The transmission curve is measured using Varian Cary 5G spectrophotometer.

The as-deposited ITO thin films by RF magnetron sputtering at room temperature have an amorphous structure [82-84]; thus, their electrical conductivity is

too low for them to be useful as a transparent conductive electrode. To mitigate this problem, heat treatment (post-deposition annealing) over 200°C is typically conducted to transform the amorphous ITO into crystallized ITO [83]. The annealing process parameters are optimized to be 270°C on a hot plate for 40min.

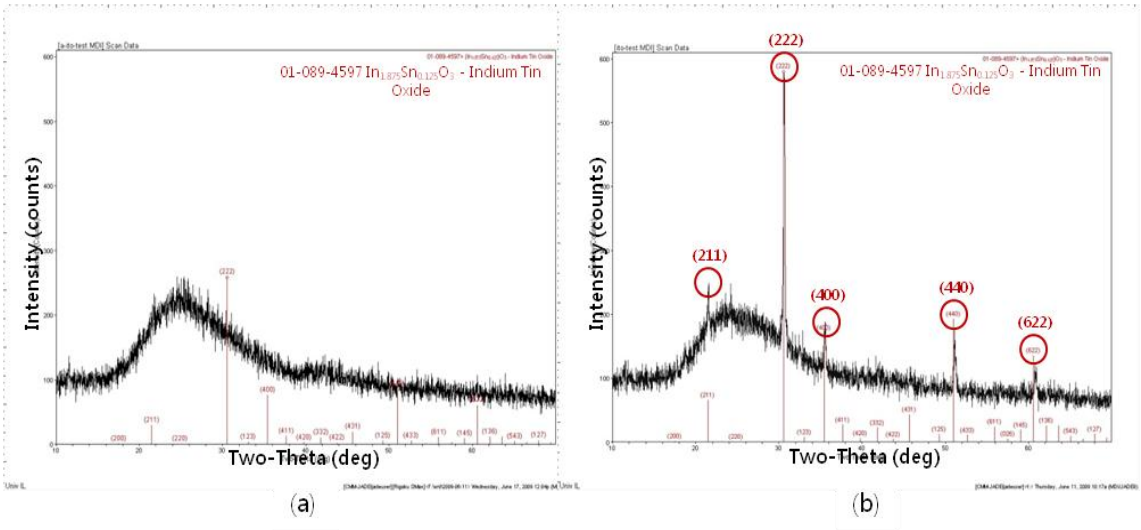

Figure 5.3: X-ray diffraction patterns of (a) As-deposited amorphous ITO and (b) Post-deposition thermally annealed crystallized ITO.

Figure 5.3 compares X-ray diffraction patterns of as-deposited ITO (Figure 5.3 (a)) and thermally annealed ITO (Figure 5.3 (b)). As expected, no diffraction peaks are observed from the as-deposited ITO while sharp diffraction peaks are seen from the thermally annealed ITO, indicating that the heat treatment successfully crystallized the ITO sample. Strong diffraction peaks observed at (211), (222), (400), (440), and (622) crystal planes match well to cubic $In_{1.875}Sn_{0.125}O_3$ phase reference peaks. Other weak diffraction peaks are difficult to identify due to noisy background intensity.

Figure 5.4 shows the change of resistivity from 3.42×10^{-2} Ωcm (as-deposited amorphous ITO) to 8.13×10^{-4} Ωcm (post-deposition annealed crystallized ITO) which is

approximately a factor of 40. The resistivity is obtained by measuring the sheet resistance with a four-point probe and dividing it by the film thickness. The optical transparency in both visible and near- infrared spectral range remained clear.

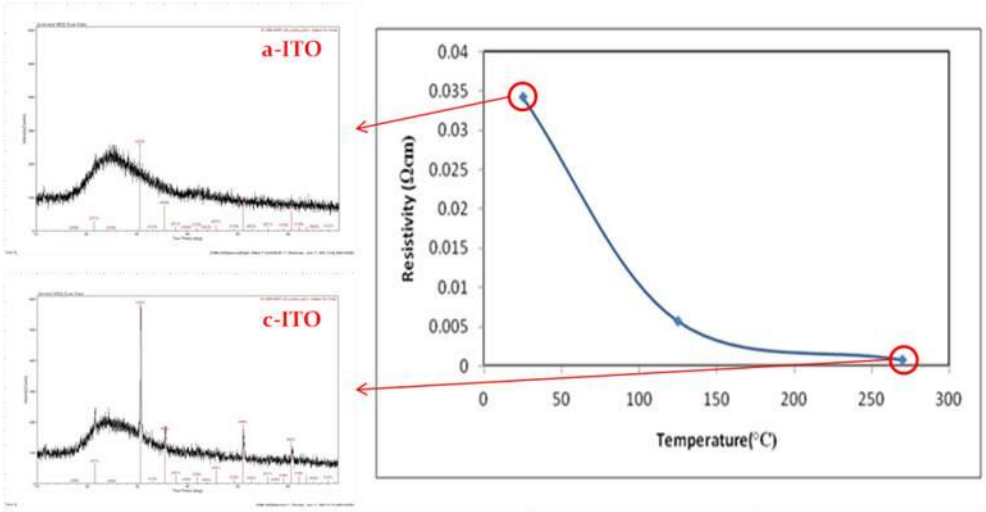

	V/I	ρ_0	ρ
Sample #1 (RT)	514	328	$3.42 * 10^{-2}$
Sample #2 (125℃)	86	55	$5.73 * 10^{-3}$
Sample #3 (270℃)	12	7.8	$8.13 * 10^{-4}$

Figure 5.4: Resistivity change of ITO thin films as a function of post-deposition annealing temperature shows the electrical conductivity increases in two order of magnitude after thermal annealing.

5.2.2. Challenges with Electrode Patterning

The TCO is patterned by contact photolithography followed by either wet etching or lift-off process to form the electrodes that drive the liquid crystal. However, defects from multiple sources are observed under the optical microscope which resulted in a short circuit. We attempted to repair the defects by using Focused Ion Beam (FIB) etching (Figure 5.5) but the limited field of view of the tool's secondary electron image makes it difficult to find and remove all defects in a 1cm by 1cm active area.

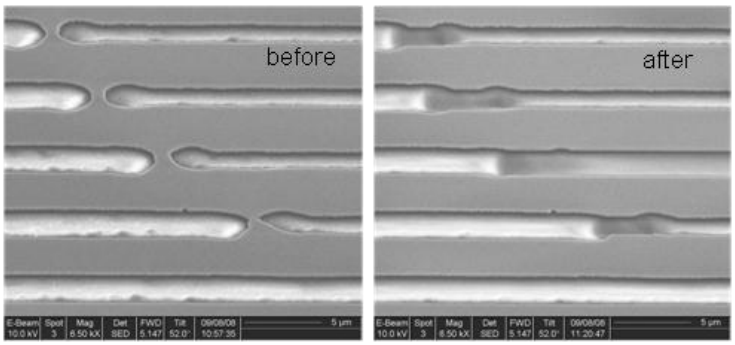

Figure 5.5: ITO defect removal by Focused Ion Beam milling process. Ga ions are extracted at 30kV with an aperture size to obtain 1000pA ion current. (a) Scanning electron micrograph of ITO defects which short the adjacent ITO electrodes. (b) Scanning electron micrograph after removing ITO defects by ion millin.

We designed the optimal electrode layout to have a 5 μm width and 2 μm spacing to work with the 1 μm alignment limit. Larger electrode spacing will ease the fabrication but it will affect adversely the grating efficiency because wider spacing, which is the area where no electric field is applied, will cause troughs in the triangular groove profile generated in the liquid crystal layer. Another disadvantage is that the grating pitch increases as the electrode width or spacing increases which, results in a smaller separation angle between near-infrared and visible that makes the device inefficient.

The electrode pitch is 7 μm, and there are 1428 contacts to be made in a 1 cm x 1 cm prototype; thus it is impractical to connect all the electrodes individually for independent control. Because a 4-step electro-optic blazed grating requires only 4 periodic variable voltages, the photomask layer is designed to connect every four electrodes together as shown in Figure 5.6 to make the driving circuitry simpler. However, this simplification brings up a new challenge in processing which originates from the inherent defects in contact lithography. Positive resist and image reversal resist

processes were developed and investigated to address this issue; however, the issue remains to be resolved.

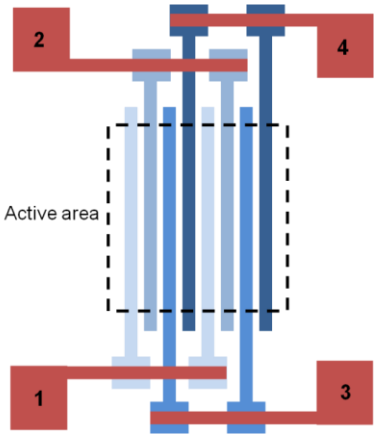

Figure 5.6: Photomask design for the transparent electrode pattern and metal interconnects.

5.2.2.1. Positive Photoresist

As shown in Figure 5.7, there are two possible defect scenarios; a) Particles on top of the developed photoresist pattern, and b) damaged patterns by variable causes such as contaminated mask, physical damage (rip-off), air bubble, etc.

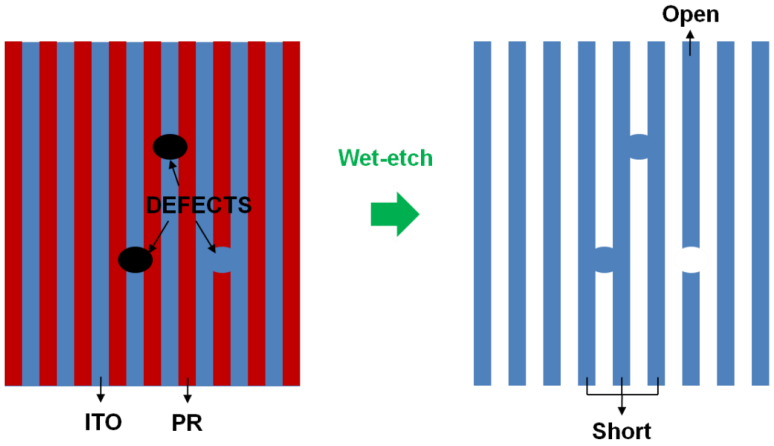

Figure 5.7: Wet-etching process to pattern transparent electrodes using positive resist with more shorted than open electrodes caused by defects.

In the former case (which is more dominant than the latter case), the wet etchant cannot reach the areas that is supposed to be etched, thus resulting in shorted electrodes. The latter case results in an open electrode which is acceptable if there are only a few of these on the sample.

5.2.2.2. Image Reversal Photoresist

This is an alternate process to pattern positive resist. Since particles sitting on top of developed photoresist are regarded as a major issue in the positive resist process, this method is intended to reverse shorted electrodes to open electrode, as shown in Figure 5.8. However, damaged photoresist pattern exists where the ITO is deposited and where the pattern is supposed to lift-off, resulting in a shorted electrode. Nevertheless, compared to the conventional wet etching process, there are more open electrodes than shorted electrodes, so this is preferred for defect removal using the FIB etching system.

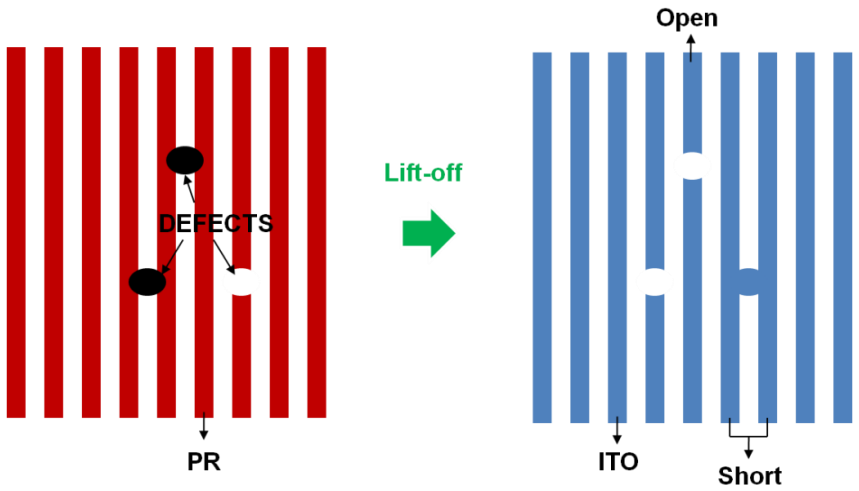

Figure 5.8: Lift-off process to pattern transparent electrodes using image reversal resist with more open than shorted electrodes caused by defects.

5.2.2.3. Current Status

Repairing defects using an FIB etching system is easier in the case of image reversal process because there are fewer defects which cause a short circuit. However, the number of open electrodes is still high; this might reduce the blazing efficiency drastically. There are also a few unfound defects that generate short electrodes that causes the device to malfunction. Currently, contact lithography is the most convenient equipment in Micro and Nanotechnology Laboratory (MNTL) that is suitable for the 1 μm alignment requirement, although projection lithography is preferred in the microfabrication industry for defect-free processes. In the next section, we describe our investigation of an alternative patterning technology that uses a projection excimer laser lithography system that could possibly address the challenges in defect-free electrode patterning.

5.2.3. Alternative Patterning Method Utilizing Excimer Laser Crystallization

As the defects generated by contact lithography pose challenges for the fabrication of a working prototype device, we further investigated high-resolution patterning of ITO thin films by a selective crystallization process using low-fluence excimer laser irradiation and we reported the results described below [85]. We demonstrated the selective crystallization process using a large-area excimer laser projection system to fabricate desired patterns. The patterns were clean and sharp, their overall quality being suitable for use in high-volume production of electronic devices.

For the initial structure, a 60 nm thick ITO layer was deposited on a Corning 1737 glass substrate by sputtering (Figure 5.9 (a)). The substrate was not heated during the deposition process to ensure that the deposited ITO is amorphous. After deposition, the amorphous ITO (a-ITO) was selectively crystallized using an excimer laser projection system as shown in Figure 5.9 (b). The substrate was then dipped in a diluted HCl solution for an empirically determined optimized time. In this wet etch process, the a-ITO is removed selectively due to its higher etching rate compared to that for polycrystalline ITO (p-ITO), enabling the formation of patterns of p-ITO, as shown in Figure 5.9 (d). Note that there is no photoresist-related process required in this technique for patterning of ITO thin films as described in Figure 5.9; only the exposure and etching steps were needed.

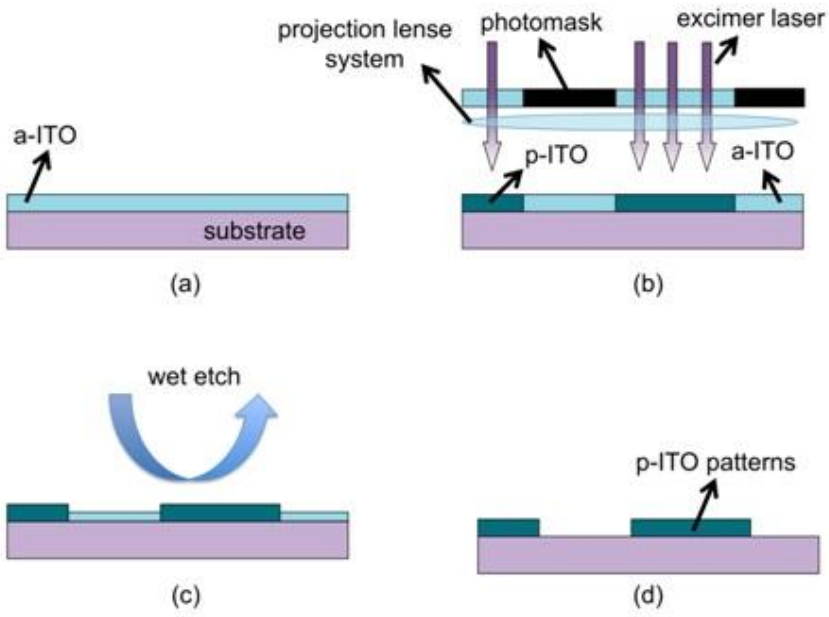

Figure 5.9: Schematic illustration of high-resolution ITO patterning process by excimer laser projection crystallization technique. (a) Amorphous phase ITO (a-ITO) is deposited on a substrate by room temperature sputtering process. (b) a-ITO is crystallized selectively by excimer laser projection crystallization process. (c) Wet etch process for optimized process time removes a-ITO and polycrystalline ITO (p-ITO) remains because p-ITO has a lower etch rate than a-ITO. (d) Patterns of p-ITO are formed after a cleaning process.

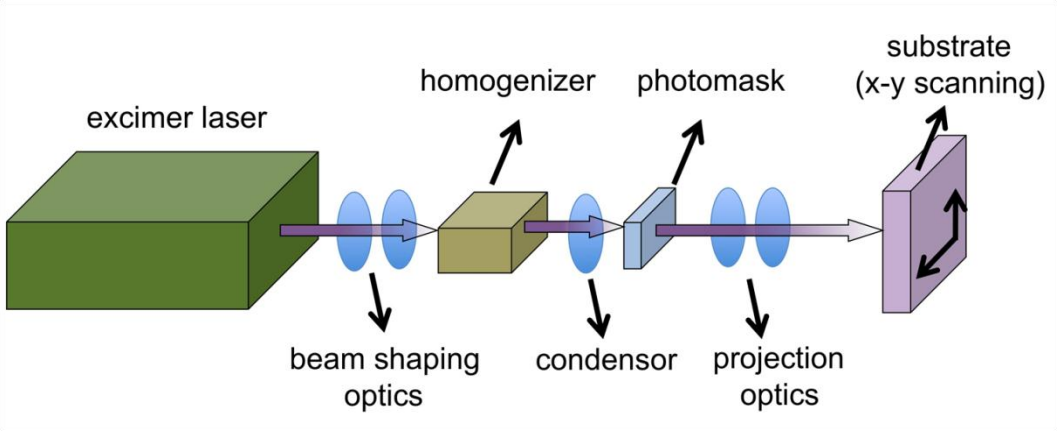

Figure 5.10: Schematic illustration of the excimer laser projection system used in the experiments. A beam homogenizer was used to make excimer laser beam spatially uniform. A photomask was used to make patterns on the substrate. The substrate stage can move in x and y directions by system control software.

Figure 5.10 shows a schematic illustration of the excimer laser projection system used in these experiments. A 248 nm KrF excimer laser was used as the irradiation source. The pulse repetition rate of the laser was 50 Hz. A beam homogenizer was used to make the excimer laser beam spatially uniform. The exposure fluence at the substrate was 45 mJ/cm^2. The substrate was scanned in two directions for the large-area patterning process. The excimer laser, the photomask, and the substrate stage were controlled automatically by the exposure system operating software. With this system, it is possible to expose substrates of sizes up to 500 mm by 500 mm with 5 μm pattern resolution using our experimental configuration.

Before fabricating ITO patterns using the above excimer laser projection crystallization process, we investigated the process of crystallization of ITO films under various exposure conditions without imaging through a photomask. First, we investigated the effect of excimer laser irradiation on crystallization of the amorphous as-deposited ITO thin films by X-ray diffraction measurements (XRD). Measurements

were performed on a Rigaku D-max diffractometer using Cu K_α radiation at 40 kV and 20 mA.

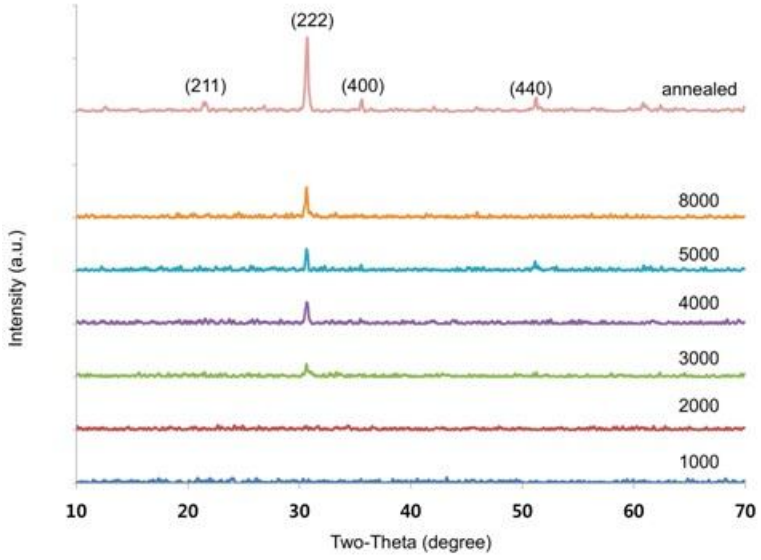

Figure 5.11: XRD peaks of ITO samples after exposure by various numbers of excimer laser pulses. As the number of excimer laser pulses is increased, the height of the strongest peak increases because the ITO is more crystallized. The peak from thermally crystallized ITO is shown for comparison.

XRD patterns of a-ITO samples exposed to different numbers of laser pulses are shown in Figure 5.11. It is observed that crystallization takes place as the number of pulses increases to over 3000 and that it happens preferentially along the <111> crystalline direction. The strongest diffraction peak was reached at 10000 pulses; the diffraction peak intensity decreased thereafter. Post annealing of the laser crystallized samples led to sharp peaks of In_2O_3:Sn cubic phase, indicating partial crystallization by the laser process. Since temporary heating by the absorbed pulsed UV laser light controls the crystallization [86, 87], we can attribute partial crystallization to heat dissipation during the scanning exposure process. From the results in Fig. 5.11, we thus

verified that the a-ITO is transformed into p-ITO when exposure energy from the excimer laser is sufficient.

Figure 5.12 (a)-(d) show patterns of p-ITO after excimer laser crystallization and wet etch process. Figure 5.12 (a) illustrates the result obtained when the degree of crystallization is not sufficient. If the number of excimer laser exposure pulses is not sufficient, the irradiated a-ITO is not transformed into p-ITO completely, and therefore the ITO pattern is damaged during wet etch process. By increasing the number of exposure pulses, we were able to fabricate clean patterns of ITO when the number of pulse was optimized, as shown in Figure 5.12 (b)-(d). Figure 5.12 (b) shows a scanning electron microscope (SEM) image of circular dots of p-ITO. Figure 5.12 (c) is a magnified SEM image of the p-ITO circular dots, and Figure 5.12 (d) presents line patterns of p-ITO, fabricated to check the line-edge linearity of the patterns. As Figures 5.12 (b)-(d) demonstrate, we have been able to fabricate clean patterns of ITO using the excimer laser projection crystallization process. The quality of the patterns achieved by this process is sufficiently clean and sharp so as to be suitable for use in high-volume production of flat-panel displays and other electronic devices. In these experiments, we fabricated the ITO patterns on a 50mm by 50mm substrate; the substrate size limitation arises from the ITO deposition process, rather than from our excimer laser projection crystallization process, which is capable of patterning ITO films on 500 mm by 500 mm substrates with our current equipment. The patterns on the entire substrate have uniform quality, and we did not find any ITO residue after the process.

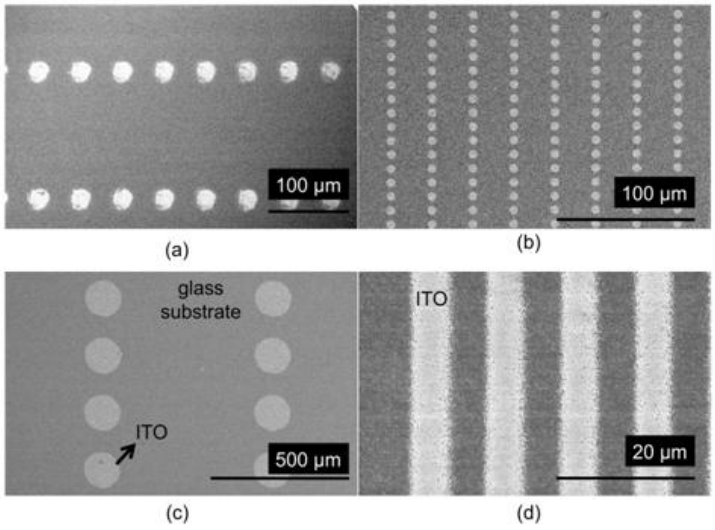

Figure 5.12: SEM images of ITO patterns fabricated by exposure with a large-area excimer laser scanning system followed by wet etching. (a) When the number of laser pulses was 1000, the crystallization was not enough and the patterns were damaged by the wet etchant. (b) Patterns of clean ITO patterns fabricated when the number of excimer laser pulses was 4000. The white dots are the ITO patterns remaining on the glass substrate. (c) Magnified image of (b). (d) Line patterns of ITO showing the linearity of the pattern line edges. This sample was fabricated using a different, small-area excimer laser projection system because of mask compatibility consideration.

One of the significant advantages of this patterning process is that photoresist-related processes are not required. The cost of device production is reduced because the photoresist material and the corresponding application, development and stripping processes are eliminated. Since the cost of equipment is also reduced, both the cost of manufacturing and cost of ownership decrease correspondingly. Equally importantly, the process conditions are suitable for use in high-volume production. Since the excimer laser projection crystallization process uses low-fluence excimer laser radiation, there should be no damage to the underlying structures. As described above, we used a fluence of 45 mJ/cm^2 for the crystallization, which does not cause damage in conventional materials used in microfabrication processes. Typically, common materials in TFT-LCD fabrication are damaged only when exposed to laser fluences higher than ~100 mJ/cm^2 [88, 89].

5.3. Liquid Crystal Alignment Layer

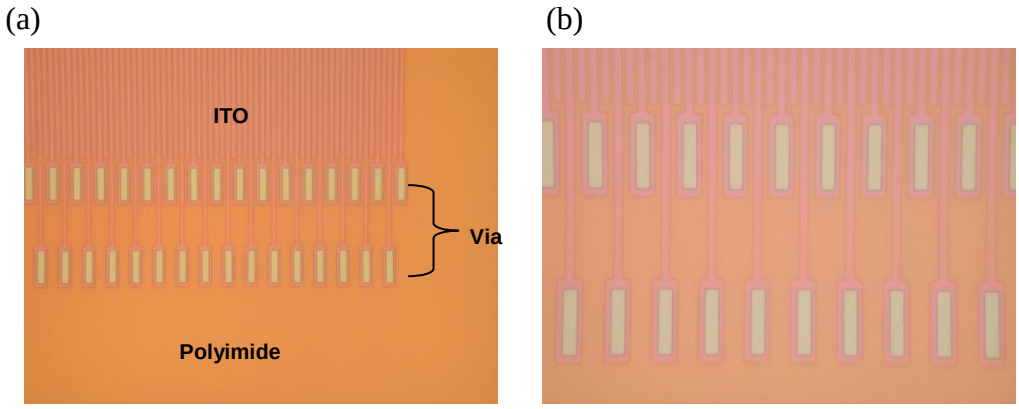

Figure 5.13: (a) Optical micrograph of Glass-ITO-Polyimide layer structure (b) Magnified image of vias.

Figure 5.13 shows a 3-layer structure (Glass-ITO-Polyimide) where vias are opened through the polyimide layer to the ITO contact pads. The polyimide layer insulates the underlying patterned ITO when metal is deposited for interconnects. The polyimide layer needs to be cured in the furnace with N_2 gas in a controlled manner, as shown in Figure 5.14.

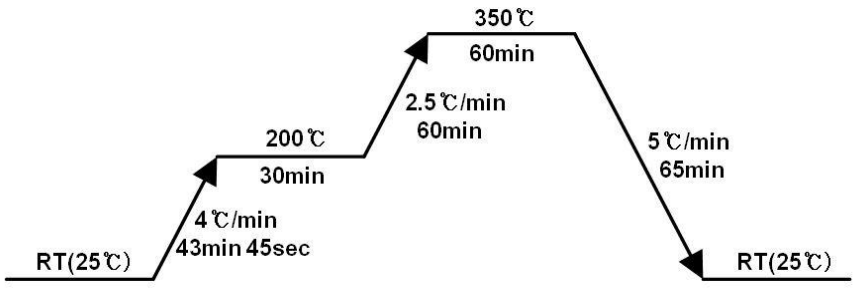

Figure 5.14: High temperature furnace curing cycle for polyimide imidization.

The curing process is essential for the imidization of the polyimide, which gives good mechanical strength and chemical safety. Once the polyimide layer is cured, it is

also used as a dielectric layer to provide an electric field across the sandwiched liquid crystal layer and as an alignment layer to allow the liquid crystal molecules to arrange to a preferred direction.

5.4. Rubbing Process

If the liquid crystals are injected into an empty cell, their optical axes (directors) distribute randomly causing the material to behave as an isotropic material even though each liquid crystal molecule is anisotropic. Therefore, a rubbing process is necessary to form mechanical grooves for molecular directions on the polyimide surface; the grooves align the anisotropic liquid crystal molecules along the rubbing direction and make the whole cell an anisotropic medium.

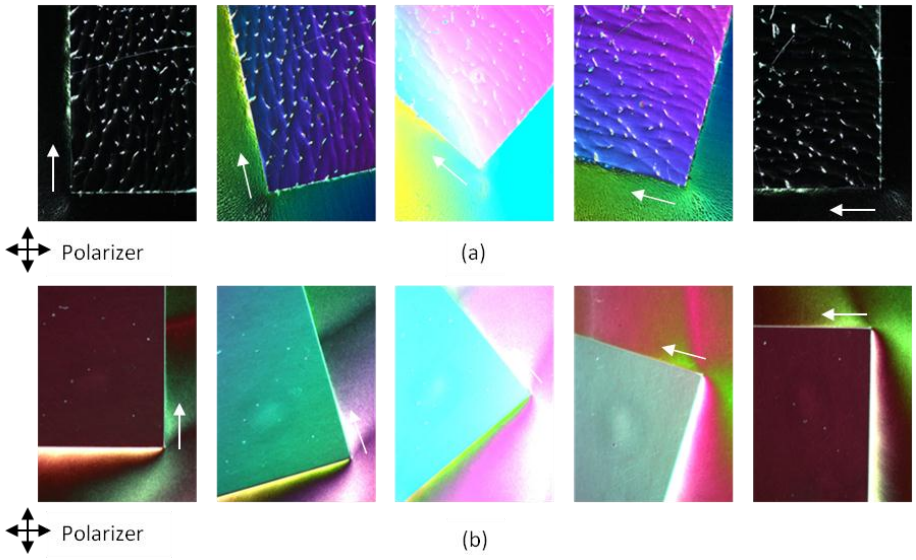

Figure 5.15: Cross polarized microscope image of a fabricated cell filled with liquid crystal to check proper alignment. (a) Hand rubbed alignment layer shows rough texture. (b) Roller rubbed alignment layer shows smooth texture.

The integrity of proper alignment is verified by observing the change of light transmission when the liquid crystal cell is placed and rotated in a crossed polarized microscope (Figure 5.15). The polarizing microscope is used to examine the texture of the liquid crystal surface. Placing the liquid crystal cell between polarizers that are placed perpendicular to each other in the polarizing microscope can verify homogenous planar alignment. By rotating the cell, transmission intensity gradually increases for both samples, reaching highest transmission at 45^{o} and then decreasing back to extinction when the rubbing direction, that is the optical axis of the liquid crystal, is parallel to either polarizer. This indicates that the liquid crystal is homogeneously aligned to the rubbing direction.

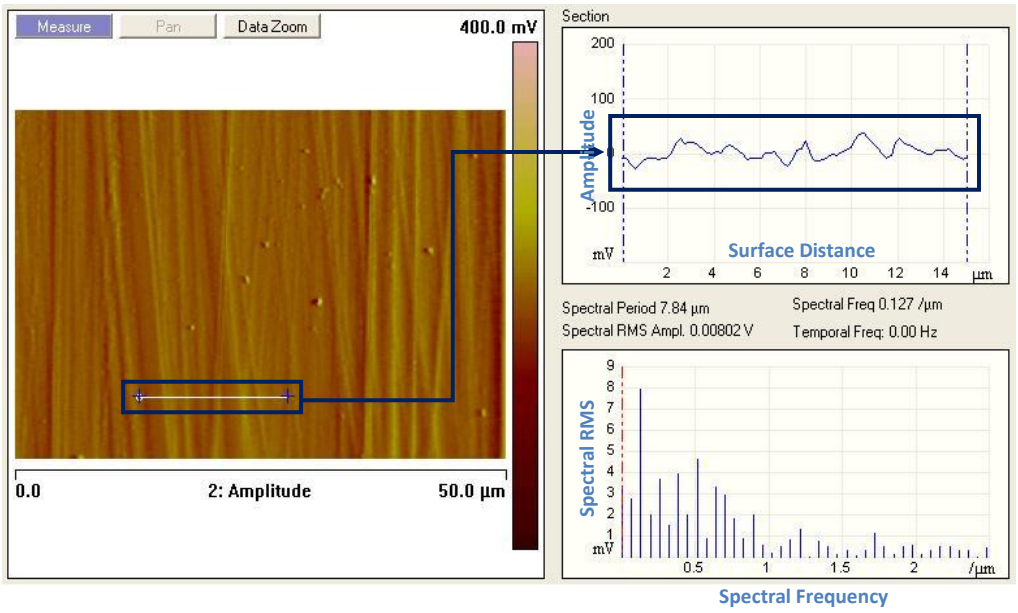

Figure 5.16: AFM image of polyimide surface rubbed by microvelvet cloth attatched to a rotating barrel.

Rubbing can be performed either by hand or by using a motorized roller with an attached micro-velvet cloth. We investigated both processes and observed that hand rubbed surface (Figure 5.15 (a)) was damaged more than roller rubbed surface (Figure

5.15 (b)). This can be attributed to the irregular force applied on the surface by hand while the roller applies uniform rubbing force.

The substrate stage is positioned 1.23 mm apart from the roller and the thickness of the glass substrate is 0.5 mm. The lengths of the micro-velvet cloth's fibers are measured to be approximately 1.4 mm long, so there is good contact between the polyimide surface and the micro-velvet fibers. The substrate travels back and forth 10 times through the roller with a rotation speed of 1400 rpm. Fine and coarse grooves are observed as shown in Figure 5.16 with surface roughness less than 20 nm. These grooves align nematic liquid crystals in a homogenous planar orientation.

5.5. Spacer Patterning

Spacers provide a uniform cell gap and are patterned using a photodefinable polyimide. Cured polyimide provides good mechanical strength to keep the cell gap consistent which is important because the change of cell gap will affect the driving voltage for the liquid crystal device. The advantage of using photodefinable polyimide over the typical glass bead material widely used in LCDs is that spacers can be exactly patterned uniformly and placed sparsely to reduce light scattering whereas glass beads tend to aggregate and act as a scattering source. Another advantage is that the spacer conforms strongly to the same type of polyimide alignment layer surface. Since spacers contribute to light scattering which can affect the device performance, we patterned a spacer density of less than $100/mm^2$ [90].

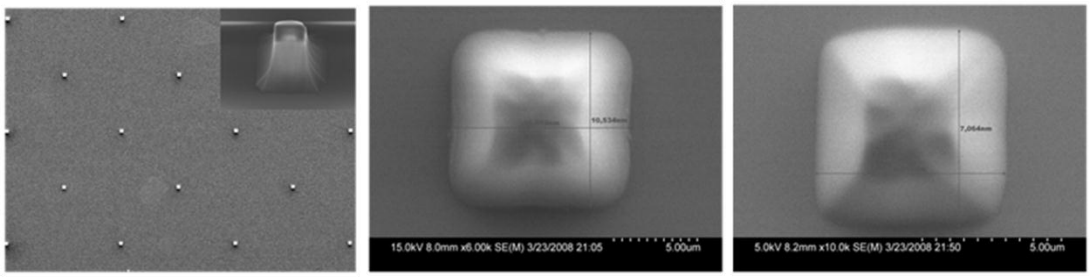

(a) (b) (c)

Figure 5.17: SEM images of spacers patterned by a photodefinable polyimide. (a) Low magnification image of spacer distribution with density of 50/mm^2. Inset shows a prospective view of a spacer. (b) Spacer dimension before curing is ~10 μm x ~10 μm. (c) Spacer dimension after curing is ~7 μm x ~7 μm..

Figure 5.17 (a) shows patterned spacers with a density of 50/mm^2 on top of the alignment layer. The originally designed dimension of the spacer is ~10 μm x ~10 μm as seen in Figure 5.17 (b) which is measured before curing. A high-temperature curing cycle in an inert atmosphere is again carried out as described in Section 5.3 for the alignment layer to drive off any remaining solvents and to complete the imidization process. After curing, we observed the spacer dimensions to have reduced to ~7 μm x ~7 μm, as shown in Figure 5.17 (c).

5.6. Cell Gap Measurement

Accurate measurement of empty cell gap is important because it directly affects the Frederick's threshold voltage and the driving voltage of the liquid crystal device. Optical interferometric methods are commonly used to measure cell gaps. The most widely used methods are rotation interferometric method, split-beam interferometric method, and spectral interferometric method [91]. We adopted spectral interferometric

method where Fabry-Perot type multiple interference peaks as a function of wavelength are measured to determine the cell gap value by [92],

$$d = \frac{m}{2n} \times \frac{\lambda_2 \times \lambda_1}{\lambda_2 - \lambda_1} \tag{5.1}$$

where d is the cell gap, m is the number of interference cycles, n is the refractive index of sandwiched medium, and λ_1, λ_2 are the wavelength dependent transmission maxima.

The interference peaks of an empty cell composed of a glass substrate with other thin films deposited on it look like a superposed sine wave that is composed of multiple sine waves representing each layer. However, the interference peaks for the air gap can be deduced practically since the thick glass substrate results in much finer oscillation peaks, and the various thin films give much coarser oscillation peaks.

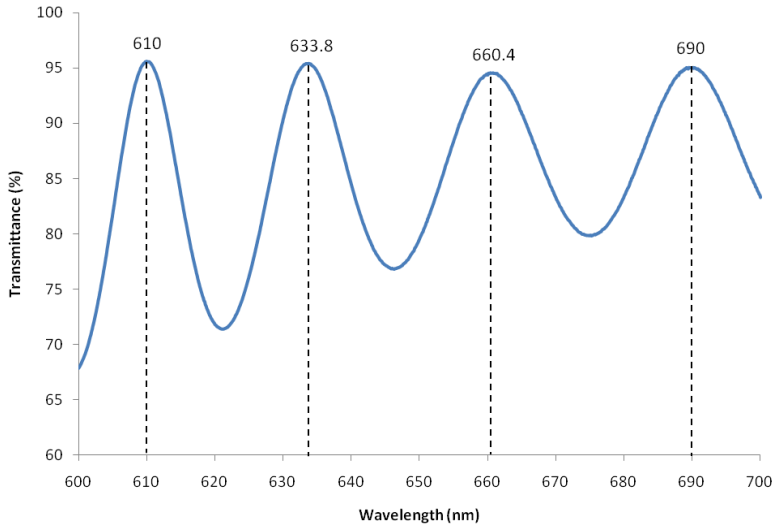

Figure 5.18: Transmittance curve of a fabricated empty cell before liquid crystal injection which is separated by photodefinable spacers.

Figure 5.18 is the transmitted intensity as a function of wavelength for a fabricated cell separated by photodefinable polyimide spacers which shows Fabry-Perot interference oscillations of the air gap. Four interference peaks are found and used to calculate the cell gap from Equation 5.1 to be 7.89 μm.

The thickness of the spacer dictates the cell gap which is an important parameter in the electro-optic blazed grating. For example, the cell gap needs to be larger than 5 μm for a 1 μm target wavelength to generate 2π phase reset in an optical medium that has birefringence of 0.2

5.7. Liquid Crystal Injection

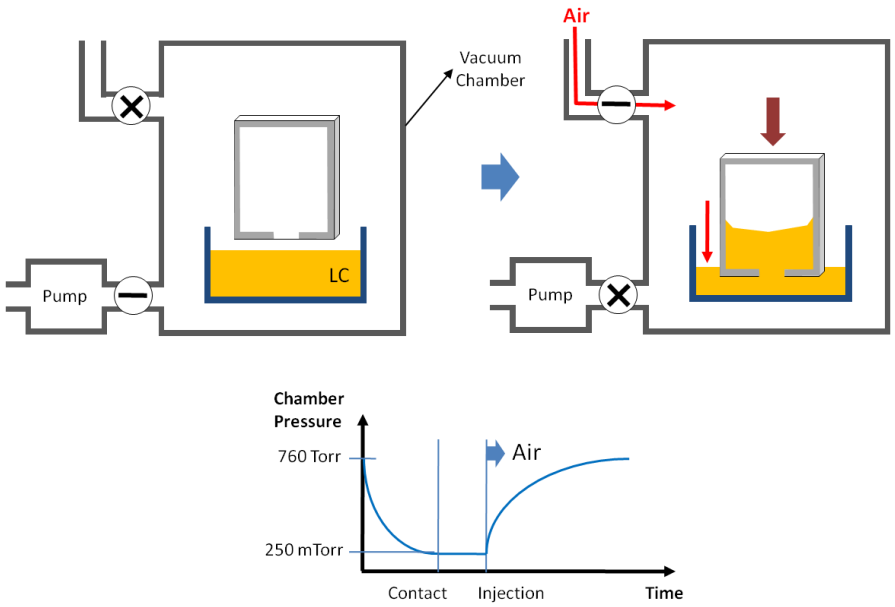

Figure 5.19: Schematic illustration of the vacuum chamber for liquid crystal injection. The fabricated empty cell is first evacuated to 250mTorr. Lowering the cell in contact with the liquid crystal bath causes partial filling by the capillary effect. Afterwards, flowing air into the chamber completes the liquid crystal filling process.

We have built an in-house vacuum chamber with a manipulator that holds the fabricated empty cell while the air inside the cell is pumped out down to 250 mTorr, and then lowers the cell into the liquid crystal bath for injection by capillary force as illustrated in Figure 5.19. After allowing the capillary force to inject initially the liquid crystal into the empty cell, the chamber is brought back to atmospheric pressure which completes the filling process.

5.8. Excimer Laser Photoablation for Physical Blazed Gratings

In this section, we introduce a novel method for fabricating physical blazed gratings using angled photoablation and *in-situ* masking. This fabrication technique offers a low-cost approach with customizability of grating pitch and grating angle such that we can make optimally designed gratings that are not commercially available.

5.8.1. Introduction

Excimer laser photoablation is the process of using deep ultraviolet (DUV) radiation to pattern or etch a material directly (i.e., without requiring a post-exposure development step), and is often used for patterning of polymers. The excimer laser energy strikes the polymer surface with enough energy to cause bond-breaking of polymers through photochemical and photothermal processes. Excimer laser photoablation has been demonstrated for the fabrication of various electronics, optoelectronics, microfluidic and MEMS devices [93-95].

Excimer lasers are pulsed lasers; thus, the ablated depth can be precisely

controlled by modulating the fluence or the number of laser pulses. The threshold fluence for ablation is the lowest fluence at which the material can be effectively patterned or etched, and is known to be less than 50 mJ/cm^2 for many polymers [96-98]. Excimer lasers also remove thin films of metals at higher fluences [93, 96]. The threshold fluence for removal or damage to metal films is a function of the metal thickness and thermal conductivity of the material [96]. Generally, since the threshold fluence for photoablation of polymers is much lower than the threshold fluence for removal or damage of high-thermally-conductive metals [96, 97], metal thin films can be used as *in-situ* masks for polymers if the proper fluence is used. In addition, thermal barriers such as SiO_2, placed between polymer and metal thin films, are effective in isolating the polymer-inorganic thin-film interface from high temperatures experienced during photoablation and thus improve the viability of the *in-situ* mask [99].

5.8.2. Excimer Laser Photoablation Setup

A prototype system is set up for excimer laser photoablation using a 248 nm KrF excimer laser (GSI Lumonics PM844). Initial experiments use the flood photoablation path to examine ablation characteristics for future experiments. The experimental setup is as follows (Figure 5.20): The laser beam passes through an attenuator to reduce the intensity of the light output and then through a system of cylindrical convex lenses and a spherical convex lens to reshape the laser. There is one convex lens after the rectangular aperture; this lens converges the excimer laser light such that varying the distance between the square aperture and the substrate holder varies the area in which the laser light strikes the substrate while keeping the total energy constant, thereby changing the fluence of the laser light. The fluence can also be modified by removing quartz plates

from the attenuator and changing the excitation voltage of the excimer laser. A simple Debris Removal System (DRS) was used by attaching Teflon tubing to N_2 cylinder and adjusting the nozzle and pressure for N_2 blowing during the photoablation process.

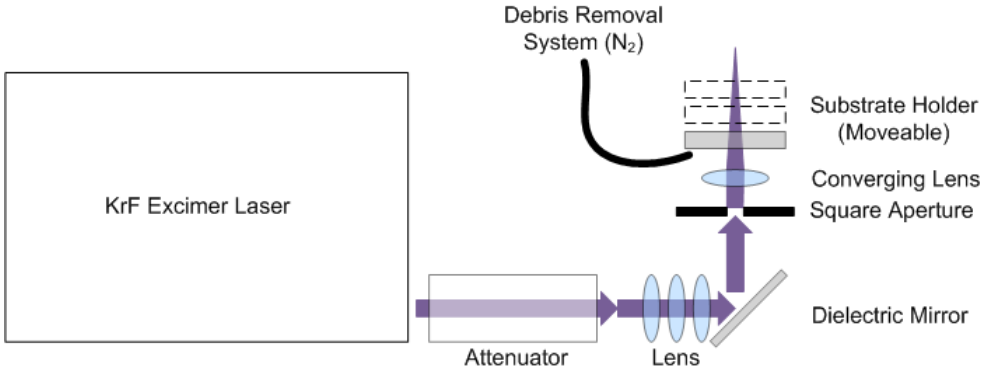

Figure 5.20: Schematic of photoablation experimental setup.

5.8.3. Concept for Fabrication of Blazed Gratings

The fabrication process for blazed gratings is as follows. First, aluminum metal is deposited on a polymer substrate using the RF sputtering process (Figure 5.21 (a), Figure 5.21 (b)). The metal is patterned and etched using positive photoresist and a chemical etchant. The sample is then exposed to excimer laser energy to selectively pattern the polymer; during this process, the patterned metal gratings serve as *in-situ* masks (Figure 5.21 (c)). To obtain a blazed pattern, the substrate is placed at an angle with respect to the incident laser beam during the ablation process. The fabrication process concludes with an O_2 plasma ash process to remove the ablated polymer debris, and a wet etch to remove the aluminum *in-situ* mask (Figure 5.21 (d)).

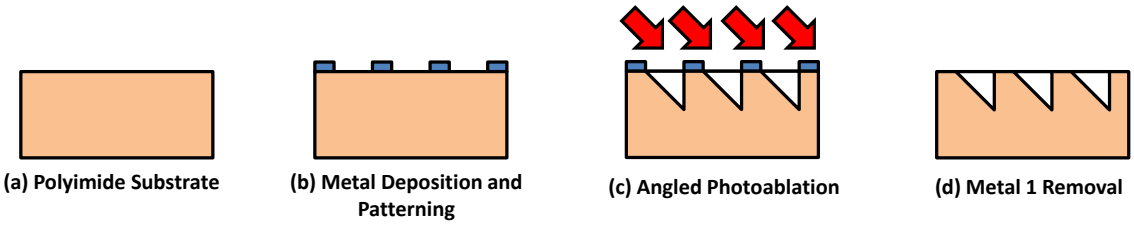

Figure 5.21: Fabrication process for blazed gratings.

The laser ablation process creates non-vertical side-walls due to near-field diffraction (Fresnel diffraction) interactions with the *in-situ* mask and the substrate. These effects cause a decrease in overall fluence near the edges of the mask. Thus, the sections of the polymer near the *in-situ* masks will not be ablated, and will form a shadow for subsequent laser pulses (Figure 5.22 (b)). Therefore, the side-wall angles are a function of the substrate angle with respect to the incident beam, the laser fluence, and the polymer substrate. This process iterates with additional pulses until two adjacent side-walls meet, forming a corner and creating an "etch-stop" which prevents further ablation from occurring (Figure 5.22 (c)).

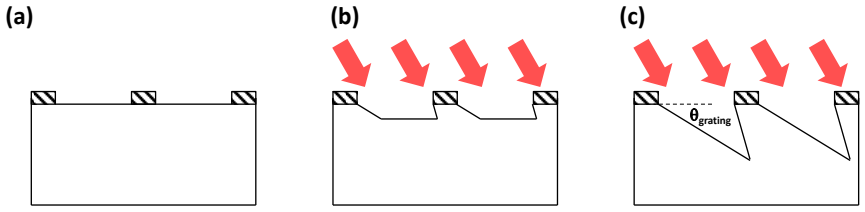

Figure 5.22: Formation of blazed grating using angled ablation. (a) Initial Sample. (b) After 1 pulse, the edges near the mask receive less fluence due to near-field diffraction and thus form a shadow for subsequent ablation. (c) After many pulses, the sidewalls meet and thus form an edge-stop. The grating angle is defined as $\theta_{grating}$ in the figure.

5.8.4. Experimental Results

A few samples were fabricated using the processes described in the previous part. Samples consist of 1 μm thick aluminum metal patterns on a 25.4 μm (1 mil) thick

Kapton E Polyimide flexible substrate. Samples were patterned with gratings having 32 μm pitch; some samples consisted of 8 μm line and 24 μm space features, while others consisted of 16 μm line and 16 μm space (32 μm pitch) features. Samples were ablated using various fluences and incident angles: Sample A was ablated at a 30 degree incident angle at 80 mJ/cm^2, Sample B was ablated at 45 degree incident angle at 65 mJ/cm^2, and Sample C was ablated at 50 degree incident angle at 75 mJ/cm^2.

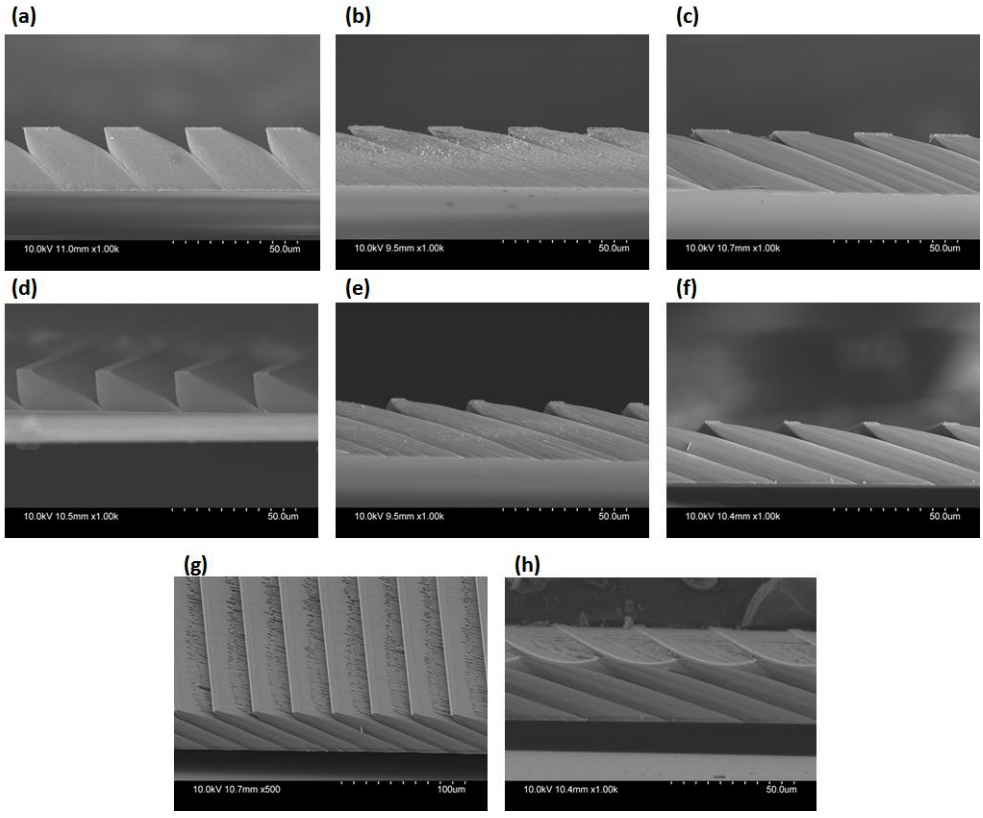

Figure 5.23: Scanning electron micrographs of blazed gratings. (a) Sample A with 16 μm line and 16 μm space. (b) Sample B with 16 μm line and 16 μm space. (c) Sample C with 16 μm line and 16 μm space. (d) Sample A with 8 μm line and 24 μm space. (e) Sample B with 8 μm line and 24 μm space. (f) Sample C with 8 μm line and 24 μm space. (g, h) Blazed grating showing conical defects and surface striations.

The samples were cross-sectioned and examined using SEM to determine the angle of the blazed patterns, the pattern repeatability, and also defects in the grating patterns. SEM reveals a sidewall angle of 24 degrees for Sample A (Figure 5.23 (a), (d)),

9 degrees for Sample B (Figure 5.23 (b), (e)), and 10 degrees for Sample C (Figure 5.23 (c), (f)). Even though incident angle for Sample C were the greatest (50 degrees), Sample B actually exhibited the shallowest grating angles because this sample was ablated at the lowest fluence, indicating that both incident angle and incident fluence affect the sidewall angle of the blazed grating.

SEM reveals that there are conical defects and surface striations which may reduce grating efficiency (Figure 5.23 (g), (h)). Conical defects are present in the ablated regions because some ablated debris redeposits on the surface which then acts a mask for additional ablation. Surface striations may be caused by line edge roughness in the metal features or diffraction patterns associated with adjacent gratings. Process optimizations such as increasing laser fluence or using a more effective debris removal system may minimize defects during the ablation process.

After SEM, the samples were placed in a metal etchant to remove the gold coating (which was applied during SEM preparation), and the aluminum in-situ mask. Samples were examined in the optics lab for evidence of a blazed diffraction profile. These blazed gratings exhibit a blazed grating profile for both the visible and infrared wavelengths at a normal angle of incidence to the beam (Figure 5.24 (b), (e), (f)). The sample was then tilted to an oblique angle of incidence (Figure 5.24 (c)), and the blazed angle is observed to increase, which follows the theoretical behavior described in the previous sections. Defects on the grating surface during the ablation process decrease the overall efficiency of the grating; we observe the decreased efficiency through the presence of multiple beams in the diffracted pattern.

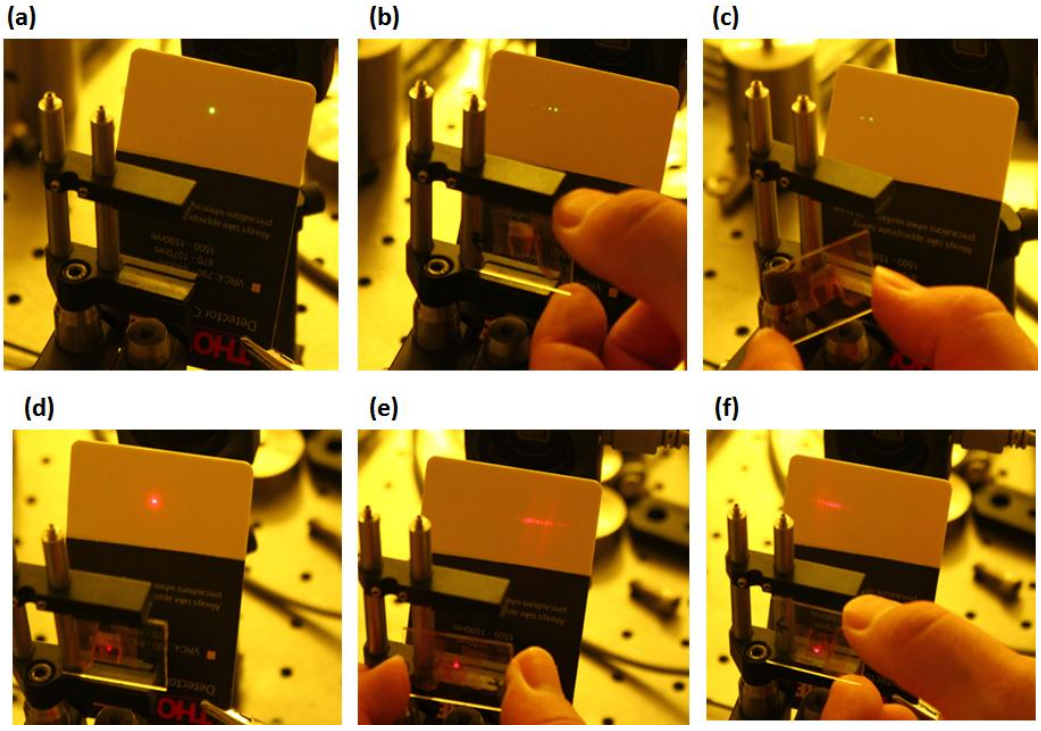

Figure 5.24: Optical images of blazed grating diffraction experiments. (a) Infrared light with no grating. (b) Infrared light passing through blazed grating at normal incidence. (c) Infrared light passing through diffracted beam at angled incidence. (d) Visible Light with no grating. (e) Visible light passing through blazed grating at normal incidence. (f) Visible light passing through blazed grating at normal incidence (the grating is rotated 180 degrees).

We have demonstrated a novel method for low-cost fabrication of blazed gratings on polymer substrates which permits the fabrication of gratings with very shallow grating angles (less than 10 degrees). The grating angles are determined by the angle of incidence, the ablation fluence, and the polymer material. Initial experiments show successful fabrication and test of the blazed gratings; however, future experiments will be needed to optimize the blazed grating quality for maximum efficiency.

CHAPTER 6

CONCLUSIONS

6.1. Summary

U.S. energy consumption will increase unprecedentedly in the next 20 years according to the Department of Energy (DOE). DOE also predicts that energy supplies will be unable to meet the demand. The total energy loss through windows is 5% of the total energy consumed in US economy. 32% of the residential cooling load is caused from the solar gain through windows, and 19% of heating load results from the losses through windows. An energy-efficient smart window technology can potentially reduce energy consumption for temperature control and lighting, saving tons of billions of dollars on heating, cooling, and lighting costs.

We reviewed current window technologies and identified their inability to have control over both visible and near-infrared radiation as a severe limitation. In other words, visible radiation, which is useful for lighting purposes, is sacrificed to block heat-generating near-infrared radiation. This limitation motivated us to develop a novel smart window technology that incorporates blazed diffractive components into the window assembly to provide spectrally selective control of the solar irradiation.

First, we investigated the optical behavior of physical diffractive structures in different configurations to optimize design parameters such as spatial frequency, groove angle, and angle of incidence. We developed predictive optical models that agree well

with experimental results to design our smart window with high efficiency. We also recognized the limitation that visible wavelengths that are half of near-infrared wavelengths, which blaze in the 1st order, are also blazed in the 2nd order, which results in the visible wavelengths not separating from the near-infrared wavelengths. As a result, we invented a novel way to overcome this limitation by placing two or more gratings in series in opposite blaze directions, where the first grating blazes visible wavelengths and the second grating blazes the near-infrared wavelengths. We have demonstrated this concept successfully to show that diffraction peaks of the visible wavelengths located at the near-infrared wavelengths are shifted away and closer to the normal to the window, which is desirable for admitting the useful visible radiation.

We further extended the physical diffractive concept to electro-optic diffractive structures which provide the additionally desired user controllability. The continuous triangular groove profile of the physical blazed grating is approximated by a 4-step binary profile. Solar irradiance and solar trajectory based on time and location have been analyzed to provide feedback to window operation. Extensive optical modeling and simulation were performed; the results indicated the feasibility of the electro-optic diffractive component for our smart window technology. Furthermore, we determined that the inefficient behavior of the visible wavelengths in the physical blazed grating is reduced by 50% because of the reduced blazing efficiency of the binary approximation.

Toward the objective of fabrication of a proof-of-concept device, we explored and developed fabrication techniques for low-resistivity ITO thin-film deposition and patterning, metal interconnects through vias, alignment layer rubbing, spacer patterning, and liquid crystal injection. The requirement of large-area and defect-free 2 μm spacing

ITO patterning imposed challenges in fabrication. We explored a selective crystallization process using low-fluence excimer laser irradiation as an alternative patterning method. Previous techniques used a phase mask to generate interference patterns for defining fine pitch gratings; we investigated an alternate method involving high-resolution patterning of ITO thin films on a large-area projection system. Lastly, we also investigated a novel method to fabricate physical blazed gratings using angled excimer laser photoablation and *in-situ* masking; initial results look promising for low-cost fabrication of physical blazed gratings.

6.2. Recommendations

In this work, we successfully demonstrated the proposed smart window concept using physical blazed gratings and designed an electro-optic grating concept to provide user controllability and adaptability to the changing incident angles during the day. However, the challenges associated with large-area patterning of defect-free ITO electrodes hampered the operation and testing of the electro-optic device. Future collaboration with facilities that have more sophisticated large-area microelectronic equipments is expected to further this work in the area of smart window technology.

The high-resolution and large-area requirements for the electrode (or pixel) size also impose a new challenge in the driving scheme although a small area batch approach to large area will simplify the overall control system. Further studies to efficiently address an entire window system will be beneficial.

The demonstrated novel method for low-cost fabrication of blazed gratings on polymer substrates requires further experiments to optimize the blazed grating quality for maximum efficiency. We foresee a cost-effective manufacturing approach that will allow this novel diffractive smart window technology to be commercially available and to contribute in reducing energy loss.

REFERENCES

[1] Energy Information Administration, "*Annual Energy Review 2005*," DOE/EIA-0384, 2006.

[2] U.S. Department of Energy, "*Buildings Energy Data Book*," 2006.

[3] A. Beck, W. Körner, O. Gross, and J. Fricke, "Making better use of natural light with a light-redirecting double-glazing system," in *Solar Energy*, vol. 66, pp. 215-221, 1999.

[4] A. K. Athienitis and A. Tzempelikos, "A methodology for simulation of daylight room illuminance distribution and light dimming for a room with a controlled shading device," in *Solar Energy*, vol. 72, pp. 271-281, 2002.

[5] K. Maeda, S. Ishizuka, T. Tsujino, H. Yamamoto, and A. Takigawa, "Optical performance of angle dependent light control glass," in *Proceedings of the SPIE – The International Society for Optical Engineering*, 1991, vol. 1536, pp. 138-148.

[6] A. Helgesson, B. Karlsson, and P. Nostell, "Angular dependent optical properties from outdoor measurements of solar glazings," in *Solar Energy*, vol. 69, pp. 93-102, 2000.

[7] C. M. Lampert, "Progress in Switching Windows," in *Proceedings of SPIE-Solar and Switching Materials*, 2001, vol. 4458, pp. 95-103.

[8] R. Padiyath, C. Haak, and L. Gilbert, "Spectrally selective window films," in *SVC 50th Annual Technical Conference Proceedings*, 2007, pp. 669-673.

[9] C. G. Granqvist, "Spectrally selective surfaces for heating and cooling applications," in *Physics and Technology of Solar Energy. Proceedings of the International Workshop on Physics of Solar Energy*, 1987, vol. 2, pp. 192-276.

[10] C. G. Granqvist, "Spectrally selective coatings for energy efficiency and solar applications," in *Physica Scripta*, vol. 32, pp. 401-407, 1985.

[11] R. T. Kivaisi and G. Mbise, "Multilayer coatings for solar energy control applications," in *Proceedings of the SPIE – The International Society for Optical Engineering*, 1993, vol. 2017, pp. 286-291.

[12] G. Leftheriotis, S. Papaefthimiou, and P. Yianoulis, "Development of multilayer transparent conductive coatings," in *Solid State Ionics*, vol. 136-137, pp. 655-661, 2000.

[13] M. G. Hutchins, "Selective thin film coatings for the conversion of solar radiation," in *Surface Technology*, vol. 20, pp. 301-320, 1983.

[14] H. Bouas-Laurent and H. Durr, "Organic photochromism," in *Pure and Applied Chemistry*, vol. 3, pp. 639-665, 2001.

[15] M. Irie, "Diarylethenes for memories and switches," in *Chemical Reviews*, vol. 100, pp. 1685-1716, 2000.

[16] Y. Yokoyama, "Fulgides for memories and switches," in *Chemical Reviews*, vol. 100, pp. 1717-1739, 2000.

[17] G. Berkovic, V. Krongauz, and V. Weiss, "Spiropyrans and spirooxazines for memories and switches," in *Chemical Reviews*, vol. 100, pp. 1741-1753, 2000.

[18] S. Dong, J. Woo, Z. Chen, Y. Tang, and F. Zhang, "A liquid photochromic diarylethene for high speed photo switches," in *Proceedings of the SPIE – The International Society for Optical Engineering*, 2008, vol. 7125, pp. 712515-1-5.

[19] R. A. Evans, T. L. Hanley, M. A. Skidmore, T. P. Davis, G. K. Such, L. H. Yee, G. E. Ball, and D. A. Lewis, "The generic enhancement of photochromic dye switching speeds in a rigid polymer matrix," in Nature Materials, vol. 4, pp. 249-253, 2005.

[20] K. Sone and Y. Fukuda, *Inorganic Thermochromism*. Berlin : Springer, 1987.

[21] K. Kato, P. K. Song, H. Odaka, and Y. Shigesato, "Study on Thermochromic VO2 Films Grown on ZnO-coated Glass Substrates for Smart Windows," in *Japanese Journal of Applied Physics, Part 1 : Regular Papers and Short Notes and Review Papers*, vol. 42, pp. 6523-6531, 2003.

[22] A. Seeboth, J. Kriwanek, D. Lotzsch, and A. Patzak, "Chromogenic polymer gels for reversible transparency and color control with temperature at a constant volume," in *Polymers for Advanced Technologies*, vol. 13, pp. 507-512, 2002.

[23] B. S. Yu, E. S. Kim, and Y.W. Lee, "Developments in Suspended Particle Devices(SPD)," in *Proceedings of SPIE-Optical Materials Technology for Energy Efficiency and Solar Energy Conversion*, 1997, vol. 3138, pp. 217-225.

[24] P. Drzaic, B. Comiskey, J. D. Albert, L. Zhang, A. Loxley, R. Feeney, and J. Jacobson, "A Printed and Rollable Bistable Electronic Display," in *SID Symposium Digest of Technical Papers*, 1998, vol. 29, pp. 1127-1130.

[25] P. V. Konynenburg, S. Marsland, and J. McCoy, "Solar radiation control using NCAP liquid crystal technology," in *Solar Energy Materials*, vol. 19, pp. 27-41, 1989.

[26] C. M. Lampert, "Large-area Smart Glass and Integrated Photovoltaics," in *Solar Energy Materials & Solar Cells*, vol. 76, pp. 489-499, 2003.

[27] C. G. Granqvist, *Handbook of inorganic electrochromic materials*. Elsevier, 1992.

[28] C. G. Granqvist, "Electrochromic tungsten oxide films: Review of progress 1993–1998," in *Solar Energy Materials & Solar Cells*, vol. 60, pp. 201-262, 2000.

[29] E. S. Lee and D. L. DiBartolomeo, "Application issues for large-area electrochromic windows in commercial buildings," in *Solar Energy Materials and Solar Cells*, vol. 71, pp. 465-491, 2002.

[30] T. J. Richardson, J. L. Slack, B. Farangis, and M. D. Rubin, "Mixed metal films with switchable optical properties," in *Applied Physics Letter*, vol. 80, pp. 1349-1351, 2002.

[31] C. A. Gueymard, *SMARTS, A Simple Model of the Atmospheric Radiative Transfer of Sunshine: Algorithms and Performance Assessment*. Technical Report No. FSEC-PF-270-95. Cocoa, FL : Florida Solar Energy Center, 1995.

[32] D. R. Myers, K. Emery, C. Gueymard, "Proposed Reference Spectral Irradiance Standards to Improve Concentrating Photovoltaic System Design & Performance Evaluation," in *Proceedings of the 29th Institute of Electrical and Electronics Engineers Photovoltaic Specialists Conference*, 2002, pp. 923-926.

[33] D. R. Myers, K. Emery, and C. Gueymard, "Terrestrial Solar Spectral Modeling Tools and Applications for Photovoltaic Devices," in *Proceedings of the 29th Institute of Electrical and Electronics Engineers Photovoltaic Specialists Conference*, 2002, pp. 1683-1686.

[34] D. R. Myers, K. Emery, and C. Gueymard , "Revising and Validating Spectral Irradiance Reference Standards for Photovoltaic Performance," in *Journal of Solar Energy Engineering*, vol. 126, pp. 645-653, 2004.

[35] J. Meeus, *Astronomical Formulae for Calculators*, 4th ed. Richmond, VA: Willmann-Bell Inc., 1988.

[36] J. Meeus, *Astronomical Algorithms*, 2nd ed. Richmond, VA: Willmann-Bell Inc., 1998.

[37] ESRL Global Monitoring Division – GRAD Group, NOAA Solar Calculator, Earth System Research Laboratory, National Oceanic & Atmospheric Administration, U. S. Department of Commerce, http://www.esrl.noaa.gov/gmd/grad/solcalc/.

[38] UO SRML: Sun Chart Program, Solar Radiation Monitoring Laboratory, University of Oregon, http://solardat.uoregon.edu/SunChartProgram.php.

[39] J. M. Cowley, *Diffraction Physics*, 2nd ed. Amsterdam: North-Holland Publishing Co., 1981.

[40] M. V. Klein, *Optics*. New York: John Wiley & Sons Inc., 1970.

[41] K. D. Möller, *Optics*. Mill Valley, CA: University Science Books, 1988.

[42] E. Hecht, *Optics*, 4th ed. San Francisco, CA: Addison Wesley, 2002.

[43] M. Hutley, *Diffraction Gratings (Techniques of Physics)*. London: Academic Press, 1982.

[44] E. G. Loewen and P. Evgeny, *Diffraction Gratings and Applications*. New York: M. Dekker, 1997.

[45] G. R. Harrison, "The diffraction grating – an opinionated appraisal," in *Applied Optics*, vol. 12, pp. 2039-2049, 1973.

[46] G. R. Harrison, and S. W. Thompson, "Large diffraction gratings ruled on a commercial measuring machine controlled interferometrically," in *Journal of the Optical Society of America*, vol. 60, pp. 591-595, 1970.

[47] A. A. Michelson, "Ruling and testing of a ten-inch diffraction grating," in *Proceedings of the American Philosophical Society*, vol. 54, pp. 137-142, 1915.

[48] N. K. Sheridon, "Production of blazed holograms," in *Applied Physics Letters*, vol. 12, pp. 316-318, 1968.

[49] L. Mashev and S. Tonchev, "Formation of holographic diffraction gratings in photoresist," in *Applied Physics A (Solids and Surfaces)*, vol. A26, pp. 143-149, 1981.

[50] S. Lindau, "The groove profile formation of holographic gratings," in *Optica Acta*, vol. 29, pp. 1371-1381, 1982.

[51] R. D. Rallison, R. W. Rallison, and L. D. Dickson, "Fabrication and testing of large area VPH gratings," in *Proceedings of the SPIE – The International Society for Optical Engineering*, 2003, vol. 4842, pp. 10-21.

[52] M. Fukuda, K. Deguchi, M. Suzuki, and Y. Utsumi, "Three-dimensional patterning using fine step motion in synchrotron radiation lithography," in *Journal of Vacuum Science and Technology B*, vol. 24, pp. 2840-2843, 2006.

[53] J. W. Goodman, *Introduction to Fourier Optics*, 3rd ed. Englewood, CO: Roberts & Co., 2005.

[54] Y. Okamura, K. Kitatani, and S. Yamamoto, "Low-voltage driving in nematic liquid crystal overlayered waveguide," in *Journal of Lightwave Technology*, vol. LT-4, pp. 360-363, 1986.

[55] M.-K. Kim, Y.-G. Mo, S-H. Jeong, and W.-S. Choi, "Low driving voltage of cholesteric liquid cyrstal displays," in *2002 SID International Symposium. Digest of Technical Papers. Vol.33*, 2002, vol. 1, pp. 543-545.

[56] V. G. Chigrinov, "Liquid crystal devices for photonics applications," in *Proceedings of the SPIE – The International Society for Optical Engineering*, 2007, vol. 6781, pp. 67811M-1-12.

[57] P. Yeh and C. Gu, *Optics of Liquid Crystal Displays*, 2nd ed. New York: Wiley, 1999.

[58] D.-K. Yang and S.-T. Wu, *Fundamentals of liquid crystal devices*. Chichester: Wiley, 2006.

[59] I.-C. Khoo and S.-T. Wu, *Optics and nonlinear optics of liquid crystals*. Singapore: World Scientific, 1993.

[60] C. Soutar and L. Kanghua, "Determination of the physical properties of an arbitrary twisted-nematic liquid crystal cell," in *Optical Engineering*, vol. 33, pp. 2704-2712, 1994.

[61] M. Schadt, M. Petrzilka, P. R. Gerber, A. Villiger, and G. Trickes, "New liquid crystal materials; physical properties and performance in displays for automobile, high information density and guest-host applications," in *Molecular Crystals and Liquid Crystals*, Vol. 94, pp. 139-153, 1983.

[62] A. Ogiwara, H. Kakiuchida, K. Yoshimura, M. Tazawa, A. Emoto, and H. Ono, "Effects of thermal modulation on diffraction in liquid crystal composite gratings," in *Applied Optics*, vol. 49, pp. 4633-4640, 2010.

[63] A. Miniewicz, K. Komorowska, O. V. Koval'chuk, J. Vanhanen, J. Sworakowski, and M. V. Kurik, "Studies of photorefractive properties of a novel dye-doped nematic liquid crystal system," in *Advance Materials for Optics and Electronics*, vol. 10, pp. 55-67, 2000.

[64] H. Yoshida, C. H. Lee, Y. Miura, K. Tokuoka, S. Suzuki, A. Fuji, and M. Ozaki, "Optical properties of cholesteric liquid crystals with functional structural defects," in *Molecular Crystals and Liquid Crystals*, vol. 489, pp. 73-83, 2008.

[65] S.-T. Wu, U. Efron, and L. D. Hess, "Birefringence measurements of liquid crystals," in *Applied Optics*, vol. 23, pp. 3911-3915, 1984.

[66] M. Schadt and W. Helfrich, "Voltage-dependent optical activity of a twisted nematic liquid crystal," in *Applied Physics Letter*, vol. 18, pp. 127-128, 1971.

[67] K. Kinugawa, Y. Kando, and Y. Nagae, "High-resolution super-twisted nematic liquid crystal displays," in *Hitachi Review*, vol. 38, pp. 103-108, 1989.

[68] B. Dargent and J. Robert, "Twisted nematic flat-panel display," in *1977 SID International Symposium. (Digest of Technical Papers)*, 1977, pp. 60-61.

[69] L. E., Jr., Tannas, "Evolution of flat-panel displays," in *Proceedings of the IEEE*, 1994, vol. 82, pp. 499-509.

[70] U. Efron, B. Apter, and E. Bahat-Treidel, "Studies of fringing field effects in liquid crystal beam-steering devices," in *Proceedings of the SPIE – The International Society for Optical Engineering*, 2005, vol. 5936, pp. 59360P-1-12.

[71] J. Stockley and S. Serati, "Advances in liquid crystal beam steering," in *Proceedings of the SPIE – The International Society for Optical Engineering*, 2004, vol. 5550, pp. 32-39.

[72] S.-T. Wu, S. Gauza, and H. Wang, "High birefringence liquid crystal mixtures for laser beam steering," in *LEOS 2002. 2002 IEEE/LEOS Annual Meeting Conference Proceedings. 15th Annual Meeting of the IEEEE Lasers and Electro-Optics Society (Cat. No. 02CH37369)*, 2002, vol. 2, pp. 522-523.

[73] J. E. Stockley, S. Serati, X. Xiaodong, and R. W. Cohn, "Liquid crystal spatial light modulator for multisport beam steering," in *Proceedings of the SPIE – The International Society for Optical Engineering*, 2004, vol. 5160, pp. 208-215.

[74] E. J. Haellstig, L. Sjoeqvist, and M. Lindgren, "Characterization of a liquid crystal spatial light modulator for beam steering," in *Proceedings of the SPIE – The International Society for Optical Engineering*, 2002, vol. 4632, pp. 187-196.

[75] X. Wang, D. W. Wilson, R. E. Muller, P. D. Maker, and D. Psaltis, "Liquid-crystal blazed-grating beam deflector," in *Applied Optics*, vol. 39, pp. 6545-6555, 2000.

[76] P. F. McManamon, T. A. Dorschner, D. L. Corkum, L. J. Friedman, D. S. Hobbs, M. Holz, S.Liberman, H. Q. Nguyen, D. P. Resler, R. C. Sharp, and E. A. Watson, "Optical phased array technology," in *Proceedings of the IEEE*, 1996, vol. 84, pp. 268-298.

[77] Y.-H. Lin, H. Ren, K.-H. Fan-Chiang, W.-K. Choi, S. Gauza, X. Zhu, and S.-T. Wu, "Tunable-focus cylindrical liquid crystal lenses," in *Japanese Journal of Applied Physics, Part 2 (Letters)*, vol. 44, pp. 243-244, 2005.

[78] X. Wang, H. Dai, and K. Xu, "Tunable reflective lens array based on liquid crystal on silicon," in *Optics Express*, vol. 13, pp. 352-357, 2005.

[79] Y.-H. Fan, H. Ren, X. Liang, and S.-T. Wu, "Tunable-focus liquid crystal microlens arrays for display applications," in *2004 IEEE/LEOS Annual Meeting Conference Proceedings (IEEE Cat. No. 04CH37581)*, 2004, vol. 1, pp. 41-42.

[80] H. Ren, Y.-H. Fan, S. Gauza, and S.-T. Wu, "Tunable-focus flat liquid crystal spherical lens," in *Applied Physics Letters*, vol. 84, pp. 4789-4791, 2004.

[81] S. Kuchibhotla, Anvik Corporation.

[82] L. Kerkache, K. Sadaoui, and A. Layadi, "Structural and electrical properties of as-deposited and annealed DC sputtered ITO thin films," in *European Physical Journal, Applied Physics*, vol. 1, pp. 177-180, 1998.

[83] L. Kerkache, A. Layadi, E. Dogheche, and D. Remiens, "Physical properties of RF sputtered ITO thin films and annealing effect," in *Journal of Physics D (Applied Physics)*, vol. 39, pp. 184-189, 2006.

[84] W.-F. Wu and B.-S. Chiou, "Fabrication and characteristics of RF magnetron sputtered ITO thin films," in *Proceedings of the SPIE – The International Society for Optical Engineering*, 1994, vol. 2150, pp. 319-325.

[85] J. Chae, L. Jang, and K. Jain, "High-resolution, resistless patterning of indium-tin-oxide thin films using excimer laser projection annealing process," in *Materials Letters*, vol. 64, pp. 948-950, 2010.

[86] H. Hosono, M. Kurita, and H. Kawazoe, "Excimer laser crystallization of amorphous indium-tin-oxide and its application to fine patterning," in *Japanese Journal of Applied Physics, Part 2 (Letters)*, vol. 37, pp. L1119-L1121, 1998.

[87] H. Hosono, M. Kurita, and H. Kawazoe, "Excimer laser crystallization of amorphous indium-tin-oxide and application to fabrication of Bragg gratings," in *Thin Solid Films*, vol. 351, pp. 137-140, 1999.

[88] K. Suzuki, N. Hayashi, H. Masuhara, and T. K. Lippert, "Ablation lithography for TFT-LCD," in *Materials Research Society Symposium Proceedings (Advanced Materials and Devices for Large-Area Electronics)*, 2001, v. 685, pp. 1-10.

[89] K. Suzuki, M. Matsuda, T. Ogino, N. Hayashi, T. Terabayashi, and K. Amemiya, "Excimer ablation lithography (EAL) for TFT-LCD," in *Proceedings of the SPIE – The International Society for Optical Engineering*, 1997, vol. 2992, pp. 98-107.

[90] P. J. Janssen, G. A. Melnik, "Liquid crystal display device having spacers with reduced visible artifacts," U. S. Patent 9,835,577, October 17, 2002.

[91] K. H. Yang, "Measurements of empty cell gap for liquid-crystal displays using interferometric methods," in *Journal of Applied Physics*, vol. 64, pp. 4780-4781, 1988.

[92] M. Born and E. Wolf, *Principles of Optics : Electromagnetic Theory of Propagation, Interference and Diffraction of Light*, 7th ed. Cambridge: Cambridge University Press, 1999.

[93] K. Jain, *Excimer Laser Lithography*. Bellingham, WA: SPIE Optical Engineering Press, 1990.

[94] M. Wehner, "Ablative micro-fabrication," in *Excimer Laser Technology, D*. Basting and G. Marowsky, eds., Berlin: Spinger-Verlag, 2005, pp. 149-154.

[95] R. Srinivasan, B. Braren, and R. W. Dreyfus, "Ultraviolet laser ablation of polyimide films," in *Journal of Applied Physics*, vol. 61, pp. 372-376, 1987.

[96] J. Siegel, K. Ettrich, E. Welsch, and E. Matthais, "UV-laser ablation of ductile nabrittle metal films," in *Applied Physics A*,. 64, pp. 213-218, 1997.

[97] J. Chae and K. Jain, "Excimer laser projection photoablation patterning of metal thin films for fabrication of microelectronic devices and displays," in *2008 IEEE Photonics Technology Letters*, vol. 20, pp. 1216-1218, 2008.

[98] M. Gonzalez, F. Axisa, M. V. Bulcke, D. Brosteaux, B. Vandevelde, and J. Vanfleteren, "Design of metal interconnects for stretchable electronic circuits using finite element analysis," in *EuroSime 2007: International Conference on Thermal, Mechanical and Multi-Physics Simulation Experiments in Microelectronics and Micro-Systems*, 2007, pp. 1-6.

[99] K. Lin, J. Chae, and K. Jain, "Design and fabrication of large-area, redundant, stretchable interconnect meshes using excimer laser photoablation and in-situ masking," in *IEEE Transactions on Advanced Packaging*, vol. 33, pp. 592-601, 2010.